

# The ALMA-CRISTAL survey: Resolved kinematic studies of main sequence star-forming galaxies at $4 < z < 6$

Lilian L. Lee<sup>1</sup>, Natascha M. Förster Schreiber<sup>1</sup>, Rodrigo Herrera-Camus<sup>2,3</sup>, Daizhong Liu<sup>4</sup>, Sedona H. Price<sup>5,6</sup>, Reinhard Genzel<sup>1,7</sup>, Linda J. Tacconi<sup>1</sup>, Dieter Lutz<sup>1</sup>, Ric Davies<sup>1</sup>, Thorsten Naab<sup>8</sup>, Hannah Übler<sup>1</sup>, Manuel Aravena<sup>3,9</sup>, Roberto J. Assef<sup>9</sup>, Loreto Barcos-Muñoz<sup>10,11</sup>, Rebecca A. A. Bowler<sup>12</sup>, Andreas Burkert<sup>13</sup>, Jianhang Chen<sup>1</sup>, Rebecca L. Davies<sup>14</sup>, Ilse De Looze<sup>15</sup>, Tanio Diaz-Santos<sup>16,17</sup>, Jorge González-López<sup>18</sup>, Ryota Ikeda<sup>19,20</sup>, Ikki Mitsuhashi<sup>21</sup>, Ana Posses<sup>9,22</sup>, Mónica Relaño Pastor<sup>23,24</sup>, Alvio Renzini<sup>25</sup>, Manuel Solimano<sup>9</sup>, Justin S. Spilker<sup>22</sup>, Amiel Sternberg<sup>26,27</sup>, Kenichi Tadaki<sup>28</sup>, Kseniia Telikova<sup>9</sup>, Sylvain Veilleux<sup>29</sup>, and Vicente Villanueva<sup>2</sup>

(Affiliations can be found after the references)

Received XXX; accepted YYY

## ABSTRACT

We present a detailed kinematic study of a sample of 32 massive ( $9.5 \leq \log(M_*/M_\odot) \leq 10.9$ ) main-sequence star-forming galaxies (MS SFGs) at  $4 < z < 6$  from the ALMA-CRISTAL program. The data consist of deep (up to 15 hr observing time per target), high-resolution ( $\sim 1$  kpc) ALMA observations of the  $[\text{C II}]\lambda 158\mu\text{m}$  line emission. This data set enables the first systematic kpc-scale characterisation of the kinematics nature of typical massive SFGs at these epochs. We find that  $\sim 50\%$  of the sample are disk-like, with a number of galaxies located in systems of multiple components. Kinematic modelling reveals these main sequence disks exhibit high-velocity dispersions ( $\sigma_0$ ), with a median disk velocity dispersion of  $\sim 70 \text{ km s}^{-1}$  and  $V_{\text{rot}}/\sigma_0 \sim 2$ , and consistent with dominant gravity driving. The elevated disk dispersions are in line with the predicted evolution based on Toomre theory and the extrapolated trends from  $z \sim 0-2.5$  MS star-forming disks. The inferred dark matter (DM) mass fraction within the effective radius  $f_{\text{DM}}(< R_e)$  for the disk systems decreases with the central baryonic mass surface density, and is consistent with the trend reported by kinematic studies at  $z \lesssim 3$ ; roughly half the disks have  $f_{\text{DM}}(< R_e) \lesssim 30\%$ . The CRISTAL sample of massive MS SFGs provides a reference of the kinematics of a representative population and extends the view onto typical galaxies beyond previous kpc-scale studies at  $z \lesssim 3$ .

**Key words.** galaxies: high-redshift — galaxies: kinematics and dynamics — galaxies: evolution — submillimeter: galaxies

## 1. Introduction

Studying the kinematics of high-redshift galaxies offers a direct tracer of the distribution of stars, gas, and dark matter on galactic scales. Observations at multiple epochs provide constraints on the evolution of the contribution of rotation and turbulence to the dynamical support of galaxies. Galaxy kinematics are thus a powerful probe of the dominant mechanisms governing the growth and structural formation of galaxies, with processes including gas accretion, non-circular motions, galaxy interactions, and feedback.

Thanks to the advent of near-IR IFU and slit spectroscopy on 8–10m telescopes (e.g. Eisenhauer et al. 2003; Sharples et al. 2013), ionised gas kinematics from rest-frame optical emission lines have become routinely accessible at cosmic noon  $z \sim 1-3$ . This has enabled the census of resolved kinematics of massive star-forming galaxies (SFGs) at  $z \sim 1-3$  on the ‘main sequence’ (MS) of SFGs (e.g. Förster Schreiber et al. 2009; Kassin et al. 2012; Wisnioski et al. 2015), which dominate the population and cosmic star formation rate density (Madau & Dickinson 2014). Cold gas kinematics of the same population of galaxies traced primarily via CO lines are increasingly available through the Atacama Large Millimeter/submillimeter Array (ALMA) and Northern Extended Millimetre Array (NOEMA) (Übler et al. 2018; Nestor Shachar et al. 2023; Rizzo et al. 2023; Liu et al. 2023).

The general findings at  $z \lesssim 3$  suggests a majority of disks among massive (stellar masses  $M_* \gtrsim 10^{10} M_\odot$ ) SFGs have increasing gas velocity dispersion  $\sigma_0$  and decreasing rotational-to-

dispersion support  $V_{\text{rot}}/\sigma_0$  towards higher redshift. These findings are in line with the increase of galactic gas mass fractions, which plays an important role in the emergence of the ‘equilibrium growth’ model of galaxy evolution (see reviews by Tacconi et al. 2020, and references therein) in the framework of marginally stable gas-rich disks (e.g. Genzel et al. 2008; Dekel et al. 2009; Dekel & Burkert 2014; Zolotov et al. 2015; Ginzburg et al. 2022). These works have highlighted the important role of internal processes, alongside accretion and merging, in galaxy stellar mass and structural buildup during the peak epoch of cosmic star formation activity around  $z \sim 2$  (e.g. reviews by Glazebrook 2013; Förster Schreiber & Wuyts 2020).

The exploration of kinematics beyond cosmic noon at  $z > 3$  has been opened by facilities such as ALMA and NOEMA, primarily via the bright  $[\text{C II}]^2 P_{3/2} - ^2 P_{1/2}$  ( $[\text{C II}]\lambda 158\mu\text{m}$ , hereafter  $[\text{C II}]$ ) line emission. The  $[\text{C II}]$  line serves as a key coolant for the interstellar medium (ISM) (e.g. Wolfire et al. 2003). Its relatively low ionisation potential of 11.3 eV (compared to 13.6 eV for hydrogen) allows  $[\text{C II}]$  to arise from various ISM phases, primarily from the photo-dissociation regions (PDRs) (e.g. Vallini et al. 2015; Clark et al. 2019). Consequently, the  $[\text{C II}]$  line is an ideal tracer for kinematics, enabling measurements reaching well beyond the effective radii of these early galaxies (e.g. Lelli et al. 2021; Jones et al. 2021; Tsukui & Iguchi 2021; Umehata et al. 2025).

So far, studies suggest that disks appear to be sub-dominant among the bulk of SFGs at  $z \sim 4-7$  (from rest-UV-selected samples, e.g. Smit et al. 2018; Le Fèvre et al. 2020; Jones et al. 2021;

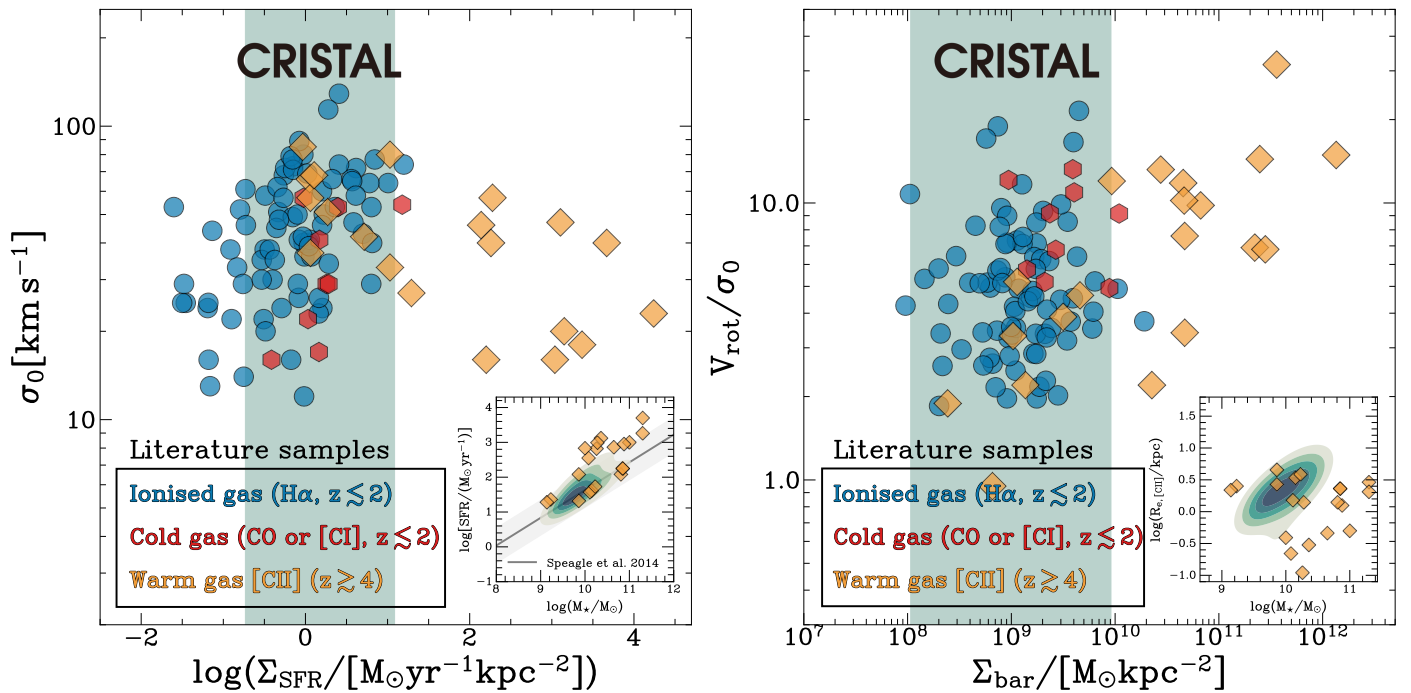


Fig. 1: Parameter space of the CRISTAL sample in terms of surface densities of star formation rate ( $\Sigma_{\text{SFR}}$ , left) and baryons ( $\Sigma_{\text{bar}}$ , right). For comparison, the  $z \sim 2$  main-sequence galaxies observed in  $\text{H}\alpha$  (blue circles) and CO (red hexagons) by [Nestor Shachar et al. \(2023\)](#) are also shown. The inset of the left and right panels show the  $\text{SFR}-M_{\star}$  and  $[\text{C II}]-\text{size}-M_{\star}$  distributions of CRISTAL (green contour) and other studies at  $z \gtrsim 4$  (yellow diamonds) ([Neeleman et al. 2020](#); [Rizzo et al. 2020, 2021](#); [Fraternali et al. 2021](#); [Herrera-Camus et al. 2022](#); [Parlanti et al. 2023](#); [Roman-Oliveira et al. 2023](#)), respectively. The solid line in the left inset is the main-sequence (MS) relation from [Speagle et al. \(2014\)](#) at  $z = 5$  with the shading representing  $\pm 0.5$  dex offset from the relation. For the purpose of this figure, the values of CRISTAL shown on the plots are adopted from ALPINE ([Béthermin et al. 2020](#); [Faisst et al. 2020b](#); [Le Fèvre et al. 2020](#)). CRISTAL provides a higher-resolution sample of MS SFGs that fills up the parameter space currently poorly explored by existing  $z \gtrsim 4$  samples observed with  $[\text{C II}]$ , which predominantly comprises starburst and compact galaxies.

[Herrera-Camus et al. 2022](#); [Posses et al. 2023](#)). While some of them appear to be quite turbulent, high-resolution observations of small samples of individual galaxies, primarily infrared-luminous dusty SFGs, reveal the existence of dynamically cold disks at those early epochs (e.g. [Sharda et al. 2019](#); [Fraternali et al. 2021](#); [Lelli et al. 2021](#); [Rizzo et al. 2021](#); [Tsukui & Iguchi 2021](#); [Roman-Oliveira et al. 2023](#); [Rowland et al. 2024](#)). Larger, more systematic samples covering typical galaxies, such as those provided by ALPINE ( $4 < z < 6$ ; [Le Fèvre et al. 2020](#); [Béthermin et al. 2020](#); [Faisst et al. 2020b](#)) and REBELS ( $7 < z < 8$ ; [Bouwens et al. 2022](#)), are available, albeit at lower spatial resolution and shallower depths. Nevertheless, the typical SFGs targeted by ALPINE formed an ideal sample for high-resolution follow-up studies, and provided the motivation for the CRISTAL ([C II] Resolved ISM in STar forming galaxies with ALMA) survey.

CRISTAL is designed to address four primary science goals: (i) kinematics, (ii) outflows, (iii) spatial distribution of the ISM and star formation, and (iv) the ISM conditions. [Herrera-Camus et al. \(2022\)](#) presented a pilot study of the kinematics of one of the CRISTAL galaxies, HZ4 (CRISTAL-20). [Posses et al. \(2025\)](#) and [Telikova et al. \(2025\)](#) presented detailed case studies of the kinematics of CRISTAL-05 and CRISTAL-22, respectively, and highlighted the improvement in kinematics modelling of complex systems, thanks to higher resolution. The outflow properties of one of the CRISTAL galaxies are presented in [Davies et al. \(2025\)](#) and the overall outflow demographics through stacking in [Birkin et al. \(2025\)](#). Works addressing goals (iii) and (iv) are presented in [Ikeda et al. \(2025\)](#), [Li et al. \(2024\)](#), [Lines et al. \(2025\)](#),

[Mitsuhashi et al. \(2024\)](#), [Solimano et al. \(2025\)](#), and [Villanueva et al. \(2024\)](#). We refer the readers to the overview survey paper by [Herrera-Camus et al. \(2025\)](#) for more details. In this paper, we present the systematic study of the kinematics of the CRISTAL sample.

The structure of this paper is as follows. In § 2, we describe the sample selection and data reduction process. § 3 presents the classification of the kinematic types and § 4 discusses the disk fraction of CRISTAL galaxies. § 5 discusses the kinematic properties of the disks from forward modelling, and compares them with literature results in the context of the dynamical evolution of MS SFGs. § 6 investigates the intrinsic velocity dispersion of CRISTAL disks in the broader context of the dynamical evolution of galaxies with redshift, and explores possible drivers of turbulence, particularly gravitational instabilities and stellar feedback. In § 7, we discuss the dark matter fraction within the effective radius of the CRISTAL disks, and its dependence on the circular velocity and baryonic surface density. § 8 presents a brief discussion on the properties of non-disk galaxies. Finally, § 9 summarises the key findings and outlines ways forward to improve constraints on the nature and kinematics of  $z \sim 4-6$  galaxies.

Throughout, we adopt a flat  $\Lambda$ CDM cosmology with  $H_0 = 70 \text{ km s}^{-1} \text{ Mpc}^{-1}$ , and  $\Omega_m = 0.3$ . Physical size is always reported in physical kiloparsecs (kpc), but we use kpc henceforth for brevity. Where relevant, we quote the rest-frame air wavelengths if not specified otherwise.

## 2. Data and sample selection

### 2.1. Galaxy sample

The full CRISTAL sample is presented by [Herrera-Camus et al. \(2025\)](#). In brief, the survey builds on an ALMA Cycle-8 Large Program (2021.1.00280.L; PI: R. Herrera-Camus), targeting [C II] emission of 19 MS SFGs drawn from ALPINE ([Le Fèvre et al. 2020](#)), selected at  $\log(M_*/M_\odot) \geq 9.5$  and within a factor of 3 of the main sequence of SFGs in their specific SFRs ( $sSFR/sSFR(MS) \leq 3$ ). At the higher resolution of the CRISTAL ALMA observations, some of these sources split into separate components. This sample was expanded with six systems satisfying the same criteria taken from pilot programs and the literature (see details in [Herrera-Camus et al. 2025](#)). There are 39 galaxies in the final CRISTAL sample in total.

The sample studied here consists of the 32 galaxies near the MS that have sufficient S/N and are sufficiently well-resolved to perform quantitative measurements and model their kinematics properties. Table 1 lists the galaxies included in this kinematics sample, along with their redshifts, coordinates, stellar masses ( $M_*$ ) and SFRs, as well as the beam size and sensitivity of the ALMA data sets. Fig. 1 shows the range of  $M_*$ , SFRs, and surface densities in SFR and baryonic masses ( $\Sigma_{SFR}$  and  $\Sigma_{bar}$ ) covered by the CRISTAL MS SFGs, in comparison to those from selected detailed kinematics studies of disks at lower redshifts in ionised and cold molecular gas, and literature work at  $z \gtrsim 4$  from [C II] data ([Neeleman et al. 2020](#); [Rizzo et al. 2020, 2021](#); [Fraternali et al. 2021](#); [Herrera-Camus et al. 2022](#); [Parlanti et al. 2023](#); [Roman-Oliveira et al. 2023](#)). CRISTAL MS SFGs are distinct from most existing samples that predominantly comprise starburst or compact galaxies, allowing for more direct comparison to  $z \sim 1$ –3 kinematics studies of MS star-forming disks at lower redshifts (e.g. [Wisnioski et al. 2015, 2019](#); [Genzel et al. 2020](#); [Nestor Shachar et al. 2023](#); [Puglisi et al. 2023](#)). For the purpose of the figures, we adopt the values from the ALPINE catalogues ([Béthermin et al. 2020](#); [Faisst et al. 2020b](#); [Le Fèvre et al. 2020](#)) to demonstrate the original sample selection. We adopt the values in Table 1 for our subsequent analysis in this work.

### 2.2. ALMA observations and data

We refer the readers to [Herrera-Camus et al. \(2025\)](#) for the observation set-up. In brief, each observation was reduced using the standard CASA (Common Astronomy Software Applications; [CASA Team et al. 2022](#)) pipeline. Each cube was continuum-subtracted in the  $uv$ -plane resulting in a line-only, continuum-free data cube. For the kinematics modelling, we use the cubes with channel width of  $20 \text{ km s}^{-1}$  and natural weighting.<sup>1</sup> We do not apply the ‘JvM’ correction ([Jorsater & van Moorsel 1995](#)) in our analysis, which mostly affects the measurement of integrated properties.

### 2.3. Space-based ancillary data

All of the galaxies in the kinematics sample benefit from high-resolution broad-band optical to mid-IR imaging obtained with the *Hubble Space Telescope* (*HST*) and in most cases also the *James Webb Space Telescope* (*JWST*). Covering stellar continuum emission at rest-frame UV to near-IR wavelengths, this

imaging data provides important complementary information for a full morpho-kinematic classification and important priors in the dynamical modelling of [C II] kinematics. These data sets were reduced in a homogeneous fashion for the CRISTAL sample, as described by [Li et al. \(2024\)](#) and [Herrera-Camus et al. \(2025\)](#).

## 3. (Morpho)-kinematic classification

In this section, we describe the classification of the galaxies from the CRISTAL kinematics sample. We use several methods that have been devised for applications to IFU and interferometric observations of high redshift galaxies, with comparable S/N and resolution as our ALMA data. We determine the final classification by combining the results from each method detailed in §§ 3.1–3.5. We assign 2 points to three metrics (PV, kinemetry and spectro-astrometry) and 1 point to  $V_{obs}/2\sigma$  and morphological information, totalling 8 points.

Table 2 compiles the relevant measurements and resulting classification, and Appendix A provides details of the individual galaxies. In summary, the systems in the CRISTAL sample can be broadly classified into three general groups:

1. Best Disk (22%): Score  $\geq 7$ . They are clear disks with no clear sign of nearby interacting companion within a projected distance of  $\sim 20 \text{ kpc}$  in the *HST*, *JWST* and ALMA data. The velocity gradients are monotonic with a well-defined kinematic position angle ( $PA_k$ ), and the location of steepest slope coinciding with a central peak in observed velocity dispersion, defining the kinematic centre.
2. Disk (28%): Score = 5–6. They show features of a rotating disk but also irregularities. These systems meet most criteria but exhibit some deviations from one or the other pure disk rotation features. Except for two cases, they belong to systems with visible companions in both [C II] and *HST* or *JWST* imaging data.
3. Non-Disk (50%): The rest of the systems with a score  $\leq 4$ . They do not have an apparent velocity gradient across  $\geq 2$  beams and no centralised dispersion peak. Some of them have a visible companion.

### 3.1. Position-velocity diagrams

We extract position-velocity (p-v) diagrams from the original reduced data cubes along the kinematic major axis ( $PA_k$ ) defined as the direction of the largest observed velocity difference across the source. The width of the synthetic slit is equal to the FWHM of each beam, which is taken to be the geometric average of the major and minor axes values listed in Table 1. The slit is positioned to pass through the dynamical centre of the galaxies. We then integrate the light along the spatial direction perpendicular to the slit orientation. These p-v diagrams are presented in Figs. A.5 to A.7 in Appendix A. For visualisation purposes, we median-filtered the p-v diagrams with a kernel size of 3 pixels.

We classify a system as disk-like if there are no detached and distinct velocity structures in the p-v diagrams. This metric contributes to two points in the disk score in Table 2. We do not consider deviations (e.g. CRISTAL-02 and 08) from a standard S-shape as indicative of a merger, as they may instead reflect the possible origin of non-circular gas flow, which could be common for gas-rich systems at higher redshifts.

<sup>1</sup> Except for CRISTAL-19, in which the higher resolution Briggs-weighted (robust = 0.5) cubes have sufficient S/N. There is, however, no significant difference in the kinematics modelling results between the natural-weighted and Briggs-weighted cubes of the two galaxies.

Table 1: Properties of the 32 galaxies in kinematics sample of ALMA-CRISTAL

CRISTAL ID	Full name	$z_{\text{CIII}}$	R.A. ( $^{\circ}$ )	Decl. ( $^{\circ}$ )	$\log(M_*/M_{\odot})$ (dex)	$\log[\text{SFR}/(M_{\odot}\text{yr}^{-1})]^e$ (dex)	Beam size	Cube Noise <sup>e</sup> (mJy beam <sup>-1</sup> )
CRISTAL-01a	DEIMOS_COSMOS_842313	4.554	150.2271	2.5762	10.65	2.31	0'42×0'47	0.13
CRISTAL-01b	...	4.530	150.2282	2.5745	9.81	1.71	0'42×0'47	0.13
CRISTAL-02	DEIMOS_COSMOS_848185, HZ6, LBG-1	5.294	150.0896	2.5864	10.30	2.25	0'45×0'55	0.13
CRISTAL-03	DEIMOS_COSMOS_536534, HZ1	5.689	149.9719	2.1182	10.40	1.79	0'68×0'82	0.15
CRISTAL-04a	vuds_cosmos_5100822662	4.520	149.7413	2.0809	10.15	1.89	0'57×0'75	0.18
CRISTAL-04b	vuds_cosmos_5100822662	4.520	149.7414	2.0813	8.91	0.63	0'57×0'75	0.16
CRISTAL-05	DEIMOS_COSMOS_683613, HZ3	5.541	150.0393	2.3372	10.16	1.83	0'31×0'38	0.16
CRISTAL-06a	vuds_cosmos_5100541407	4.562	150.2538	1.8094	10.09	1.62	0'45×0'54	0.13
CRISTAL-06b	...	4.562	150.2542	1.8097	9.19	1.07	0'45×0'54	0.13
CRISTAL-07a	DEIMOS_COSMOS_873321, HZ8	5.154	150.0169	2.6266	10.00	1.89	0'49×0'74	0.18
CRISTAL-07b	...	5.154	150.0166	2.6268	...	...	0'49×0'74	0.18
CRISTAL-07c	...	5.155	150.0134	2.6271	10.21	1.92	0'49×0'74	0.18
CRISTAL-08	vuds_efdes_530029038	4.430	53.0793	-27.8771	9.85	1.88	0'54×0'80	0.17
CRISTAL-09a	DEIMOS_COSMOS_519281	5.575	149.7537	2.091	9.84	1.51	0'33×0'36	0.16
CRISTAL-10a	DEIMOS_COSMOS_417567, HZ2	5.671	150.5172	1.929	9.99	1.86	0'44×0'48	0.09
CRISTAL-10a-E	...	5.671	150.5186	1.9304	...	...	0'44×0'48	0.09
CRISTAL-11	DEIMOS_COSMOS_630594	4.439	150.1358	2.2579	9.68	1.57	0'38×0'47	0.22
CRISTAL-12	CANDELS_GOODSS_21	5.572	53.0498	-27.6993	9.30	0.98	0'42×0'58	0.12
CRISTAL-13	vuds_cosmos_5100994794	4.579	150.1715	2.2873	9.65	1.51	0'44×0'52	0.18
CRISTAL-14	DEIMOS_COSMOS_709575	4.411	149.9461	2.3758	9.53	1.45	0'11×0'12	0.15
CRISTAL-15	vuds_cosmos_5101244930	4.580	150.1986	2.3006	9.69	1.44	0'36×0'42	0.17
CRISTAL-16a	CANDELS_GOODSS_38	5.571	53.0662	-27.6901	9.60	1.30	0'42×0'58	0.14
CRISTAL-19	DEIMOS_COSMOS_494763	5.233	150.0213	2.0534	9.51	1.45	0'31×0'40 <sup>b</sup>	0.15
CRISTAL-20 <sup>c</sup>	DEIMOS_COSMOS_494057, HZ4	5.545	149.6188	2.0518	10.11	1.82	0'41×0'45	0.06
CRISTAL-21 <sup>c</sup>	HZ7	5.255	149.8769	2.1341	10.11	1.80	0'32×0'35	0.22
CRISTAL-22a <sup>c</sup>	HZ10	5.653	150.2471	1.5554	10.35	2.13	0'27×0'34	0.22
CRISTAL-22b <sup>c</sup>	HZ10	5.653	150.2469	1.5554	...	...	0'27×0'34	0.22
CRISTAL-23a <sup>d</sup>	DEIMOS_COSMOS_818760	4.560	150.4786	2.5421	10.55	2.50	0'25×0'30	0.35
CRISTAL-23b <sup>d</sup>	DEIMOS_COSMOS_818760	4.562	150.4790	2.5421	10.46	1.72	0'25×0'30	0.35
CRISTAL-23c <sup>d</sup>	...	4.565	150.4778	2.5421	...	...	0'25×0'30	0.35
CRISTAL-24 <sup>d</sup>	DEIMOS_COSMOS_873756	4.546	150.0113	2.6278	10.53	2.06	0'26×0'31	0.46
CRISTAL-25 <sup>d</sup>	vuds_cosmos_5101218326	4.573	150.3021	2.3146	10.90	2.75	0'25×0'30	0.38

**Notes.** <sup>(a)</sup> Adopted from [Mitsuhashi et al. \(2024\)](#) and [Li et al. \(2024\)](#). They are in broad agreement with the values inferred from existing  $L_{\text{CIII}}$ -SFR relations as demonstrated by [Li et al. \(2024\)](#) and references therein. <sup>(b)</sup> Briggs-weighted data is used. <sup>(c)</sup> CRISTAL pilot targets. <sup>(d)</sup> From ALMA archive. <sup>(e)</sup> Cube noise are measured in cubes with  $20 \text{ km s}^{-1}$  channel width. CRISTAL-01c, 07d, 09b, 10b, 16b, 17, 18 are not included in this study because they are either too faint for kinematics analysis or not detected. SMG J1000+0234 and CRLE are excluded because they are starburst galaxies. A full table with all CRISTAL source is available in Table 1 of [Herrera-Camus et al. \(2025\)](#).



Table 2: Kinematic Classification and Properties of CRISTAL galaxies

ID	Classification <sup>a</sup>	PA <sub>k</sub> <sup>b</sup> (°)	$V_{\text{obs}}/2$ <sup>c</sup> (km s <sup>-1</sup> )	$V_{\text{obs}}/2\sigma_{\text{int}}$ <sup>d</sup>	$f_{\text{molgas}}$ <sup>e</sup>	$K_{\text{asym}}$ <sup>f</sup>	Disk Score <sup>g</sup> (Total: 8)
01a	Non-Disk	295.6	116.54±26.56	0.41 ±0.09	0.10 <sup>+0.21</sup> <sub>-0.06</sub>	0.29±0.05	3
01b	Non-Disk	325.8	54.54±5.64	0.46 ±0.12	...	0.63±0.78	3
02	Disk	126.9	65.19±6.24	0.45 ±0.04	0.43 <sup>+0.21</sup> <sub>-0.11</sub>	0.23±0.03	5
03	Best Disk	126.6	50.0±11.99	0.35 ±0.09	0.13 <sup>+0.14</sup> <sub>-0.06</sub>	0.15±0.03	7
04a	Non-Disk	171.5	47.16±13.87	0.58 ±0.17	0.39 <sup>+0.25</sup> <sub>-0.12</sub>	0.71±0.12	1
04b	Non-Disk	207.9	27.6±20.78	0.68 ±0.51	...	0.54±0.15	1
05a	Disk	...	...	...	0.39 <sup>+0.29</sup> <sub>-0.13</sub>	...	... <sup>h</sup>
05b	Non-Disk	...	...	...	...	...	... <sup>h</sup>
06a	Non-Disk	268.0	44.18±2.09	0.57 ±0.03	0.51 <sup>+0.26</sup> <sub>-0.13</sub>	2.10±0.28	3
06b	Disk	79.0	48.11±7.29	0.56 ±0.09	...	0.35±0.17	5
07a	Disk	359.0	83.3±6.03	0.88 ±0.08	0.43 <sup>+0.28</sup> <sub>-0.13</sub>	0.20±0.03	5
07b	Non-Disk	66.8	63.37±15.79	0.62 ±0.16	...	0.84±0.15	3
07c	Non-Disk	32.0	100.56±19.01	0.91 ±0.18	0.21 <sup>+0.20</sup> <sub>-0.09</sub>	0.81±0.42	4
08	Best Disk	123.0	110.43±28.70	0.94 ±0.25	0.63 <sup>+0.29</sup> <sub>-0.13</sub>	0.18±0.06	7
09a	Disk	170.0	84.27±59.79	0.63 ±0.45	0.74 <sup>+0.32</sup> <sub>-0.12</sub>	0.25±0.27	6
10a	Non-Disk	226.0	127.79±24.82	0.78 ±0.16	0.73 <sup>+0.23</sup> <sub>-0.11</sub>	0.36±0.06	3
10a-E	Disk	123.0	30.54±15.88	0.32 ±0.16	...	0.35±0.03	6
11	Best Disk	335.0	63.19±45.60	0.45 ±0.32	0.73 <sup>+0.23</sup> <sub>-0.13</sub>	0.13±0.05	8
12	Disk	34.3	25.72±18.66	0.43 ±0.31	0.67 <sup>+0.43</sup> <sub>-0.15</sub>	0.45±0.08	7
13	Non-Disk	17.0	145.26±13.16	0.96 ±0.11	0.63 <sup>+0.17</sup> <sub>-0.13</sub>	0.37±0.03	4
14	Non-Disk	61.9	73.79±27.03	0.55 ±0.20	0.78 <sup>+0.23</sup> <sub>-0.10</sub>	0.49±0.33	3
15	Best Disk	308.2	37.27±3.89	0.28 ±0.03	0.41 <sup>+0.27</sup> <sub>-0.13</sub>	0.51±0.22	7
16	Non-Disk	14.0	52.58±9.06	0.44 ±0.08	0.69 <sup>+0.33</sup> <sub>-0.14</sub>	2.78±0.70	1
19	Best Disk	313.0	110.58±37.79	0.89 ±0.31	0.70 <sup>+0.27</sup> <sub>-0.12</sub>	0.17±0.32	8
20	Best Disk	17.0	68.31±13.26	0.73 ±0.14	0.47 <sup>+0.35</sup> <sub>-0.15</sub>	0.14±0.08	8
21	Non-Disk	41.0	27.82±18.31	0.19 ±0.12	0.59 <sup>+0.28</sup> <sub>-0.13</sub>	2.17±1.43	4
22a	Disk	...	...	...	0.71 <sup>+0.28</sup> <sub>-0.12</sub>	...	... <sup>i</sup>
22b	Non-Disk	...	...	...	...	...	... <sup>i</sup>
23a	Non-Disk	354.0	45.79±1.27	0.40 ±0.02	0.40 <sup>+0.23</sup> <sub>-0.12</sub>	1.12±0.29	3
23b	Disk	260.0	51.31±2.32	0.34 ±0.02	0.25 <sup>+0.18</sup> <sub>-0.09</sub>	0.21±0.02	6
23c	Best Disk	45.0	92.78±4.82	0.83 ±0.06	0.17 <sup>+0.13</sup> <sub>-0.07</sub>	0.17±0.04	8
24	Non-Disk	60.0	140.69±22.69	0.43 ±0.07	0.51 <sup>+0.06</sup> <sub>-0.05</sub>	0.38±0.11	4
25a	Non-Disk	309.0	60.03±30.54	0.61 ±0.31	...	0.45±0.10	4
25b	Non-Disk	335.0	98.95±26.06	0.86 ±0.23	...	0.32±0.08	4

**Notes.** <sup>(a)</sup> Classification of the sample based on the Disk Score. <sup>(b)</sup> Position angle along the kinematic major axis pointing to the blue side. <sup>(c)</sup> Half difference between the observed maximum and minimum velocities:  $V_{\text{obs}}/2 = (V_{\text{max}} - V_{\text{min}})/2$ . <sup>(d)</sup> Ratios between (c) and the [C II] integrated line widths  $\sigma_{\text{int}}$ . <sup>(e)</sup> Molecular gas fraction inferred in Appendix C for systems with dust continuum detection. <sup>(f)</sup> Asymmetry measure of the velocity and velocity dispersion fields following [Shapiro et al. \(2008\)](#) demarcation. <sup>(g)</sup> The sum of points from the metrics outlined in §§ 3.1–3.5, with the following scheme: Best Disk if Disk Score  $\geq 7$ , Disk if 5–6, and Non-Disk if  $\leq 4$ . <sup>(h)</sup> See [Posses et al. \(2025\)](#). <sup>(i)</sup> See [Telikova et al. \(2025\)](#).

### 3.2. Kinematics profiles and $V_{\text{obs}}/2\sigma_{\text{int}}$

The ratio between the full observed velocity difference across a source ( $V_{\text{obs}}$ ) and the source-integrated line width ( $\sigma_{\text{int}}$ ) has been used as proxy to distinguish systems with dominant support from rotational/orbital motions versus random motions (e.g. [Förster Schreiber et al. 2009](#); [Wisnioski et al. 2015](#)). The  $V_{\text{obs}}$  and  $\sigma_{\text{int}}$  are measured from the data, without beam-smearing and inclination corrections. The boundary at  $V_{\text{obs}}/2\sigma_{\text{int}} = 0.4$  adopted in previous work, based on mock disk models, is also applicable for the typical range of galaxy sizes relative to beam sizes for our sample.

We measure the integrated line width  $\sigma_{\text{int}}$  from spatially integrated spectra extracted from the reduced data cubes. The cubes are at the original spatial and spectral resolution and with the channel size of  $\Delta V = 20 \text{ km s}^{-1}$ . The circular apertures for the extraction are positioned at the in order to capture the contribu-

tions from both velocity gradients and local velocity dispersion to  $\sigma_{\text{int}}$ . The apertures' sizes roughly followed those determined by [Ikeda et al. \(2025\)](#). We then sum the spectra of individual pixels within the apertures to obtain the integrated spectrum. The extracted spectra are shown in the last column of Figs. A.5 to A.7 in Appendix A.

We fit the spectrum with a single Gaussian with `emcee` ([Foreman-Mackey et al. 2013](#)) to extract the line widths, except for CRISTAL-02, where we fit a double Gaussian profile as there is a broad component possibly associated with an outflow ([Davies et al. 2025](#)). The emission from the narrow component is always the one used in this analysis.

The fitted values of integrated line widths ( $\sigma_{\text{int}}([\text{C II}])$ ) are annotated in Figs. A.5 to A.7 along with the best-fit model overlaid on the extracted spectra. Uncertainties of  $\sigma_{\text{int}}([\text{C II}])$  are taken as the [16, 84]-th percentile ( $1\sigma$ ) bounds of the

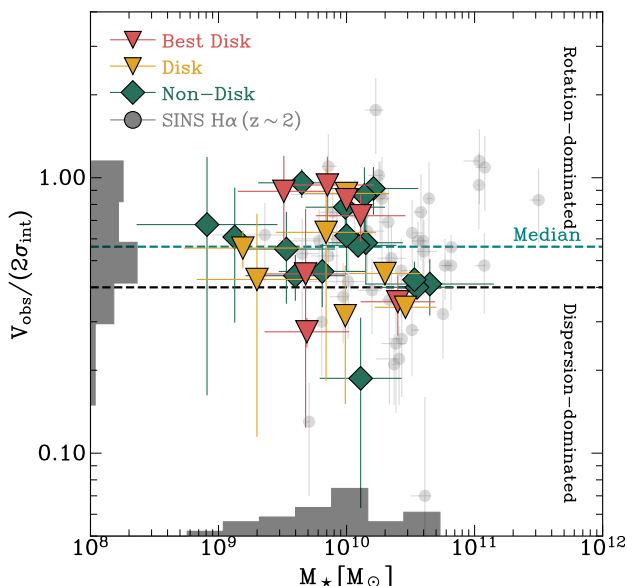


Fig. 2: Ratios of observed half velocity gradient  $V_{\text{obs}}/2$  and integrated line width ( $\sigma_{\text{int}}$ ) of [C II] as a function of stellar mass  $M_*$ . The black horizontal dashed line represents the distinction value ( $V_{\text{obs}}/2\sigma_{\text{int}} = 0.4$ ), which demarcates the boundary between rotation- and dispersion-dominated systems, as commonly used in the literature.

marginalised posterior distributions. We stress that the  $\sigma_{\text{int}}$  quantity determined here does not represent the local intrinsic disk velocity dispersion, but rather a global measure of the dynamical support combining rotation/orbital motions and random motions.

The  $V_{\text{obs}}$  is defined as the maximum observed velocity difference  $V_{\text{obs}} = V_{\text{max}} - V_{\text{min}}$ . We extract velocity profiles from the p-v diagrams obtained in § 3.1 by fitting a single Gaussian profile column-by-column (i.e., collapsed emission of the velocity channels at the same position) using again *emcee* (Foreman-Mackey et al. 2013). A one-pixel-wide vertical pseudo-slit is moved along the position axis. The centroids and widths of the fitted Gaussian models will then be the velocity and velocity dispersion at the locations of the slits. Finally, the extracted profiles are down-sampled by averaging to a resolution of one-half to one-fourth of the beam FWHM. The velocity and velocity dispersion profiles will then serve as an input for the dynamical modelling in § 5.

We list the  $V_{\text{obs}}/2\sigma_{\text{int}}$  of our sample in Table 2. We plot in Fig. 2 the distribution of  $V_{\text{obs}}/2\sigma_{\text{int}}$  as a function of the stellar mass. For comparison, we show the values for the SINS H $\alpha$  IFU sample at  $z \sim 2$  (Förster Schreiber et al. 2009). The median  $V_{\text{obs}}/2\sigma_{\text{int}}$  of all samples is 0.56. For the Best Disk, Disk and Non-Disk samples, the median values are 0.73, 0.45 and 0.57, respectively.

We observe that many Non-Disk systems have  $V_{\text{obs}}/2\sigma_{\text{int}} > 0.4$ , which can be attributed to the fact that mergers may exhibit a substantial projected velocity gradient from orbital motions depending on the orientation of the merging system. While the  $V_{\text{obs}}/2\sigma_{\text{int}}$  ratio is useful, especially in cases where the sources are less well resolved, it is not sufficient to unambiguously distinguish disks from mergers. Therefore, this metric contributes only one point to the disk score in Table 2.

### 3.3. Velocity and velocity dispersion maps and their asymmetry

To derive the flux, velocity, and velocity dispersion maps, we fit a single Gaussian profile to the [C II] emission line of each spaxel in the continuum-subtracted line cube in velocity units, with the amplitude, mean and standard deviation of the profile as free parameters. In the resulting [C II] kinematic maps, we mask pixels with  $S/N < 3$  and pixels resulting in unphysical outlier values. For the velocity map, we determine the systemic velocity of the galaxy by symmetrising the red-shifted and blue-shifted peak velocities. Fig. 3 displays the derived velocity and velocity dispersion maps, plotted in the  $M_*$  versus offset from the MS in SFR. The line flux, velocity, and velocity dispersion maps of individual galaxies are shown in the fourth and fifth columns of Figs. A.5 to A.7 in Appendix A.

Under the assumption of a single Gaussian profile, our fits primarily capture the narrower line emission component dominated by star formation. Such single-component fits of individual pixel spectra will be little sensitive to possible emission from broader lines originating, e.g. from outflowing gas as long as the amplitude of the broad component is sufficiently low (e.g. Förster Schreiber et al. 2018). Examination of our CRISTAL data shows this is the case for all galaxies considered here except for CRISTAL-02, where more prominent outflow components are detected (Davies et al. 2025). In the kinematic maps of these galaxies, the regions (largely outside of the main body of the sources) are masked out for quantitative analysis.

We then use kinemetry (Krajinović et al. 2006) to quantify asymmetries in the velocity and velocity dispersion maps of our galaxies, following the method described by Shapiro et al. (2008) for applications in studies of galaxy kinematics at  $z \sim 2$  (see also, e.g. Swinbank et al. 2012; Genzel et al. 2023).

Kinemetry performs Fourier analysis on the velocity and dispersion maps, decomposed into concentric ellipses, with the centre, position angle (PA), and inclination determined a priori through methods detailed in § 3.1. Given the limited S/N and angular resolution of our data, we fix the centre,  $PA_k$ , and inclination to the adopted values in §§ 3.1 and 5, respectively. and require at least 75% of valid pixels in an annulus. We follow the Fourier expansion up to the fifth order term, similar to Shapiro et al. (2008).

We use the demarcation set by Shapiro et al. (2008) at  $K_{\text{asym}} = \sqrt{(v_{\text{asym}}^2 + \sigma_{\text{asym}}^2)} = 0.5$ , above which the system is classified as a merger and below which is a disk. The  $v_{\text{asym}}$  and  $\sigma_{\text{asym}}$  are dimensionless measures of the average higher-order kinematic coefficients in the Fourier expansion relative to the coefficients corresponding to the regular rotation.

We plot the  $v_{\text{asym}}$  and  $\sigma_{\text{asym}}$  of the CRISTAL galaxies in Fig. 4. There are 20 and 10 galaxies (out of 30 with measurements) fall into the ‘disk’ and ‘merger’ regime, respectively, according to the fiducial  $K_{\text{asym}} = 0.5$ . Some Disks and Non-disks (according to the overall classification) overlap in the region around the boundary, which can reflect intrinsic deviations from pure circular motions caused by minor merging, non-axisymmetric structures such as bars/spirals even in the absence of interactions, noise in kinematic maps or incomplete coverage of the objects due to regions with lower S/N and fainter surface brightness, beam smearing, or a combination of these factors. For illustrative purposes, we indicate in Fig. 4 the band corresponding to  $K_{\text{asym}} = 0.3$  to  $0.9$ , which for the simulated galaxies used by Shapiro et al. (2008) to calibrate the threshold would result in 6% higher merger fraction or 3% higher disk fraction,

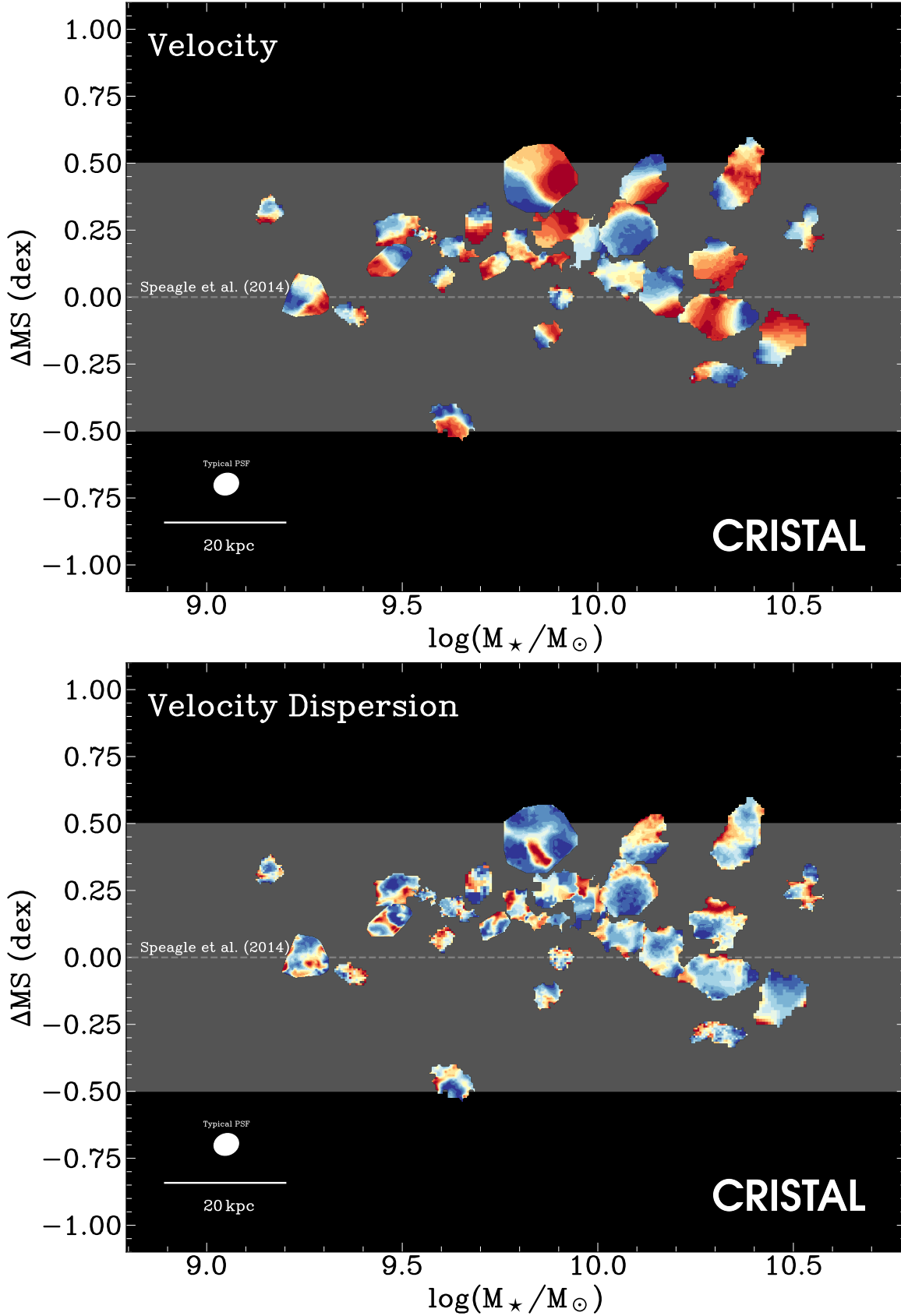


Fig. 3: Velocity (*Top*) and velocity dispersion (*bottom*) fields of CRISTAL galaxies placed on the  $\Delta MS$  offset relative to the [Speagle et al. \(2014\)](#) main-sequence (MS) relation. The velocity and dispersion fields correspond to that derived from the [C II] emission described in § 3.3. For the velocity fields, the colour coding represents the relative velocity of the line emission with respect to the systemic velocity. For the dispersion fields, the colour coding indicates the widths (in standard deviation) of the 1D Gaussian fitted to the spectra of individual spaxels. All sources are shown in the same field of view of  $3''$  ( $\sim 20$  kpc at  $z \sim 5$ ). The median beam size ( $0''.43 \times 0''.36$ ) with position angle ( $104^\circ$  counter-clockwise from north) is shown at the bottom left; the individual values are listed in Table 1.

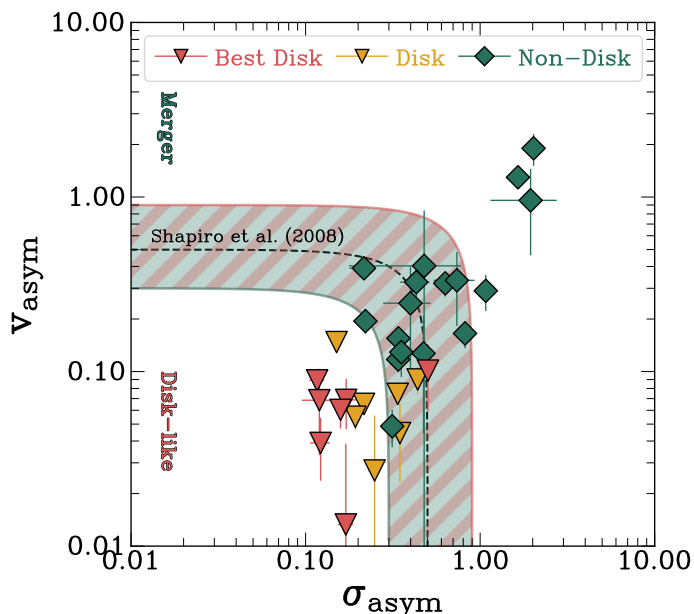


Fig. 4: Asymmetry measure of the velocity and velocity dispersion fields for the CRISTAL galaxies from Kinemetry (Krajinović et al. 2006) is shown in Fig. 4. The black dashed line represents the demarcation in Shapiro et al. (2008) at  $K_{\text{asym}} = 0.5$ . With this metric alone, we classify a system as disk-like if it falls below the dashed line and as a merger if it falls above. Over half of the samples fall below the dashed line. The pink ( $K_{\text{asym}} = 0.9$ ) and green ( $K_{\text{asym}} = 0.3$ ) lines indicate the modified demarcations.

respectively. Adopting the fiducial threshold for CRISTAL, we classify galaxies with  $K_{\text{asym}} \leq 0.5$  as disk, counting for 2 points in the disk score from this metric.

### 3.4. Spectro-astrometry

We also applied spectro-astrometry (SA) to classify our sample. This technique, commonly used to study compact, marginally resolved stellar binary systems (e.g. Christy et al. 1981; Beckers 1982) was successfully applied to IFU observations of high- $z$  galaxies (e.g. Gnerucci et al. 2010; Perna et al. 2025). SA operates on the principle that closely spaced sources with projected separation below the angular resolution element can be spectrally separated if their relative velocities differ. This technique leverages the 3D information in data cubes and can be especially useful in retrieving velocity gradients when beam smearing is important.

For each velocity channel map, we derive the spatial offsets along the  $X$  and  $Y$  directions by fitting a 2D Gaussian without any a priori assumptions of the kinematics major axis. In cases where multiple emission peaks are observed and are separated by multiple beams in FWHM, we fit multiple 2D Gaussians to the emission blob. We derive the positional uncertainty following Eq. (1) in Condon et al. (1998), which depends on the amplitude of the emission and the beam size, in addition to the formal fitting errors. We show the locus traced by the SA measurements in the sixth column in Figs. A.2 to A.4 in Appendix A, overlaid on either *HST* or *JWST* colour images.

For a galaxy to be considered Best Disk, its SA locus should be uni-directional, i.e., moving along monotonically in one direction, as in the case of CRISTAL-15 and 20 (Fig. A.2). However, for systems with non-circular motion, the loci would de-

viate from a straight line near the centre, as in the case of CRISTAL-02 and 08, but would overall follow a single direction. In all cases, the overall direction of the velocity gradients agrees with the velocity map with consistent  $PA_{\text{kin}}$ . For Non-Disks, the SA loci would exhibit a more zig-zag shape, characterised by sudden changes in opposite direction; when companions are present, the loci show discontinuities with abrupt jumps from one location to another, often separated by one to two resolution elements.

The inherent nature of SA results in uneven spatial sampling, while spectral sampling remains constant. The spectral resolution of our SA measurement is naturally determined by the channel width, which is set at  $20 \text{ km s}^{-1}$ . We do not consider a wider channel width, such as e.g.  $50 \text{ km s}^{-1}$  because it would have poorly compromised spectral sampling for several sources with observed velocities  $v_{\text{obs}} < 200 \text{ km s}^{-1}$  (Table 2). In the case of Non-Disk sources, which could potentially be mergers, there could be a few channels with emission peaks that are spatially close to each other. Although this may appear to be a spatial sampling that is too high on the SA curve, we have chosen to retain these data, as they could indicate unresolved line-of-sight mergers.

The fainter outer regions of the sources, often associated with the most blue-/redshifted emission, tend to have too low S/N for a robust centroid measurement; consequently, the full velocity gradient may not be probed for some of our targets.

This metric adds two points to the disk score in Table 2.

### 3.5. Morphology of rest-frame UV-optical and [C II] line emission

We complement the kinematic classification methods described in the previous sections with morphological information. We consider the *HST* along with *JWST*/NIRCam data and [C II] data. The longest wavelength NIRCam filter F444W corresponds to the rest-frame optical emission ( $\lambda = 0.7 \mu\text{m}$ ) at  $z = 5$ , redwards of the Balmer break, in contrast to the rest-frame  $0.3 \mu\text{m}$  provided by *HST*/F160W. The depth of the *JWST* data varies across the sample, with CRISTAL-08, 11, 13, and 15 being the deepest.

We consider source multiplicity in our inspection of the imaging data. In most cases, our ALMA data already indicate the single or multiple nature of the galaxies, with 14 of the multiple systems associated with Non-Disks according to the kinematic criteria applied in §§ 3.1–3.4. The higher angular resolution of *JWST* can provide a more detailed view of the morphology and deblending unresolved companions within the ALMA beam that could explain the observed perturbations in the [C II] kinematics. We emphasise that the companions we defined in Table 1 are unlikely to be multiple clumps within a single galaxy, as their closest separations is on average  $\sim 8 \text{ kpc}$ , ranging from 5 to 10 kpc, which is much larger than the typical size of SFGs at  $z \sim 5$  (Miller et al. 2024; Varadaraj et al. 2024). We further stress that multiplicity on a few kpc-scales could be ambiguous, as clumpy disks may mimic multiple systems especially if the sensitivity is insufficient to detect a fainter host galaxy underlying bright clumps.

The first two columns of Figs. A.2 to A.4 present a comparison between *HST* and *JWST* colour-composite images. We observe a marked difference between the rest-frame optical and UV images of galaxies in CRISTAL-01a, 07c, 08, 11, 12, 13, 16, 24, and 25. For systems CRISTAL-02 and 04a, the rest-frame optical resembles that in the UV. However, all galaxies retain their substructures or clumpy appearance. The single-pair clas-



sification using the [C II] and *HST*-based morphologies of Ikeda et al. (2025) are unchanged with the additional information from *JWST* data and the multiplicity remain the same.

To highlight the clumpiness and substructures, we subtract the F444W image by a smooth Sérsic (Sérsic 1968) model in Appendix B. The clumpy appearance of CRISTAL-02, 08, and 15 is apparent in the residual images shown in Fig. B.1.

Since many of the galaxies are not well-fitted by a Sérsic model, we do not consider the difference of *JWST* (or *HST*) morphological PA and  $PA_{\text{kin}}$  (defined in § 3.1) as a disk criterion because the former is not well-constrained.

There are systems with visible [C II] companions or extended emission, such as CRISTAL-01b, 12, and 13, but no associated counterparts in either *HST* or *JWST* images. This suggests that we are still missing the more evolved stellar population due to extinction or simply fainter emission with the shallow NIR-Cam data. Therefore, we consider the imaging data as complementary but not decisive evidence for the kinematics nature. With the visual inspection of *JWST* and *HST* images, alongside [C II] line maps, we classify a system as a disk if it is a single-component system with smooth underlying emission, possibly featuring bright clumpy substructures that are closely spaced (typically within  $\lesssim 2$  kpc, generally consisting of more than two clumps). Additionally, there should be no detectable companion within  $\lesssim 20$  kpc across the observed wavelengths. This contributes one point towards the disk score.

#### 4. Disk fraction

Considering the systems with disk score  $\geq 5$ , the total disk fraction among the 32 CRISTAL kinematics samples is  $50 \pm 9\%$  ( $N = 16$ ), encompassing both Best Disk and Disk (Table 2). Best Disk and Disk make up of  $22 \pm 7\%$  ( $N = 7$ ) and  $28 \pm 8\%$  ( $N = 9$ ) of the sample, respectively. The errors are binomial errors. The distribution of these types is shown in the inset in Fig. 5. The disk fraction in our study is higher than that reported in the previous ALPINE work (Le Fèvre et al. 2020), which found that for the overlapping CRISTAL sample,  $\lesssim 40\%$  of systems are classified as ‘Rotator’ or ‘Extended Dispersion Dominated’, with only  $< 20\%$  being the former, and the remaining systems being ‘Pair-Merger’.

The 50% disk fraction of CRISTAL ( $4.4 < z < 5.7$ ) is consistent with morphological studies based on NIRC*am*/*JWST* data, which reveal a high fraction of disks of  $\sim 35\%$  on average across studies (Ferreira et al. 2023; Jacobs et al. 2023; Kartaltepe et al. 2023; Huertas-Company et al. 2024; Lee et al. 2024; Pandya et al. 2024; Tohill et al. 2024). A smaller sample using *JWST*/MIRI also supports this finding (Costantin et al. 2025). These results suggest an early establishment of the Hubble sequence (Ferreira et al. 2023; Xu & Yu 2024; Huertas-Company et al. 2025).

In particular, we compare our CRISTAL disk fraction with Ferreira et al. (2023), a morphological study of  $\sim 4,000$  galaxies from the CEERS survey, classified in rest-frame optical observed with *JWST*. Fig. 5 plots our disk fractions against their evolutionary trend. For consistency we select galaxies from Ferreira et al. (2023) in the same mass and  $\Delta MS$  ranges as our kinematic sample, using the galaxy parameters from the CANDELS-EGS catalogue of Stefanon et al. (2017). We do not apply surface brightness corrections to the fractions as we compare with the direct fraction from our kinematic classification. Fig. 5 shows these derived morphology-based disk fractions over  $z \sim 1$ –6; our kinematics-based disk fraction for the CRISTAL MS SFGs are in very good agreement.

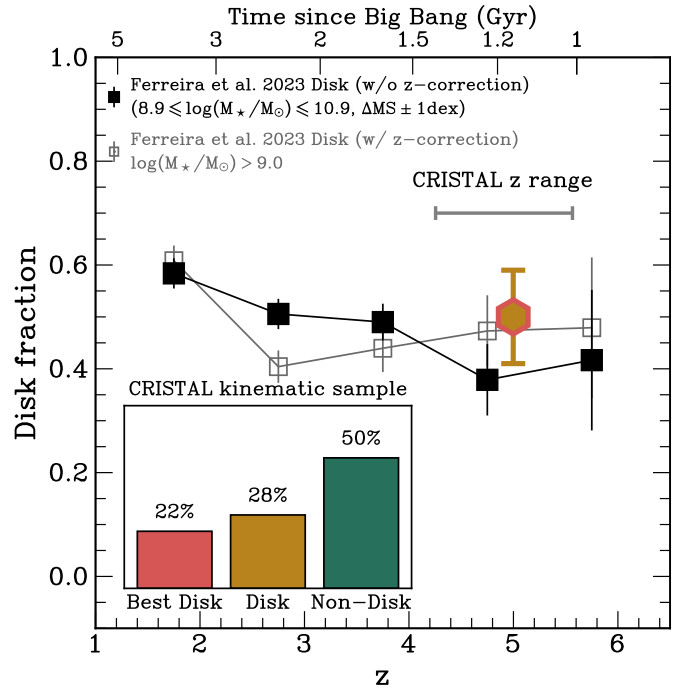


Fig. 5: Comparison of the CRISTAL total disk fraction (yellow hexagon with red outline) to the mass-selected sample from Ferreira et al. (2023) based on CRISTAL mass range. The grey curve with square marker shows the ‘redshift-corrected’ trend of their high-mass bin. To more fairly compare with our sample, we further selected so that their star formation rates are within 1 dex from the Speagle et al. (2014) main sequence relation. The grey horizontal line indicates the redshift range of CRISTAL ( $4.4 < z < 5.7$ ). The black solid curve with square markers represents the redshift evolution of disk fraction as reported by Ferreira et al. (2023) before their application of ‘redshift corrections’, which primarily account for surface brightness effects in higher redshift objects. It would be a more equal comparison since we do not apply any such correction to the CRISTAL disk fraction. The inset shows the distribution of Best Disk, Disk and Non-Disk among the CRISTAL sample.

The presence of Disk (disks in an interacting system) is perhaps not surprising, as hinted from simulation (see also the classic example of M51); gravitational interactions between galaxies and the presence of rotating disks are not inherently contradictory (Springel & Hernquist 2005; Robertson et al. 2006). The rotation of a disk is relatively resilient to minor mergers. For gas-rich systems, the stellar disk can rapidly reform and sustain itself through the formation of new stars from the remaining gas, even if the pre-existing stellar disk is destroyed in the process (Übler et al. 2014; Peschken et al. 2020; Sotillo-Ramos et al. 2022).

#### 5. Kinematics modelling and properties of the disk samples

##### 5.1. Forward modelling with *DysmalPy*

To extract the intrinsic kinematics and mass distribution of CRISTAL disks, we use the public forward-modelling code *DysmalPy*<sup>2</sup> (Davies et al. 2004b,a; Cresci et al. 2009; Davies et al. 2011; Wuyts et al. 2016; Lang et al. 2017; Price et al.

<sup>2</sup> <https://www.mpe.mpg.de/resources/IR/DYSMALPY>

2021; Lee et al. 2025). Table 3 reports the best-fit results. We refer the readers to the earlier cited works for a detailed description of `DysmalPy`. In short, it is a forward modelling tool that starts from a parametrised input mass distribution to establish the best-fit models for the data. The models consist of a baryonic disk, bulge (optional), and DM halo. The disk component is parametrised as a Sérsic profile of index  $n_d = 1$  (exponential disk) adopted for all fits, with flattening  $q_d$  and effective radius  $R_{e,\text{disk}}$ .

The baryonic disk component is assumed to be a thick oblate disk, treated as a flattened spheroid of intrinsic axis ratio  $q = c/a$ , and the rotation curve (RC) is derived accordingly following the Noordermeer (2008) parametrisation. We assume the velocity dispersion is locally isotropic and radially uniform, representing a dominant turbulence term,  $\sigma_0$ .

We adopt the Burkert et al. (2010) pressure support (asymmetric drift) correction to circular velocity  $V_{\text{circ}}$ . We use the option for a self-gravitating exponential disk with constant velocity dispersion  $\sigma(R) = \sigma_0$ , such that

$$V_{\text{rot}}^2(R) = V_{\text{circ}}^2(R) - 3.36\sigma_0^2(R/R_e). \quad (1)$$

We note that the pressure support corrections derived from local galaxies (Dalcanton & Stilp 2010) and from simulations of high- $z$  galaxies (Kretschmer et al. 2021) predict more moderate corrections (see Bouché et al. 2022; Price et al. 2022). As discussed below, due to the lack of empirical evidence of strong radially varying velocity dispersions in SFGs at cosmic noon, here we choose to adopt the Burkert et al. (2010) prescription derived for isotropic dispersion and self-gravitating disks.

We choose the two-parameter NFW (Navarro, Frenk, & White 1996) profile for the DM halo. The virial mass  $M_{\text{vir}}$  is tied to the variable  $f_{\text{DM}}(< R_e)$ . The initial guess of  $M_{\text{vir}}$  is set by the expected value from the stellar-mass-halo-mass (SMHM) scaling relation from abundance matching (Moster et al. 2018), and  $\log(M_{\text{vir}}/M_\odot) \in [11.7, 12.1]$ . We then allow  $M_{\text{vir}}$  to vary by tying it to  $f_{\text{DM}}$ . The concentration parameter  $c_{\text{vir}}$  is fixed at a value following the  $M_{\text{vir}}-c_{\text{vir}}$  relation from Dutton & Macciò (2014), such that  $c_{\text{vir}} \in [3.4, 3.6]$ . We do not apply adiabatic contraction in our fits (Burkert et al. 2010).

`DysmalPy` assumes an isotropic velocity dispersion profile  $\sigma(R) = \sigma_0$ . It is motivated by empirical results from MS SFGs at  $z \sim 1-3$  (e.g. Genzel et al. 2011; Wuyts et al. 2016; Übler et al. 2019; Liu et al. 2023), in which  $\sigma(R)$  do not show strong trends with inclination and radius in high-resolution and high-S/N IFU observations, after accounting for beam-smearing effects. They also do not exhibit significant residuals after subtracting a constant profile, that would otherwise justify using a more complicated model for the dispersion profile. The  $\sigma_0$  is sensitive to the masking of spectral channels, especially for the S/N of the CRISTAL data (Davies et al. 2011; de Blok et al. 2024; Lee et al. 2025). Overly aggressive masking, which removes the fainter wings of the line emission, can result in a bias towards lower  $\sigma_0$  values. To avoid this bias entirely, we do not apply masking along the spectral axis. Instead, we evaluate the integrated S/N for each spaxel, and if the S/N falls below a threshold of  $\sim 3$ , we mask the entire spaxel.

The inclination ( $i$ ) of the galaxies is inferred from the intrinsic axis ratio of the *JWST*/NIRCam F444W image when available, or from the [C II] line emission map if not. The F444W-inferred inclinations are, on average,  $10^\circ$  more face-on than those inferred from the [C II] line emission map suggesting a possible overestimation of inclination when using the [C II] line emission map alone, even after accounting for beam convolution due to the elongated beam sizes and shapes.

The inclination is then derived from the axis ratio ( $\epsilon$ ) using the equation

$$\cos^2(i) = (\epsilon^2 - \epsilon_0^2)/(1 - \epsilon_0^2), \quad (2)$$

where  $\epsilon_0$  is the intrinsic axis ratio which we assume to be 0.25 (e.g. Wisnioski et al. 2019). The median inclination is  $54^\circ$ , which is essentially the same as the average over a population of randomly oriented disks (Law et al. 2009).

We simultaneously fit the 1D velocity and dispersion profiles extracted in § 3.2 along the kinematic major axis. This approach is preferred for our data over 2D and 3D methods, the latter are more demanding in terms of per-spaxel S/N and are more sensitive to non-circular motions. Since this work primarily focuses on the first-order kinematics of disks, the 1D approach is sufficient since the motion along the major axis best captures these properties (e.g. van der Kruit & Allen 1978; Genzel et al. 2017, 2020; Price et al. 2021). The extended radial coverage provided by the 1D method allows us to constrain  $\sigma_0$  at larger distances from the central region, thereby mitigating the effects of beam smearing and helping to resolve degeneracies in the model parameters, particularly those related to the relative contributions of baryons and dark matter to the observed RCs.

As demonstrated by Price et al. (2021) for  $z \sim 1-2.5$  MS galaxies, such a 1D approach is in broad agreement with 2D modelling. We additionally verify that the 3D and 1D methods agree within  $\sim 10\%$  if the per-pixel S/N within the effective radius is on average  $\geq 20$  within  $R_e$ , and in the worst case  $\sim 20\%$  if such S/N  $\leq 3$ . We note that while the terms 1D and 2D refer to the method of profile extraction from the data, `DysmalPy` always construct the model cube in full hypercube space when accounting for beam-smearing, projection, and spectral-broadening effects, as described above, irrespective of the extraction approach, and the full 3D information is used to identify the kinematic major axis. The model profile is then extracted from a 3D model cube in the same fashion as the data profiles are extracted from the observed data cube (see Fig. 6 in Price et al. 2021).

Since for all galaxies, the resolution and S/N of our data cannot provide constraints on many parameters, we leave four parameters free: (i) the baryonic mass  $\log_{10}(M_{\text{bary}}/M_\odot)$ , (ii) the disk effective radius  $R_{e,\text{disk}}$  (kpc), (iii) the enclosed dark matter fraction  $f_{\text{DM}}(< R_{e,\text{disk}})$ , and (iv) the velocity dispersion  $\sigma_0$  ( $\text{km s}^{-1}$ ). We employ Gaussian priors for  $\log_{10}(M_{\text{bary}}/M_\odot)$ , with a standard deviation of 1 dex centred on the sum of the stellar mass reported in Mitsuhashi et al. (2024) and Li et al. (2024) and the molecular gas mass derived in Appendix C. For  $R_{e,\text{disk}}$  (henceforth  $R_e$ ), we adopt Gaussian priors of standard deviation 1 kpc, centred on the fitted value of  $R_e$  of the [C II] emission measured in Ikeda et al. (2025). For CRISTAL-10a-E, 12 and 15, the quality of the data is not sufficient to constrain the  $R_e$ , we fix  $R_e$  to the [C II]-based radius. The prior range is tailored for each galaxy but generally spans  $[0, 10]$  kpc. We assume flat bounded priors for the intrinsic dispersion  $\sigma_0 \in [20, 200] \text{ km s}^{-1}$  and dark matter fraction  $f_{\text{DM}}(< R_{e,\text{disk}}) \in [0, 1]$ . Finally, we fix the geometrical parameters  $i$  and PA inferred from Eq. (2) and § 3.1, respectively. Other parameters are either tied, such as the disk scale height (through  $R_e$ ) and halo virial mass (through  $f_{\text{DM}}$ ), or fixed. We run `DysmalPy` with the `emcee` sampler, employing 512 walkers and a minimum of 200 burn-in steps followed by 1000 iterations. For all our fit, the final acceptance fraction is between 0.2 and 0.5 (mean = 0.32) and the chain is run for  $> 10\times$  (mean =  $23\times$ ) the maximum estimated parameter autocorrelation time (Foreman-Mackey et al. 2013).

We begin the first modelling without the bulge component given that the F444W/NIRCam data show no strong indication of

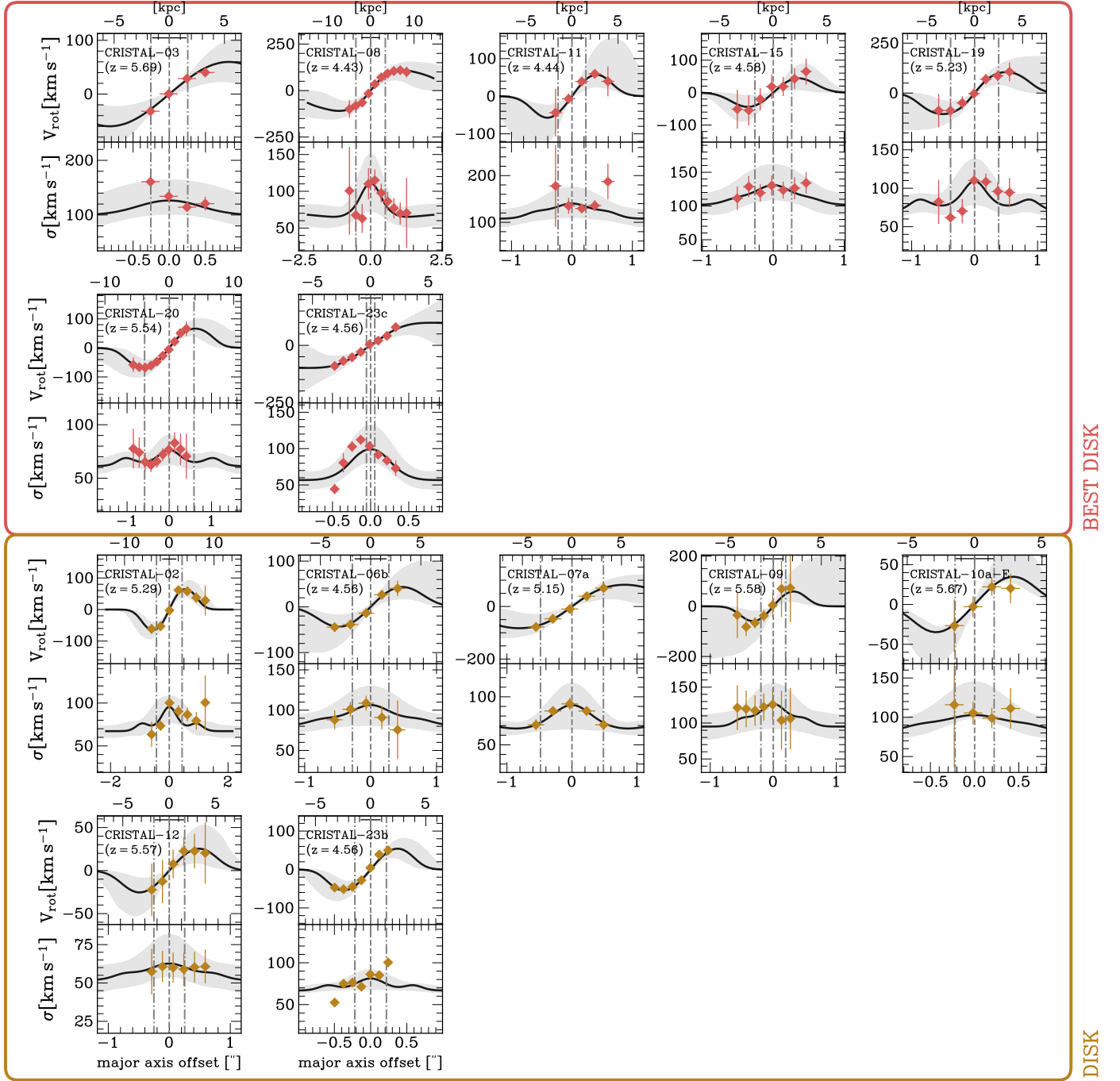


Fig. 6: Observed rotation curves (RCs) of the CRISTAL disk sample. The RCs are the fitted line velocity centroids of the position-velocity diagram extracted along the kinematic major axis. The RCs are grouped according to their kinematics types. The black curves are the extracted 1D model (in the same way as data) from the best-fit 3D model cube from *DysmalPy*. The 3D model cubes are projected and convolved with the beam, which give rise to the apparent central peak in the velocity dispersion profile and the shallower velocity profiles. The two symmetric grey vertical lines about the dynamical centre indicate the effective radius. The synthesised beam size is shown as the horizontal black line at the top. CRISTAL-05 and 22a belong to Disk, their velocity profiles are shown in [Posses et al. \(2025\)](#) and [Telikova et al. \(2025\)](#), respectively.

a bulge based on the relatively low Sérsic indices (Appendix B). For some galaxies, we observe a fair level of residuals between the data and the best-fit velocity and dispersion models in the central region, which could be evidence of a concentrated mass distribution deviating from the pure exponential disk profile. We therefore introduce a small, low-mass de Vaucouleurs bulge

component with a fixed Sérsic index ( $n_{\text{bulge}} = 4$ ) and an effective radius ( $R_{\text{e,b}} \leq 1$  kpc).

We iteratively increment the bulge-to-total ratio  $B/T$  in steps of 0.1. For all but 2 cases, a  $B/T = 0.1$  leads to the best fit in terms of reduced- $\chi^2$ . For two galaxies the preferred  $B/T \geq 0.3$  (CRISTAL-06b, as well as CRISTAL-05 modelled by [Posses et al. \(2025\)](#)).

Table 3: Best-fit properties from our dynamical models and molecular gas fractions

ID	$\log_{10}(M_{\text{tot}}/M_{\odot})^a$ (dex)	$R_{\text{e,disk}}^b$ (kpc)	B/T <sup>c</sup>	$V_{\text{rot}}(R_{\text{e}})^d$ (km s <sup>-1</sup> )	$\sigma_0^e$ (km s <sup>-1</sup> )	$f_{\text{DM}}(R_{\text{e}})^f$	$i^g$ (°)	$R_{\text{out}}/R_{\text{e,disk}}^h$	$R_{\text{out}}/\text{beam}^i$
02	10.5 <sup>+0.1</sup> <sub>-0.2</sub>	2.7 <sup>+0.5</sup> <sub>-0.5</sub>	0.1 <sup>+0.1</sup> <sub>-0.1</sub>	129.0 <sup>+36.6</sup> <sub>-37.2</sub>	67.1 <sup>+7.8</sup> <sub>-2.4</sub>	0.07 <sup>+0.31</sup> <sub>-0.06</sub>	[47.0]	3.0	5.5
03	10.4 <sup>+0.1</sup> <sub>-0.2</sub>	1.5 <sup>+0.9</sup> <sub>-0.2</sub>	[0.0]	165.3 <sup>+20.6</sup> <sub>-65.5</sub>	77.8 <sup>+28.5</sup> <sub>-0.2</sub>	0.09 <sup>+0.28</sup> <sub>-0.08</sub>	[67.0]	2.3	1.6
06b	10.5 <sup>+0.1</sup> <sub>-0.3</sub>	1.8 <sup>+0.7</sup> <sub>-0.7</sub>	[0.3]	136.3 <sup>+44.6</sup> <sub>-136.3</sub>	80.8 <sup>+12.5</sup> <sub>-6.4</sub>	0.08 <sup>+0.46</sup> <sub>-0.07</sub>	[43.0]	2.3	2.6
07a	10.2 <sup>+0.4</sup> <sub>-0.2</sub>	3.0 <sup>+0.9</sup> <sub>-1.0</sub>	0.1 <sup>+0.1</sup> <sub>-0.1</sub>	132.6 <sup>+41.7</sup> <sub>-73.5</sub>	63.1 <sup>+5.0</sup> <sub>-7.2</sub>	0.62 <sup>+0.28</sup> <sub>-0.29</sub>	[54.7]	1.4	2.2
08	10.5 <sup>+0.3</sup> <sub>-0.2</sub>	3.4 <sup>+0.9</sup> <sub>-0.9</sub>	0.1 <sup>+0.1</sup> <sub>-0.1</sub>	183.6 <sup>+50.2</sup> <sub>-61.0</sub>	62.4 <sup>+10.9</sup> <sub>-12.8</sub>	0.52 <sup>+0.28</sup> <sub>-0.29</sub>	[46.0]	2.6	4.1
09	10.4 <sup>+0.1</sup> <sub>-0.6</sub>	1.2 <sup>+0.2</sup> <sub>-0.2</sub>	0.1 <sup>+0.1</sup> <sub>-0.0</sub>	153.1 <sup>+70.0</sup> <sub>-153.1</sub>	93.2 <sup>+26.2</sup> <sub>-13.2</sub>	0.08 <sup>+0.52</sup> <sub>-0.07</sub>	[55.0]	3.1	3.7
10a-E	10.3 <sup>+0.0</sup> <sub>-0.2</sub>	[1.3]	[0.0]	111.8 <sup>+40.3</sup> <sub>-20.6</sub>	79.2 <sup>+13.1</sup> <sub>-9.0</sub>	0.05 <sup>+0.27</sup> <sub>-0.04</sub>	[80.0]	2.2	2.2
11	10.6 <sup>+0.1</sup> <sub>-0.3</sub>	1.5 <sup>+0.6</sup> <sub>-0.9</sub>	[0.0]	160.3 <sup>+47.9</sup> <sub>-98.9</sub>	107.8 <sup>+16.7</sup> <sub>-12.2</sub>	0.10 <sup>+0.27</sup> <sub>-0.09</sub>	[82.0]	2.9	3.3
12	9.7 <sup>+0.1</sup> <sub>-0.1</sub>	[1.5]	[0.0]	69.6 <sup>+32.9</sup> <sub>-69.6</sub>	48.5 <sup>+14.8</sup> <sub>-14.8</sub>	0.43 <sup>+0.12</sup> <sub>-0.12</sub>	[58.0]	2.6	2.7
15	10.5 <sup>+0.1</sup> <sub>-0.5</sub>	[1.7]	[0.1]	117.8 <sup>+45.1</sup> <sub>-117.8</sub>	100.5 <sup>+27.0</sup> <sub>-1.0</sub>	0.17 <sup>+0.35</sup> <sub>-0.16</sub>	[65.0]	2.4	3.3
19	10.5 <sup>+0.1</sup> <sub>-0.4</sub>	2.3 <sup>+0.4</sup> <sub>-0.2</sub>	0.1 <sup>+0.1</sup> <sub>-0.1</sub>	156.0 <sup>+50.3</sup> <sub>-81.5</sub>	70.3 <sup>+12.0</sup> <sub>-7.4</sub>	0.18 <sup>+0.45</sup> <sub>-0.13</sub>	[65.0]	1.7	3.7
20	10.3 <sup>+0.2</sup> <sub>-0.1</sub>	3.5 <sup>+0.9</sup> <sub>-0.6</sub>	[0.0]	98.7 <sup>+37.2</sup> <sub>-33.9</sub>	61.2 <sup>+3.8</sup> <sub>-6.7</sub>	0.43 <sup>+0.10</sup> <sub>-0.37</sub>	[64.4]	1.5	4.2
23b	9.8 <sup>+0.1</sup> <sub>-0.1</sub>	1.4 <sup>+0.2</sup> <sub>-0.2</sub>	[0.0]	93.3 <sup>+24.2</sup> <sub>-27.1</sub>	66.8 <sup>+2.0</sup> <sub>-2.5</sub>	0.57 <sup>+0.09</sup> <sub>-0.11</sub>	[60.9]	2.5	3.9
23c	9.2 <sup>+0.1</sup> <sub>-0.3</sub>	0.4 <sup>+0.1</sup> <sub>-0.1</sub>	0.1 <sup>+0.2</sup> <sub>-0.1</sub>	114.4 <sup>+17.3</sup> <sub>-34.8</sub>	56.5 <sup>+11.0</sup> <sub>-15.7</sub>	0.53 <sup>+0.23</sup> <sub>-0.05</sub>	[73.5]	9.2	3.7

**Notes.** From (a) to (h) are the best-fit (maximum a posteriori) parameters from *DysmalPy* modelling. Values in square brackets are fixed. The rotation velocity in (d) is the intrinsic total (baryons and dark matter) velocity defined in Equation 1. Inclinations in (g) are inferred from the *JWST*/F444W image, except for CRISTAL-10a, 20 and 23, which we infer from [C II] line flux map due to lack of NIRCcam data. The gas fraction  $f_{\text{molgas}}$  listed in (h) is estimated using the method outlined in Appendix C for galaxies with available dust continuum measurements. The  $1\sigma$  uncertainties from (a) to (f) are the distance to the shortest interval containing 68% of the marginalised posterior for each parameter (See Appendix A.2 in Price et al. 2021). The ratios in (h) and (i) represent the outermost measurable radius  $R_{\text{out}}$  (maximum radius on either the approaching or receding side) relative to the disk effective radius  $R_{\text{e,disk}}$  and the beam size in half-width-half-maximum, respectively. Best-fit values of CRISTAL-05 and 22a are presented in Posses et al. (2025) and Telikova et al. (2025), respectively.

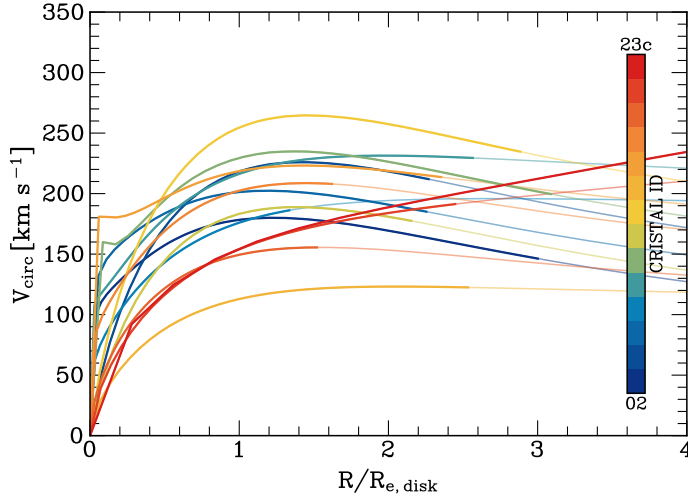


Fig. 7: Intrinsic total circular velocity profiles  $V_{\text{circ}}(R/R_{\text{e,disk}})$  of all CRISTAL disks, corrected for beam-smearing and projection effects. Colours, in ascending order, represent the CRISTAL ID (first column in Table 3). The individual  $V_{\text{circ}}(R)$  of baryons and dark matter are presented in Figure E.1 in Appendix E. Thin, lighter-coloured lines indicate the radial range beyond which the data is not covered.

We compare in Fig. 6 the observed and best-fit (projected and beam-smear) model RCs for the CRISTAL disks. The intrinsic circular velocity profiles  $V_{\text{circ}}(R)$  of the models are shown in Fig. 7, with the maximum radial coverage of the data indicated. Fig. E.1 in Appendix E shows the intrinsic  $\sigma_0$ , circular velocity profiles of the DM and the baryonic components. For all systems, except CRISTAL-01b, 07a, 08, 19, 23b and 23c, we observe a fall-off of circular velocities, indicative of masses dominated by

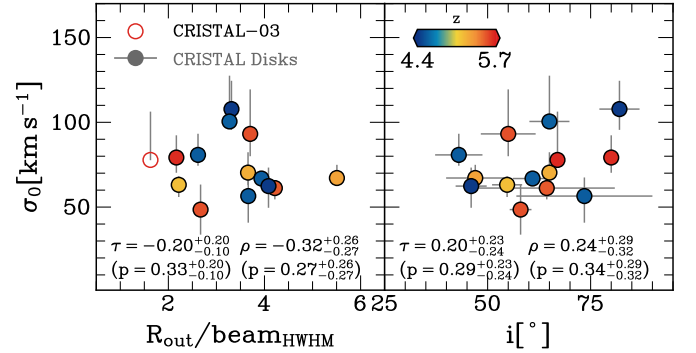


Fig. 8: Intrinsic velocity dispersion  $\sigma_0$  as a function of the number of resolution elements within the outermost measurable radius  $R_{\text{out}}$  and inclination ( $i$ ). The Spearman and Kendall rank correlation coefficients ( $\rho$  and  $\tau$ , respectively) do not indicate a significant correlation of  $\sigma_0$  with the inclination and resolution effects, though the uncertainties in both the coefficients and  $p$ -value are large. CRISTAL-03 which has  $R_{\text{out}}/\text{beam}_{\text{HWHM}} = 1.6$  is excluded in the correlation analysis in § 6.2.

the baryonic components. We will discuss the DM fractions of the samples later in § 7.

We examine the potential dependence of  $\sigma_0$  on the angular resolution relative to the galaxies' sizes and  $i$ . Table 3 lists the ratios of  $R_{\text{out}}$  to the beam size (geometric average of the values in Table 1) in terms of half-width-half maximum ( $\text{beam}_{\text{HWHM}}$ ).  $R_{\text{out}}$  represents the outermost radius at which we can reliably extract velocity and dispersion profiles using the method described in § 3.2. Overall, the kinematics profiles are traced out to  $\sim 1.5\text{--}3R_{\text{e}}$  ( $\sim 9R_{\text{e}}$  for CRISTAL-23c), with  $R_{\text{out}}/\text{beam}_{\text{HWHM}} \sim 2\text{--}4$  (5.5 for CRISTAL-02). Lee et al. (2025) has tested these requirements are sufficient to recover  $V_{\text{rot}}$  and  $\sigma_0$  with a large suite of mock



galaxies having comparable angular resolution and S/N to the CRISTAL data, provided that the adopted parametric profiles are close to the intrinsic profiles.

We perform Spearman and Kendall rank correlation tests (Fig. 8) to investigate the relationships between  $\sigma_0$ – $R_{\text{out}}/\text{beam}_{\text{HWHM}}$  as well as  $\sigma_0$ – $i$ . We do not detect significant correlations in either case (similarly for  $\sigma_0$ – $R_e/\text{beam}_{\text{HWHM}}$ ). The small sample size, however, would only allow to detect stronger correlations if present.

We conservatively exclude the least-resolved CRISTAL-03 in the correlation analysis in § 6.2, which has  $R_{\text{out}}/\text{beam}_{\text{HWHM}} = 1.6$ . For this galaxy, the  $5\times$  better angular resolution NIRSpec/JWST data reveals a consistent rotational pattern in  $H\alpha$  (W. Ren et al., in prep.).

## 6. Disk turbulence and dynamical support

### 6.1. Comparison to other samples and redshift trends

To put CRISTAL disks' kinematics in the context of dynamical evolution over cosmic time, we present in Fig. 9 the intrinsic dispersion  $\sigma_0$  and the dynamical support from  $V_{\text{rot}}/\sigma_0$ , compared with literature values from local to distant galaxies up to  $z \lesssim 8$ . The data points are coded according to the MS offset  $\Delta\text{MS}$  of the galaxies, and different symbols distinguish measurements based on tracers of atomic, cold molecular, warm, and ionised gas phases.

The literature compilation is listed in Appendix D Table D.1. It includes studies of local galaxies and local analogues observed in H I, CO,  $H\alpha$  or [O II], as well as unlensed and lensed galaxies at  $0.5 < z < 4$  traced by CO, [C I],  $H\alpha$ , [O III] or [C II], and at  $z \geq 4$  traced by  $H\alpha$ , CO, [C II], [O III], or [C III]. We only consider the systems classified as disk-like. We exclude those measurements with uncertainties in  $\sigma$  and  $V_{\text{rot}}$  greater than 50%, but include all disks in CRISTAL without this cut.

The definition and methodology employed for  $V_{\text{rot}}$  and  $\sigma_0$  vary between studies. In cases where  $V_{\text{rot}}$  is not available at  $R_e$  is not available,  $V_{\text{rot}}$  is taken as the maximum velocity  $V_{\text{max}}$  or  $V_{\text{rot}}(2.2R_e)$ . For parametric modelling, the profiles adopted for  $V_{\text{rot}}$  include arctan and the multi-parameter function from Courteau (1997). The definition of  $\sigma$  also varies across literature; for non-parametric modelling, such as using <sup>3D</sup>Barolo (Di Teodoro & Fraternali 2015) or KinMS (Davis et al. 2013, 2017), it would be either the median or mean of the radial profile; for parametric modelling, which assumed either a constant profile  $\sigma(R) = \sigma_0$ ,  $\sigma(R) = \sigma_0 \exp(-R/R_c)$  or other functions, we adopt the  $\sigma_0$  or the median in the latter cases, following the choice of the original authors. The literature values are also a mix of data obtained from various observational methods, including IFU, interferometry, and slit spectroscopy. The slit-based method tends to give higher  $\sigma$  values than the other two (Übler et al. 2019). Different CO transitions can also trace gas with various kinematic and spatial properties.

We recalculate  $\Delta\text{MS}$  using the relation of Speagle et al. (2014), extrapolated to the redshift range of the samples. Recent studies of the star-forming main sequence at  $z \gtrsim 5$ , utilising JWST imaging data, have provided support for this extrapolated relationship (Cole et al. 2025; Koprowski et al. 2024). When available, the stellar mass  $M_\star$  values are taken directly from the literature, which was derived from spectral energy distribution (SED) fitting using various tools and assuming different initial mass functions (IMFs) or decomposition of RC. In cases where  $M_\star$  is not reported, we estimate it from the dynamical and gas mass ( $M_\star = M_{\text{dyn}} - M_{\text{gas}}$ ).

In Fig. 9, the literature values of  $\sigma_0$  in ionised and molecular gas tracers are both displaying an overall increasing trend with redshift. For MS galaxies up to  $z \sim 4$ , the trends are well-described by the best-fit relations derived by Übler et al. (2019). Qualitatively, extrapolating these relations matches the evolutionary trend at even higher redshifts for the MS galaxies and agrees well with the CRISTAL values. On the other hand, some starburst galaxies observed with [C II] at similar epochs lie below the extrapolated relationships.

Sample selection differences between studies could partly explain the large spread in  $\sigma_0$  (and  $V_{\text{rot}}/\sigma_0$ ). As extensively discussed by Wisnioski et al. (2025), the interpretation of the dispersion should also consider the different ISM phases probed by the various kinematic tracers and, relatedly, the varying contributions of different gas phases to the [C II] line emission as a function of  $\Sigma_{\text{SFR}}$  and other properties (e.g. Cormier et al. 2019; Wolfire et al. 2022; Ikeda et al. 2025). To better understand the potential dependence on ISM phases, it is essential to study the same object using multiple tracers; currently, this has only been done for a limited number of samples (Table D.2), as highlighted in the insets of Fig. 9.

Compared to unlensed MS SFGs observed with [C II] at similar epochs, CRISTAL disks have comparable values of  $\sigma_0$  within uncertainties, with a median difference of  $11 \text{ km s}^{-1}$ , and a lower  $V_{\text{rot}}/\sigma_0$  by 0.8 in median. This is possibly because CRISTAL disks are less massive in  $M_\star$  than the literature samples by an average of 0.15 dex. Given the mass-dependence of  $V_{\text{rot}}/\sigma$  in simulations that span a wider dynamic range (e.g. Dekel et al. 2020; Kohandel et al. 2024) than allowed by our data, the lower mass of our sample may explain the lower  $V_{\text{rot}}/\sigma_0$  values. When compared with the same population observed in ionised gas, now possible thanks to JWST, CRISTAL disks are in very good agreement with the ‘gold’ sample in Danhaive et al. (2025), with median differences of only  $\sim 2\%$  in  $\sigma_0$  and  $\sim 10\%$  in  $V_{\text{rot}}(R_e)/\sigma_0$ .

On the other hand, compared with the lensed samples, CRISTAL disks have higher  $\sigma_0$ , by  $34 \text{ km s}^{-1}$  in median, and significantly lower  $V_{\text{rot}}/\sigma_0$  by  $-6$ . In particular, the lensed samples tend to be starburst galaxies, and have smaller sizes (with  $R_e$  typically  $\lesssim 1.5 \text{ kpc}$ , see also Fig. 1) that are  $\sim 50\%$  and  $\sim 70\%$  smaller than the unlensed galaxies and CRISTAL disks, respectively. The starburst and compact nature of these galaxies suggest that they have experienced a distinct assembly history (Stach et al. 2018; Hayward et al. 2021), differing from that of the more typical galaxy populations in CRISTAL.

### 6.2. Trends with galaxy properties

We explore here trends with galaxy properties, including molecular gas mass fraction ( $f_{\text{molgas}}$ ), stellar mass ( $M_\star$ ), MS offset ( $\Delta\text{MS}$ ), SFR surface density ( $\Sigma_{\text{SFR}}$ ), and molecular gas mass ( $M_{\text{gas}}$ ). Fig. 10 plots the derived  $\sigma_0$  and  $V_{\text{rot}}/\sigma_0$  as a function of these properties for the CRISTAL disk sample. We quantify the correlations by computing the Spearman's  $\rho$  and Kendall's  $\tau$ , and their  $p$ -values to assess the significance of any possible correlations. The resulting coefficients and the  $p$ -values with confidence intervals are annotated in Fig. 10.

For  $\sigma_0$ , the strongest correlation observed is with  $f_{\text{molgas}}$ . The  $V_{\text{rot}}/\sigma_0$  appears to correlate most importantly with  $\Delta\text{MS}$ . No other obvious trend is detected with the other galaxy properties. The dependence of  $\sigma_0$  with  $f_{\text{molgas}}$  is in line with expectations for marginally stable, gas rich disks as discussed in § 6.1. The trend between  $V_{\text{rot}}/\sigma_0$  and  $\Delta\text{MS}$  may reflect an underlying dependence on  $\Sigma_{\text{bar}}$  (see also the right panel of Fig. 1). However, although the correlation coefficient  $\rho$  between  $V_{\text{rot}}/\sigma_0$  and  $\Sigma_{\text{bar}}$  is  $\sim 0.5$ ,

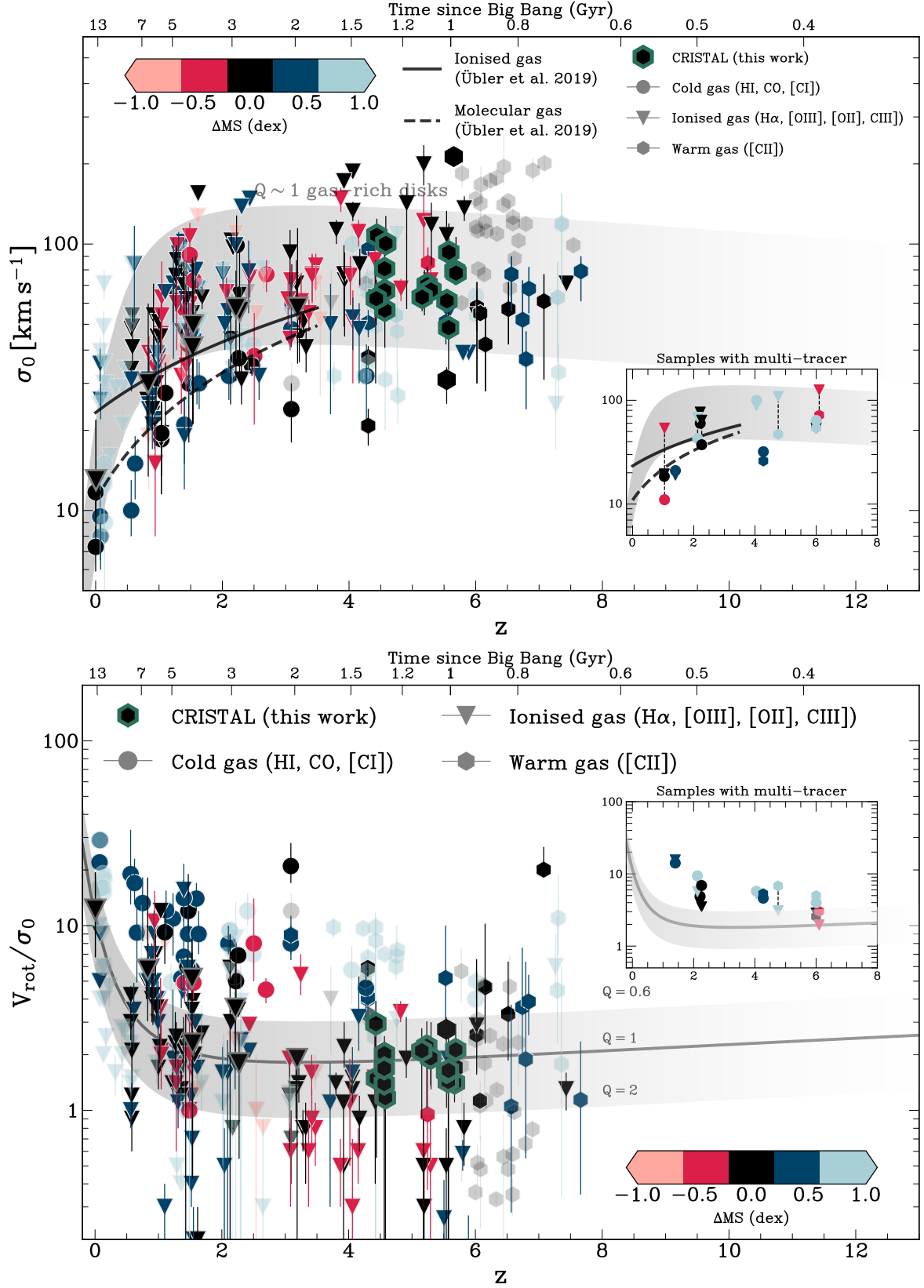


Fig. 9: Dynamical evolution of high- $z$  galaxies. *Top*: Intrinsic velocity dispersion  $\sigma_0$  as a function of redshift for our disk sample (black hexagons with green outline) compared with the literature values (see Appendix D Table D.1). *Bottom*: Same but for the ratio between rotational velocity and  $\sigma_0$ ,  $V_{\text{rot}}/\sigma_0$ . The solid and dashed black lines are the Übler et al. (2019)’s best-fit relations for galaxies at  $z < 4$ , for ionised and cold molecular gas, respectively. Where available, the points are colour-coded by their main-sequence offset  $\Delta MS$  relative to the Speagle et al. (2014) relation, otherwise in grey. The insets show the literature sample (see Table D.2) of the same galaxy with two gas tracers tracing different phases. The insets include the galaxies with large uncertainties which are omitted in the main plots. The grey shading encloses the corresponding range in  $\sigma_0$  and  $V_{\text{rot}}/\sigma_0$  for  $Q \in [0.6, 2.0]$ . The definition of the Toomre  $Q$  parameter is presented in § 6.3.

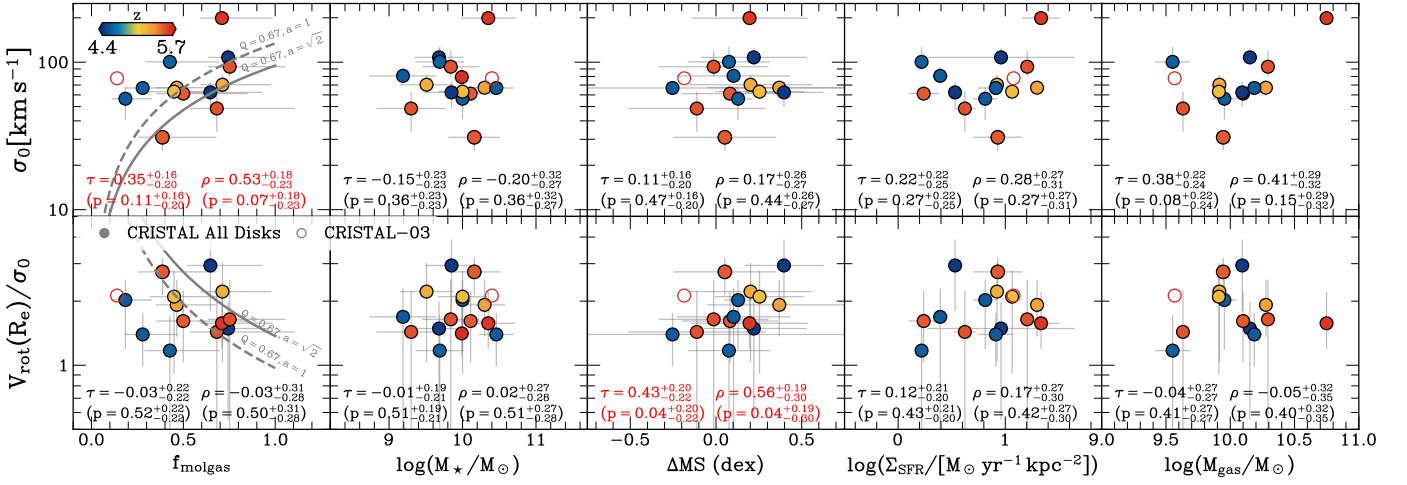


Fig. 10: Intrinsic velocity dispersion ( $\sigma_0$ ) and the ratio of rotation velocity at the effective radius ( $V_{\text{rot}}(R_e)$ ) to intrinsic velocity dispersion ( $\sigma_0$ ) as a function of five galaxy properties: molecular gas fraction ( $f_{\text{molgas}}$ ), stellar mass ( $\log(M_*/M_\odot)$ ), offset from the main sequence ( $\Delta\text{MS}$ ), star formation rate surface density ( $\Sigma_{\text{SFR}}$ ), and molecular gas mass ( $\log(M_{\text{gas}}/M_\odot)$ ). The dashed and solid grey curves in the first column are the predicted trends based on Equation 3 with  $Q$  fixed at  $Q_{\text{crit}} = 0.67$ , with  $a = 1$  and  $a = \sqrt{2}$ , respectively. The Kendall and Spearman's rank correlation coefficients ( $\tau$  and  $\rho$ ) and their corresponding  $p$ -values are shown alongside the  $1\text{-}\sigma$  percentile errors. Taken  $\sigma_0$  at face values, it shows a tentative correlation (highlighted in red) with  $f_{\text{molgas}}$ , while  $V_{\text{rot}}(R_e)$  correlates most significantly with  $\Delta\text{MS}$ . The most poorly resolved galaxy CRISTAL-03 (empty red circle), with an extent covered by  $< 2$  beams, is excluded from the correlation analysis. The limited statistics and narrow parameter range of our data lead to large uncertainties in the correlation coefficients and their  $p$ -values, and the trends should be interpreted with caution.

the large accompanying  $p$ -value suggests that more precise size measurements are required to confirm this relationship. Clearly, the CRISTAL disk sample is small and only the strongest correlations can be discerned. Future larger samples of near MS SFGs at  $z \sim 4\text{--}6$  will be important to strengthen the results, such as the literature compilation efforts by Wisnioski et al. (2025).

### 6.3. Turbulence in the framework of marginally Toomre-stable disks

The observed evolutionary trend of  $\sigma_0$  and  $V_{\text{rot}}/\sigma_0$  discussed above has been attributed to the increasing gas fraction at higher redshifts (e.g. Tacconi et al. 2010; Tacconi et al. 2020), as predicted by Toomre theory. The correlation of  $\sigma_0$  with  $f_{\text{molgas}}$  for the CRISTAL disks discussed above also is in line with expectations for marginally stable gas-rich disks. In this framework, the stability of the disks against fragmentation and local gravitational collapse is directly linked to the level of turbulence in the ISM. Turbulence is driven by both *ex-situ*, such as accretion from the cosmic web, and *in-situ*, including radial flows and clump migration, which release gravitational potential energy. This creates a self-regulating cycle that maintains the disk in a state of marginal stability. Following Eq. (3) in Genzel et al. (2014) (see also, Übler et al. 2019; Genzel et al. 2011, 2023; Liu et al. 2023), the classical Toomre (1964) parameter  $Q$  can be formulated as:

$$Q_{\text{gas}} = \frac{\sigma_0 \kappa}{\pi G \Sigma_{\text{gas}}} = \left( \frac{\sigma_0}{v_c} \right) \left( \frac{a}{f_{\text{gas}}} \right), \quad (3)$$

where the epicyclic frequency is  $\kappa = \sqrt{R d\Omega^2/dR + 4\Omega^2}$  and  $\Omega = V_{\text{rot}}/R$ . The constant  $a$  depends on the rotational structure of the disk:  $a = \sqrt{1}$  for Keplerian-like rotation and  $a = \sqrt{2}$  for a disk with constant rotational velocity. For a quasi-stable thick gas disk,  $Q_{\text{crit}} = 0.67$  (e.g. Behrendt et al. 2015). The two panels in the first column of Fig. 10 plot the predicted trends of  $\sigma(f_{\text{gas}})$  and

$V_{\text{rot}}/\sigma(f_{\text{gas}})$  based on Eq. (3) with  $Q = Q_{\text{crit}}$  and  $a = \sqrt{1\text{--}2}$ , taking into account that some RCs show a drop-off. Overall, there is a good match between the predicted trend and the CRISTAL values.

Specifically, taking the median values of CRISTAL disks,  $\sigma_0/v_c = 70/200 = 0.4$  and  $f_{\text{molgas}} \sim 0.5$ . The corresponding values of  $Q_{\text{gas}}$  is then 0.6, and the entire sample has  $Q$  in the range  $[0.4, 2.0]$ , indicating that the CRISTAL disks are, on average, marginally gravitationally stable. The  $Q$  values are broadly similar to the results of Übler et al. (2019) for their  $z \sim 1\text{--}3$  samples. The similar Toomre  $Q$  values inferred for MS SFGs from  $z \sim 5$  to  $z \sim 1$  in MS SFGs suggests that this galaxy population has grown in a marginally stable and self-regulating manner for at least 5 billion years of cosmic time.

From a broader evolutionary perspective based on the Toomre theory for gas-rich disks, the observed trends from the literature combining with CRISTAL are in remarkably good agreement. The grey bands in both panels of Fig. 9 show the prediction in the Toomre framework for the evolution of dispersion for  $\log(M_*/M_\odot) = 10.0$  galaxies with  $Q_{\text{crit}} \in [0.4, 2.0]$  and  $v_c = 200 \text{ km s}^{-1}$ . These values are appropriate for the CRISTAL disk sample (and differ from more massive samples studied at lower redshifts, e.g., Wisnioski et al. 2015). The gas fraction  $f_{\text{molgas}}$  adopted evolves according to the scaling relation in Tacconi et al. (2020) which is a function of stellar mass, SFR, and size. The SFR and size evolution with redshift is determined from the Speagle et al. (2014) MS relation and van der Wel et al. (2014) mass-size relation. CRISTAL galaxies have  $f_{\text{molgas}} \sim 51\%$ , consistent with the expected value from Tacconi et al. (2020)'s relation at  $z = 5$  for  $M_* = 10^{10} M_\odot$ , which is  $\sim 53\%$  (see discussions in Appendix C).

#### 6.4. Drivers of the gas turbulence

To explore the relative contribution of star formation- versus gravitational instability-driven turbulence in CRISTAL disks, we compare our results with the analytic model of Krumholz et al. (2018). This model combines stellar feedback and gravitational processes to drive turbulence, incorporating prescriptions for star formation, stellar feedback, and gravitational instabilities into a unified ‘transport+feedback’ framework. In the model, gas is in vertical hydrostatic equilibrium and energy equilibrium, with energy losses through turbulence decay balanced by energy input from stellar feedback and the release of gravitational energy via mass transport through the disk. Based on the model, there is a critical value of gas velocity dispersion ( $\sigma_g$ ),  $\sigma_{sf}$ , at which the amount of turbulence can be sustained by star formation alone, without the need for gravitational instability or radial transport. In such a case,  $\sigma_g$  is related to  $\sigma_{sf}$  by (Eq. (39) in Krumholz et al. 2018)

$$\sigma_g = \sigma_{sf} \equiv \frac{4f_{SF}\epsilon_{ff}}{\sqrt{3f_{g,P}\pi\eta\phi_{mp}\phi_Q\phi_{nt}^{3/2}}} \left\langle \frac{p_*}{m_*} \right\rangle \cdot \max \left[ 1, \sqrt{\frac{3f_{g,P}}{8(1+\beta)}} \frac{Q_{min}\phi_{mp}}{4f_{g,Q}\epsilon_{ff}} \frac{t_{orb}}{t_{sf,max}} \right]. \quad (4)$$

Following Table 3 in Krumholz et al. (2018) for high- $z$  galaxies, the fraction of ISM in the star-forming molecular phase,  $f_{SF}$ , is set to 1.0;  $t_{SF,max} = 2$  Gyr; the fractional contribution of gas to the mid-plane pressure and  $Q$ ,  $f_{g,P}$  and  $f_{g,Q}$ , respectively, are both assumed to be 0.7; the slope index of the RC,  $\beta = d \ln v_\phi / d \ln r$ , is set to 0.0 (i.e., flat), in which  $v_\phi$  is the circular velocity  $V_{circ}$ ; the Toomre parameter,  $Q$ , is fixed at 1, following the fiducial value. The orbital period  $t_{orb} = 2\pi r / V_{circ} \in [30, 120]$  Myr, and is adjusted to the values of our sample. The other values that we adopt are listed in Table F.1 in Appendix F. The  $\sigma_g$  from Eq. (4) is therefore  $\sim 10 \text{ km s}^{-1}$ . Dispersion much larger than this critical value ( $\geq 20 \text{ km s}^{-1}$ ) requires gravitational instability or radial mass transport for moderate SFR.

In the ‘transport+feedback’ model, the star formation rate surface density  $\Sigma_{SFR}$  and the gas velocity dispersion  $\sigma_g$  can be related as (Eq. (59) in Krumholz et al. 2018):

$$\Sigma_{SFR} = f_{SF} \frac{\sqrt{8(1+\beta)}f_{g,Q}}{GQ} \frac{\sigma_g}{t_{orb}^2} \cdot \max \left[ \frac{8\epsilon_{ff}f_{g,Q}}{Q} \sqrt{\frac{2(1+\beta)}{3f_{g,P}\phi_{mp}}} \frac{t_{orb}}{t_{SF,max}}, 1 \right], \quad (5)$$

while for ‘feedback-only’ (fixed  $Q$ ) model (Eq. (61) in Krumholz et al. 2018):

$$\Sigma_{SFR} = \frac{8(1+\beta)\pi\eta\sqrt{\phi_{mp}\phi_{nt}^3}\phi_Q}{GQ^2\langle p_*/m_* \rangle f_{g,P}} \frac{\sigma_g^2}{t_{orb}^2}. \quad (6)$$

In Fig. 11 we show the  $\sigma_0$ - $\Sigma_{SFR}$ <sup>3</sup> measurements of CRISTAL disks, compared with the ‘transport+feedback’ and ‘feedback only’ model of Krumholz et al. (2018). For reference, we also compare  $\sigma_0$  and SFR in Appendix F. Overall, our results are broadly consistent with the ‘feedback+transport’ model of Krumholz et al. (2018), which suggests that the high-velocity

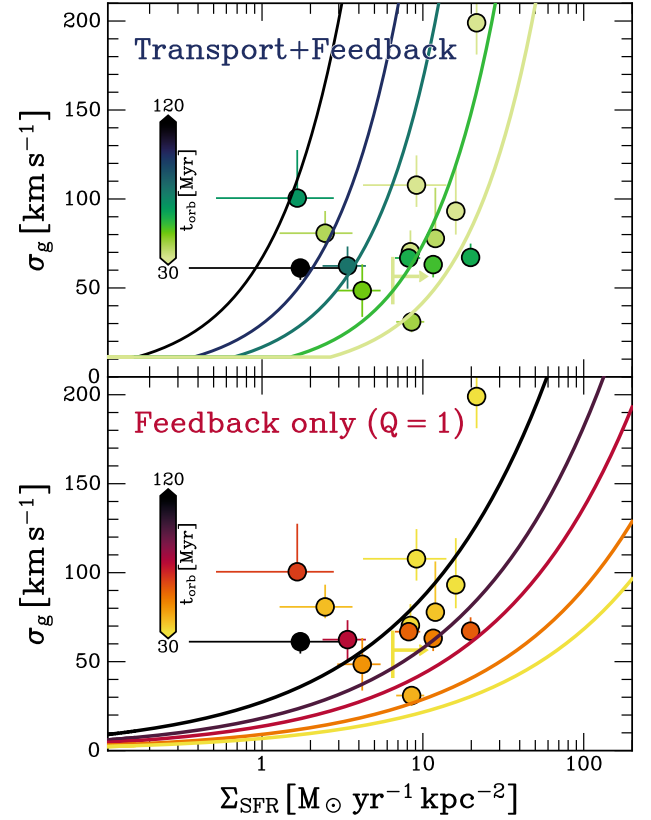


Fig. 11:  $\sigma_0$  vs  $\Sigma_{SFR}$  of CRISTAL disks compared with analytical models from Krumholz et al. (2018). The solid lines in the upper panel show the  $\sigma_0$  values predicted from the Transport+Feedback model with orbital period  $t_{orb} = [30, 120]$  Myr. Similarly for the lower panel but for the ‘Feedback-only’ model. The results are broadly consistent with the ‘feedback+transport’ model, suggesting that the elevated velocity dispersion of normal star-forming galaxies at this epoch requires additional gravitational energy from mass transport across the disk.

dispersion of normal SFGs can be predominantly attributed to the release of gravitational energy from mass transport across the disk.

This result differs from some previous studies at similar epochs, which found that star formation feedback alone can sustain the observed dispersion in starburst-like galaxies (e.g. Roman-Oliveira et al. 2023; Rowland et al. 2024). However, our analysis of CRISTAL MS disks, characterised by modest star formation activity, indicates that a different dominant mechanism drives turbulence in the ISM of MS SFGs.

The result is nevertheless consistent with the weak correlation of  $\sigma$  with global or local SFR ( $\Sigma_{SFR}$ ) of our sample as shown in § 6.2. Such a weak correlation is also found in Genzel et al. (2011); Johnson et al. (2018) and Übler et al. (2019) for cosmic noon galaxies (after redshift normalisation), and in the nearby universe (e.g. Elmegreen et al. 2022). This is also in agreement with the theoretical works (e.g. Shetty & Ostriker 2012; Kim & Ostriker 2018), which have derived a weak dependence of gas velocity dispersion on the supernova explosion rate.

We note, however, that for CRISTAL-05 with its relatively low  $\sigma_0 \approx 31 \text{ km s}^{-1}$  and  $\Sigma_{SFR} = 8.5 \text{ M}_\odot \text{ yr}^{-1} \text{ kpc}^{-2}$  ( $\text{SFR} = 68 \text{ M}_\odot \text{ yr}^{-1}$ ), the stellar feedback-only model would better match the observed values of  $\sigma_0$  and  $\Sigma_{SFR}$  (and SFR), suggesting that different mechanisms among the disk samples

<sup>3</sup> For CRISTAL-23c in which the  $\Sigma_{SFR}$  is not available, we adopt the  $\Sigma_{SFR,IR}$  from Béthermin et al. (2023) as a lower limit, although the contribution from unobscured star formation is not significant.



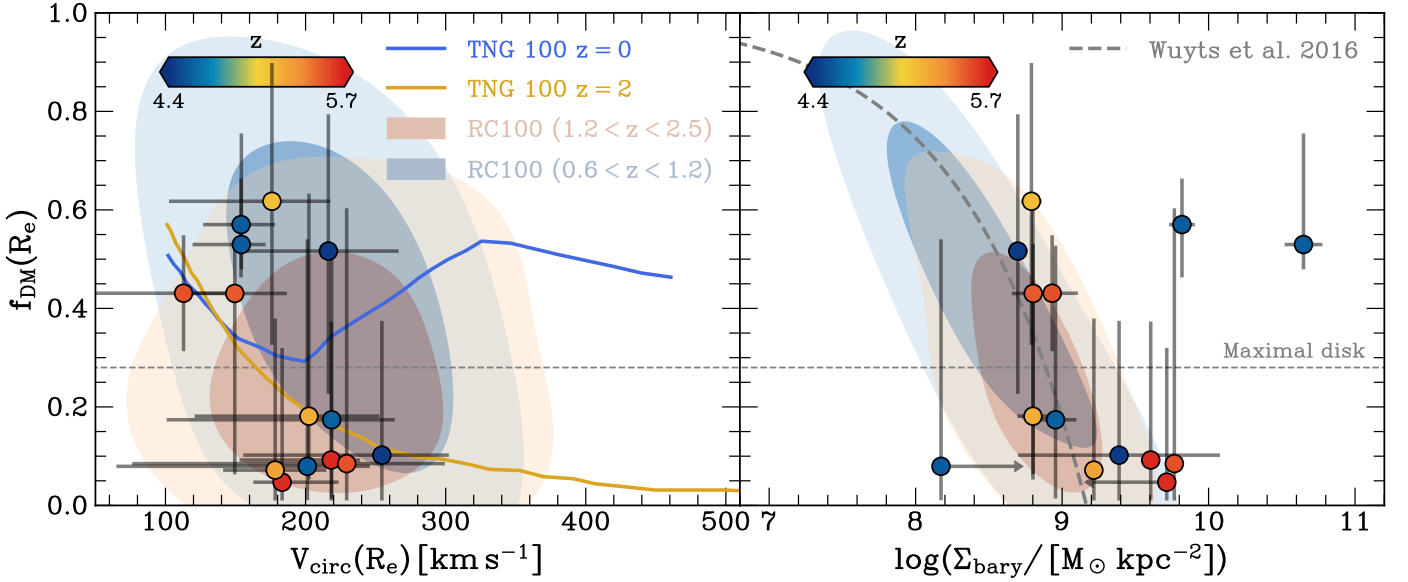


Fig. 12: Dark matter (DM) fraction  $f_{\text{DM}}$  as a function of the circular velocity at the effective radius ( $V_{\text{circ}}(R_e)$ , *left*) and baryonic surface density ( $\Sigma_{\text{bary}}$ ) (*right*). The yellow and blue curves show the TNG100 (without adiabatic contraction) relations at  $z=0$  and  $z=2$  (Lovell et al. 2018), respectively. The pale blue and yellow shading are measurements from RC100 at  $z < 2.5$  (Nestor Shachar et al. 2023). The grey dashed curve is the best-fit relation of  $z \sim 2$  star-forming galaxies from Wuyts et al. (2016). The CRISTAL sample statistics suggest a tentative anti-correlation with  $f_{\text{DM}}(R_e)$  and  $\Sigma_{\text{bary}}$ , although individual galaxy uncertainties are limited by the data depth. The horizontal dashed line denotes  $f_{\text{DM}}$  for a maximal disk  $f_{\text{DM}} := 28\%$  (van Albada et al. 1985). In the *right* panel, the two symbols plotted with only limit arrows represent CRISTAL-10a-E (upper limit) and CRISTAL-06b (lower limit). The stellar mass is only for CRISTAL-10a as a whole, which includes CRISTAL-10a-E, while no gas mass is available for CRISTAL-06b.

may contribute to varying degrees of the observed velocity dispersion, as seen also in simulations (e.g. Jiménez et al. 2023). Additionally, spatial variation of different mechanisms within a single galaxy is also possible, but the resolution of our data is currently insufficient to reveal such variation conclusively. In the future, higher resolution observations of kinematics and SFR maps would enable to test more directly the coupling (or lack thereof) between  $\sigma_0$  and stellar feedback. Other simulation works also show that stellar feedback can sustain higher dispersions compared to the Krumholz et al. 2018’s analytical treatment (Gatto et al. 2015; Orr et al. 2020; Rathjen et al. 2023). The relative contribution of stellar feedback versus gas transport depends on halo mass and redshift, in which gas transport plays a more dominant role in the high redshift systems (Ginzburg et al. 2022).

## 7. Exploration of galactic DM fraction and mass budget

On the galactic scale, CRISTAL disks tend to be baryonic-dominated, with low  $f_{\text{DM}}$  at  $R_e$  (Table 3), having a median value of 18% (mean = 27%), comparable to or less than maximal disks ( $f_{\text{DM}} := 28\%$  van Albada et al. 1985), albeit with significant scatter among the samples that span a wider range from a few % to  $\sim 60\%$ . In comparison, the Galaxy’s  $f_{\text{DM}}(R_e) = 0.38 \pm 0.1$  (Bovy & Rix 2013; Bland-Hawthorn & Gerhard 2016).

The radial profiles of  $f_{\text{DM}}$  of CRISTAL disks are shown in Fig. E.1, which is defined in `DysmalPy` as <sup>4</sup>

$$f_{\text{DM}}(< R) := V_{\text{circ,DM}}^2(R) / V_{\text{circ,tot}}^2(R). \quad (7)$$

<sup>4</sup> We note that in our analysis,  $f_{\text{DM}}$  at  $R_{e,\text{disk}}$  is a free parameter — by instead calculating the total halo mass given the specified baryonic mass distribution and  $f_{\text{DM}}(R_{e,\text{disk}})$ , the full  $f_{\text{DM}}$  radial profile for each galaxy is

We observe a tentative inverse relationship between  $f_{\text{DM}}(R_e)$  and circular velocity ( $V_{\text{circ}}$ ) in Fig. 12, which is pressure-support corrected (Eq. (1)), and similarly for the baryonic surface density  $\Sigma_{\text{bary}}$  based on the values in Tables 1 and 2. This trend is similar to that observed in Nestor Shachar et al. (2023) for cosmic noon MS SFGs. Such an inverse correlation is well-established for local SFGs, where the most DM-dominated disks are those with low baryonic mass surface density and circular velocity (e.g. Martinsson et al. 2013a,b; Courteau & Dutton 2015, and references therein). We also compare our results to Wuyts et al. (2016), who derived  $f_{\text{DM}}$  at the inner disk by subtracting the sum of stellar and gas masses from the dynamical mass obtained from RCs of 240 galaxies, assuming  $f_{\text{bary}} = M_{\text{bary}}/M_{\text{dyn}} = 1 - f_{\text{DM}}$ . We find that most of the CRISTAL disks follow the Wuyts et al. (2016) relation on the  $\Sigma_{\text{bary}}-f_{\text{DM}}$  plane, except for CRISTAL-23b, and 23c, which are both disk-like galaxies in an interacting system.

The low  $f_{\text{DM}}(R_e)$  of our sample is broadly consistent with the general trend of decreasing DM fraction towards higher redshifts. Fig. 13 shows the median  $f_{\text{DM}}(R_e)$  of our sample aligns with the extrapolated trend toward higher redshift from Nestor Shachar et al. (2023) and Wuyts et al. (2016), when considering a sample matched in  $M_{\text{bary}}$  and  $\Delta\text{MS}$ . Both  $f_{\text{DM}}$  are below the expectations from the TNG100 simulation from Lovell et al. (2018). This could be due to the insufficient physical resolution of large-scale cosmological simulation to resolve sub-galactic processes (Übler et al. 2021) and the effect of adiabatic contraction (Blumenthal et al. 1986). The possible drivers of DM deficit in MS SFGs have been discussed thoroughly by, e.g. Genzel et al. 2020 and Nestor Shachar et al. 2023. It is potentially linked to kinetic heating due to the efficient transport of baryons to cen-

then computed given the best-fit parameters ( $M_{\text{bar}}$ ,  $R_{e,\text{disk}}$ ,  $f_{\text{DM}}$  enclosed within  $R_e$ , and  $\sigma_0$ ).

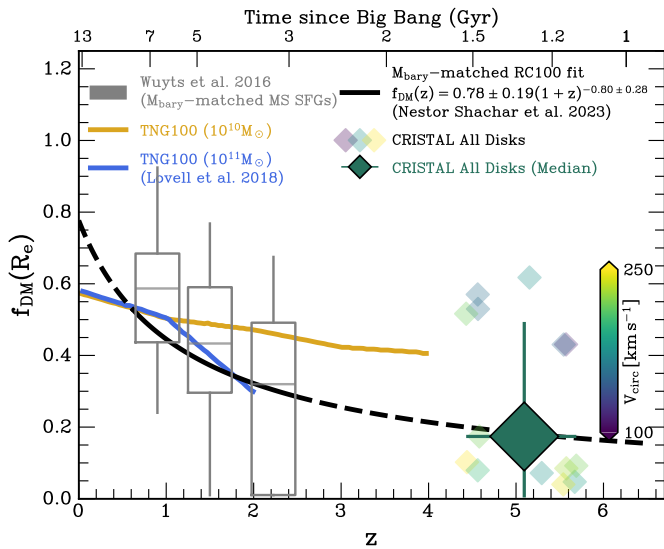


Fig. 13: The dark matter (DM) fraction at effective radius ( $f_{\text{DM}}(R_e)$ ) as a function of redshift. The  $f_{\text{DM}}(R_e)$  of individual CRISTAL disks ( $4 < z < 6$ ) are represented by small diamonds, colour-coded by their  $V_{\text{circ}}(R_e)$ . For comparison, we include lower redshift studies around  $z = 2$  from Wuyts et al. (2016) (grey box-and-whisker) and the best-fit relation to the RC100 data set (Nestor Shachar et al. 2023) (black solid line for the redshift range covered and dashed line for the extrapolated range). For both observational studies, we consider only star-forming galaxies on the main sequence (MS SFGs) and the baryonic mass  $M_{\text{bary}}$  matched within 0.3 dex of the CRISTAL disks. The new best-fit relation to RC100, using the  $M_{\text{bary}}$ -matched sample, is shown in the legend. The trends predicted from the TNG100 simulation for  $M_* = 10^{10} M_{\odot}$  and  $M_* = 10^{11} M_{\odot}$  are shown in yellow and blue, respectively (Lovell et al. 2018). Overall, the CRISTAL disks tend to be baryon-dominated on galactic scales, with a median DM fraction of  $\sim 18\%$  (large green diamond) that is tentatively consistent with the extrapolated relation based on RC100. However, there is a significant scatter in the values among the sample, partly driven by the scattered distributions of circular velocity  $V_{\text{circ}}(R_e)$  (and  $\Sigma_{\text{bary}}$ ) shown in Figure 12.

tral regions in gas-rich systems (e.g. El-Zant et al. 2001), and/or strong feedback processes redistributing DM to larger radii (e.g. Freundlich et al. 2020). One example is CRISTAL-02, which has  $f_{\text{DM}}(R_e) < 0.1$  and drives a vigorous outflow detected in [C II] (Davies et al. 2025).

The widely scattered distribution in Fig. 13 with large errors associated with individual galaxies prevents a definite conclusion on the physical origin of this distribution. We investigated whether the inhomogeneous radial coverage of the RCs (Fig. 7) could systematically drive up the  $f_{\text{DM}}(R_e)$  for galaxies with limited radial coverage. However, we do not find a straightforward one-to-one correspondence between  $f_{\text{DM}}(R_e)$  and the ratio of  $R_{\text{out}}/R_e$  (Kendall's  $\tau = -0.19^{+0.23}_{-0.25}$ ,  $p = 0.32^{+0.23}_{-0.25}$ ).

We emphasise that  $f_{\text{DM}}$  is measured at the effective radius, and we lack constraints of the DM distribution on the halo scale ( $\gg R_e$ ) with our current data, except for the very compact CRISTAL-23c. Extrapolating the DM mass from the inner disk to the virial scale with an NFW distribution will result in an unphysically large baryon fraction larger than the cosmic baryon fraction (Genzel et al. 2017). As discussed in § 5.1, the intrinsic, circular velocities would also depend on the assumption of

the pressure support corrections, which would explain the differences found in the literature (cf. Sharma et al. (2021) with, e.g. Genzel et al. (2020); Price et al. (2021) and Nestor Shachar et al. (2023)). If we were to assume a non-constant  $\sigma$ , such as an exponential decline, for the pressure support correction, rather than using Eq. (1), the correction to  $V_{\text{rot}}$  would be even larger (Eq. (12) in Price et al. 2022), leading to a more steeply declining  $V_{\text{circ}}$ , which would further exacerbate the discrepancies between our observations and simulations.

Although we have adopted the NFW profile for the DM profile, the  $f_{\text{DM}}(< R_e)$  results for the sample change less than 10% (in terms of absolute difference) for alternative DM mass profile assumption, such as the two-power halo (2PH) profile (Binney & Tremaine 2008) with a variable inner slope. Improved constraints on the DM fraction in the future would benefit from deeper observations of individual galaxies and/or kinematic stacking analysis (e.g. Lang et al. 2017; Tiley et al. 2019).

## 8. Nature of Non-Disks

The origin of the kinematic perturbations in the Non-Disk subset of the sample could arise from galaxy interactions and mergers. Most Non-Disks, except CRISTAL-21, 24 and 25, have visible companions already in the *HST* and/or *JWST* images alone, and the one classified as Non-Disk is, in most cases, the less luminous and less massive for those with available mass measurement. The higher non-disk fraction among the CRISTAL kinematic sample compared to samples of typical MS SFGs at lower redshift may not be surprising in view of the increase in merger rates with redshift from both observational work (Duncan et al. 2019; Romano et al. 2021; Duan et al. 2025; Puskás et al. 2025; Shibuya et al. 2025) and numerical simulations (Rodríguez-Gomez et al. 2015; Pillepich et al. 2019; O’Leary et al. 2021). It will be interesting in future work to investigate in more detail the environment of the galaxies to quantify, for instance, interaction strengths from neighbouring systems. More complete redshift identification around the CRISTAL galaxies will be necessary for that purpose.

## 9. Summary and Outlook

We presented the kinematics study of a sample of MS SFGs at redshift  $4 < z < 6$  from the ALMA-CRISTAL program. The angular resolution of the sensitive [C II] ALMA observations enables us to characterise the kinematics of galaxies at a scale of  $\sim 1$  kpc. We classified the galaxies primarily based on their kinematic features traced by [C II] using a variety of methods that have been applied in lower-redshift studies, supplemented by morphological information from *HST* and *JWST* imaging (§ 3). We find that  $50 \pm 9\%$  of the galaxies in our sample are disk-dominated (§ 4), with over half of them located in systems of multiple components, which differs from the more isolated environment of lower-redshift disks. We fitted the kinematics of the disks using fully forward-modelled 3D kinematic models (§ 5). Our kinematics modelling reveals the following important properties of the CRISTAL main sequence disks:

1. They have a high contribution of turbulence relative to rotational support, with a median disk velocity dispersion of  $\sim 70 \text{ km s}^{-1}$  and  $V_{\text{rot}}(R_e)/\sigma_0$  of  $\sim 2$  (§ 6.1).
2. Their high-velocity dispersions are consistent with the predicted evolution based on Toomre theory and the extrapolated evolutionary trends based on detailed studies of cosmic noon to lower-redshift galaxies (§ 6.1).

3. Their tentative correlation between gas mass and velocity dispersion provides hints that the high dispersion is sustained by gravitational instability, but it is unclear whether this is a local or global phenomenon (§ 6.2).
4. They tend to have a low dark matter fraction, with median  $f_{\text{DM}}(< R_e) \approx 18\%$ , although spanning a significant range from  $\sim 5\%$  to  $\sim 60\%$ ; the median value is in broad agreement with the extrapolated trend based on studies of lower redshifts, albeit with large scatter (§ 7).

The deep, high resolution ALMA observations of [CII]158 $\mu\text{m}$  line emission from the CRISTAL program enabled a first systematic census of the kinematics of typical MS star-forming galaxies at  $z \sim 4\text{--}6$ . The brightness of [CII] along with its sensitivity to the multi-phase ISM makes it an ideal probe of the gas motions (among other properties) over a large extent of galaxies encompassing cold molecular gas, ionised, and photodissociation regions, facilitating measurements reaching the outskirts of galaxies. As observations of rest-optical line emission originating from the warm ionised gas phase become available from *JWST* IFU follow-up of CRISTAL targets, direct comparisons will become possible. This will be important especially with regard to the issue of gas turbulence, which, as discussed in this work (§ 6) and in the literature (e.g. Girard et al. 2021; Wisnioski et al. 2025; Ejdetj  rn et al. 2022; Kohandel et al. 2024), would greatly benefit from measurements in multiple tracers for the same objects. Another outlook enabled by CRISTAL-ALMA and *JWST*-IFU synergies is the connection between spatial variations in gas-phase metallicity and kinematics, which will be the subject of a forthcoming study.

**Acknowledgements.** We thank the anonymous referee for the constructive feedback which improves the clarity of the work. L.L.L. is thankful for the stimulating discussions with M. Bureau, Q. Fei, S. Pastras, W. Maciejewski and E. Wisnioski at the various stages of this work. L.L.L. thanks A. Nestor for providing the data tables for Fig. 12. N.M.F.S. and J.C. acknowledge financial support from the European Research Council (ERC) Advanced Grant under the European Union’s (EU’s) Horizon Europe research and innovation programme (grant agreement AdG GALPHYS, No. 101055023). H.  . acknowledges funding by the EU (ERC APEX, 101164796). Views and opinions expressed are, however, those of the author(s) only and do not necessarily reflect those of the EU or the ERC. Neither the EU nor the granting authority can be held responsible for them. R.H.-C. thanks the Max Planck Society for support under the Partner Group project ‘The Baryon Cycle in Galaxies’ between the Max Planck for Extraterrestrial Physics and the Universidad de Concepci  n. M.A. and R.H.-C. also gratefully acknowledge financial support from ANID - MILENIO - NCN2024\_112. M.A., R.J.A., R.H.-C., M.S. and K. Telikova acknowledge support from ANID BASAL FB210003. R.J.A. was supported by FONDECYT grant number 1231718. R.B. acknowledges support from an STFC Ernest Rutherford Fellowship [grant number ST/T003596/1]. R.L.D. is supported by the Australian Research Council through the Discovery Early Career Researcher Award (DECRA) Fellowship DE240100136 funded by the Australian Government. T.D.-S. acknowledges the research project was supported by the Hellenic Foundation for Research and Innovation (HFRI) under the ‘2nd Call for HFRI Research Projects to support Faculty Members & Researchers’ (Project Number: 03382). I.D.L. acknowledges funding from the ERC under the EU’s Horizon 2020 research and innovation program DustOrigin (ERC-2019-StG-851622) and from the Flemish Fund for Scientific Research (FWO-Vlaanderen) through the research project G0A1523N. R.I. is supported by Grants-in-Aid for Japan Society for the Promotion of Science (JSPS) Fellows (KAKENHI Grant Number 23KJ1006). T.N. acknowledges the support of the Deutsche Forschungsgemeinschaft (DFG, German Research Foundation) under Germany’s Excellence Strategy - EXC-2094 - 390783311 of the DFG Cluster of Excellence ‘ORIGINS’. M.S. was financially supported by Becas-ANID scholarship #21221511. K. Tadaki acknowledges support from JSPS KAKENHI Grant No. 23K03466. K. Telikova was supported by ALMA ANID grant number 31220026. V.V. acknowledges support from the ALMA-ANID Postdoctoral Fellowship under the award ASTRO21-0062. This paper makes use of the following ALMA data: ADS/JAO.ALMA#2021.1.00280.L, 2017.1.00428.L, 2012.1.00523.S, 2018.1.01359.S, 2019.1.01075.S. ALMA is a partnership of ESO (representing its member states), NSF (USA) and NINS (Japan), together

with NRC (Canada), NSC and ASIAA (Taiwan), and KASI (Republic of Korea), in cooperation with the Republic of Chile. The Joint ALMA Observatory is operated by ESO, AUI/NRAO and NAOJ. This work is based in part on observations made with the NASA/ESA/CSA James Webb Space Telescope and NASA/ESA Hubble Space Telescope. The data were obtained from the Mikulski Archive for Space Telescopes (MAST) at the Space Telescope Science Institute, which is operated by the Association of Universities for Research in Astronomy, Inc., under NASA contract NAS 5-03127 for *JWST* and NAS 5-26555 for HST. The specific observations analysed can be accessed via [10.17909/2gpc-2d24](https://doi.org/10.17909/2gpc-2d24). Support to MAST for these data is provided by the NASA Office of Space Science via grant NAG5-7584 and by other grants and contracts. Some of the data products presented herein were retrieved from the Dawn *JWST* Archive (DJA). DJA is an initiative of the Cosmic Dawn Center (DAWN), which is funded by the Danish National Research Foundation under grant DNRF140. This work made use of the following Python packages: Astropy (Astropy Collaboration et al. 2022), corner (Foreman-Mackey 2016), DysmalPy (Davies et al. 2004b,a, 2011; Cresci et al. 2009; Wuyts et al. 2016; Lang et al. 2017; Price et al. 2021; Lee et al. 2025), emcee (Foreman-Mackey et al. 2013), Imfit (Erwin 2015), Matplotlib (Hunter 2007), Numpy (Harris et al. 2020), pymccorrelation (Curran 2014; Privon et al. 2020), TrilogY (Coe et al. 2012), and Scipy (Virtanen et al. 2020).

## References

- Amvrosiadis, A., Lange, S., Nightingale, J. W., et al. 2025, *MNRAS*, **537**, 1163
- Astropy Collaboration, Price-Whelan, A. M., Lim, P. L., et al. 2022, *ApJ*, **935**, 167
- Bari  i  , I., Jones, T., Mortensen, K., et al. 2025, *ApJ*, **983**, 139
- Beckers, J. M. 1982, *Optica Acta*, **29**, 361
- Behrendt, M., Burkert, A., & Schartmann, M. 2015, *MNRAS*, **448**, 1007
- B  thermin, M., Accard, C., Guillaume, C., et al. 2023, *A&A*, **680**, L8
- B  thermin, M., Daddi, E., Magdis, G., et al. 2015, *A&A*, **573**, A113
- B  thermin, M., Fudamoto, Y., Ginolfi, M., et al. 2020, *A&A*, **643**, A2
- B  thermin, M., Wu, H.-Y., Lagache, G., et al. 2017, *A&A*, **607**, A89
- Binney, J. & Tremaine, S. 2008, *Galactic Dynamics: Second Edition* (Princeton University Press)
- Birkin, J. E., Puglisi, A., Swinbank, A. M., et al. 2024, *MNRAS*, **531**, 61
- Birkin, J. E., Spilker, J. S., Herrera-Camus, R., et al. 2025, *ApJ*, **985**, 243
- Bland-Hawthorn, J. & Gerhard, O. 2016, *ARA&A*, **54**, 529
- Blumenthal, G. R., Faber, S. M., Flores, R., & Primack, J. R. 1986, *ApJ*, **301**, 27
- Bouch  , N. F., Bera, S., Krajnovi  , D., et al. 2022, *A&A*, **658**, A76
- Bouwens, R. J., Smit, R., Schouws, S., et al. 2022, *ApJ*, **931**, 160
- Bovy, J. & Rix, H.-W. 2013, *ApJ*, **779**, 115
- Burkert, A., Genzel, R., Bouch  , N., et al. 2010, *ApJ*, **725**, 2324
- CASA Team, Bean, B., Bhatnagar, S., et al. 2022, *PASP*, **134**, 114501
- Cathey, J., Gonzalez, A. H., Lower, S., et al. 2024, *ApJ*, **967**, 11
- Christy, J. W., Wellnitz, D. D., & Currie, D. G. 1981, *Lowell Observatory Bulletin*, **9**, 28
- Clark, P. C., Glover, S. C. O., Ragan, S. E., & Duarte-Cabral, A. 2019, *MNRAS*, **486**, 4622
- Coe, D., Umetsu, K., Zitrin, A., et al. 2012, *ApJ*, **757**, 22
- Cole, J. W., Papovich, C., Finkelstein, S. L., et al. 2025, *ApJ*, **979**, 193
- Condon, J. J., Cotton, W. D., Greisen, E. W., et al. 1998, *AJ*, **115**, 1693
- Cormier, D., Abel, N. P., Hony, S., et al. 2019, *A&A*, **626**, A23
- Costantin, L., Gillman, S., Boogaard, L. A., et al. 2025, *A&A*, in press
- Courteau, S. 1997, *AJ*, **114**, 2402
- Courteau, S. & Dutton, A. A. 2015, *ApJ*, **801**, L20
- Cresci, G., Hicks, E. K. S., Genzel, R., et al. 2009, *ApJ*, **697**, 115
- Curran, P. A. 2014, *arXiv e-prints*, [arXiv:1411.3816](https://arxiv.org/abs/1411.3816)
- Dalcanton, J. J. & Stilp, A. M. 2010, *ApJ*, **721**, 547
- Danhaive, A. L., Tacchella, S.,   bler, H., et al. 2025, *arXiv e-prints*, [arXiv:2503.21863](https://arxiv.org/abs/2503.21863)
- Davies, R., F  rster Schreiber, N. M., Cresci, G., et al. 2011, *ApJ*, **741**, 69
- Davies, R. I., Tacconi, L. J., & Genzel, R. 2004a, *ApJ*, **613**, 781
- Davies, R. I., Tacconi, L. J., & Genzel, R. 2004b, *ApJ*, **602**, 148
- Davies, R. L., Fisher, D. B., Herrera-Camus, R., et al. 2025, *Nature Astronomy*, submitted
- Davis, T. A., Alatalo, K., Bureau, M., et al. 2013, *MNRAS*, **429**, 534
- Davis, T. A., Bureau, M., Onishi, K., et al. 2017, *MNRAS*, **468**, 4675
- de Blok, W. J. G., Healy, J., Maccagni, F. M., et al. 2024, *A&A*, **688**, A109
- de Graaff, A., Rix, H.-W., Carniani, M., et al. 2024, *A&A*, **684**, A87
- Dekel, A., Birnboim, Y., Engel, G., et al. 2009, *Nature*, **457**, 451
- Dekel, A. & Burkert, A. 2014, *MNRAS*, **438**, 1870
- Dekel, A., Ginzburg, O., Jiang, F., et al. 2020, *MNRAS*, **493**, 4126
- Dessauges-Zavadsky, M., Ginolfi, M., Pozzi, F., et al. 2020, *A&A*, **643**, A5
- Devereaux, T., Cassata, P., Ibar, E., et al. 2024, *A&A*, **686**, A156
- Di Teodoro, E. M. & Fraternali, F. 2015, *MNRAS*, **451**, 3021
- Di Teodoro, E. M., Fraternali, F., & Miller, S. H. 2016, *A&A*, **594**, A77



- Duan, Q., Conselice, C. J., Li, Q., et al. 2025, *MNRAS*, **staf638**
- Duncan, K., Conselice, C. J., Mundy, C., et al. 2019, *ApJ*, **876**, 110
- Dutton, A. A. & Macciò, A. V. 2014, *MNRAS*, **441**, 3359
- Eisenhauer, F., Tecza, M., Thatte, N., et al. 2003, *The Messenger*, **113**, 17
- Ejdetjärn, T., Agertz, O., Östlin, G., Renaud, F., & Romeo, A. B. 2022, *MNRAS*, **514**, 480
- El-Zant, A., Shlosman, I., & Hoffman, Y. 2001, *ApJ*, **560**, 636
- Elmegreen, B. G., Martínez, Z., & Hunter, D. A. 2022, *ApJ*, **928**, 143
- Epinat, B., Amram, P., & Marcelin, M. 2008, *MNRAS*, **390**, 466
- Epinat, B., Contini, T., Le Fèvre, O., et al. 2009, *A&A*, **504**, 789
- Erwin, P. 2015, *ApJ*, **799**, 226
- Faisst, A. L., Fudamoto, Y., Oesch, P. A., et al. 2020a, *MNRAS*, **498**, 4192
- Faisst, A. L., Schaerer, D., Lemaux, B. C., et al. 2020b, *ApJS*, **247**, 61
- Fei, Q., Silverman, J. D., Fujimoto, S., et al. 2025, *ApJ*, **980**, 84
- Ferreira, L., Conselice, C. J., Sazonova, E., et al. 2023, *ApJ*, **955**, 94
- Foreman-Mackey, D. 2016, *The Journal of Open Source Software*, **1**, 24
- Foreman-Mackey, D., Hogg, D. W., Lang, D., & Goodman, J. 2013, *PASP*, **125**, 306
- Förster Schreiber, N. M., Genzel, R., Bouché, N., et al. 2009, *ApJ*, **706**, 1364
- Förster Schreiber, N. M., Renzini, A., Mancini, C., et al. 2018, *ApJS*, **238**, 21
- Förster Schreiber, N. M. & Wuyts, S. 2020, *ARA&A*, **58**, 661
- Fraternali, F., Karim, A., Magnelli, B., et al. 2021, *A&A*, **647**, A194
- Freundlich, J., Dekel, A., Jiang, F., et al. 2020, *MNRAS*, **491**, 4523
- Fujimoto, S., Oguri, M., Brammer, G., et al. 2021, *ApJ*, **911**, 99
- Fujimoto, S., Ouchi, M., Kohno, K., et al. 2024, *arXiv e-prints*, [arXiv:2402.18543](https://arxiv.org/abs/2402.18543)
- Gatto, A., Walch, S., Low, M. M. M., et al. 2015, *MNRAS*, **449**, 1057
- Genzel, R., Burkert, A., Bouché, N., et al. 2008, *ApJ*, **687**, 59
- Genzel, R., Förster Schreiber, N. M., Lang, P., et al. 2014, *ApJ*, **785**, 75
- Genzel, R., Förster Schreiber, N. M., Übler, H., et al. 2017, *Nature*, **543**, 397
- Genzel, R., Jolly, J. B., Liu, D., et al. 2023, *ApJ*, **957**, 48
- Genzel, R., Newman, S., Jones, T., et al. 2011, *ApJ*, **733**, 101
- Genzel, R., Price, S. H., Übler, H., et al. 2020, *ApJ*, **902**, 98
- Genzel, R., Tacconi, L. J., Kurk, J., et al. 2013, *ApJ*, **773**, 68
- Genzel, R., Tacconi, L. J., Lutz, D., et al. 2015, *ApJ*, **800**, 20
- Ginzburg, O., Dekel, A., Mandelker, N., & Krumholz, M. R. 2022, *MNRAS*, **513**, 6177
- Girard, M., Dessauges-Zavadsky, M., Combes, F., et al. 2019, *A&A*, **631**, A91
- Girard, M., Dessauges-Zavadsky, M., Schaerer, D., et al. 2018, *A&A*, **613**, A72
- Girard, M., Fisher, D. B., Bolatto, A. D., et al. 2021, *ApJ*, **909**, 12
- Glazebrook, K. 2013, *PASA*, **30**, e056
- Gnerucci, A., Marconi, A., Capetti, A., Axon, D. J., & Robinson, A. 2010, *A&A*, **511**, A19
- Gnerucci, A., Marconi, A., Cresci, G., et al. 2011, *A&A*, **528**, A88
- Harris, C. R., Millman, K. J., van der Walt, S. J., et al. 2020, *Nature*, **585**, 357
- Hayward, C. C. & Hopkins, P. F. 2017, *MNRAS*, **465**, 1682
- Hayward, C. C., Sparre, M., Chapman, S. C., et al. 2021, *MNRAS*, **502**, 2922
- Herrera-Camus, R., Förster Schreiber, N. M., Price, S. H., et al. 2022, *A&A*, **665**, L8
- Herrera-Camus, R., González-López, J., Förster Schreiber, N., et al. 2025, *A&A*, **699**, A80
- Hirstenstone, J., Jones, T., Wang, X., et al. 2019, *ApJ*, **880**, 54
- Hodge, J. A., Carilli, C. L., Walter, F., et al. 2012, *ApJ*, **760**, 11
- Hogan, L., Rigopoulou, D., Magdis, G. E., et al. 2021, *MNRAS*, **503**, 5329
- Huang, S., Kawabe, R., Kohno, K., et al. 2023, *ApJ*, **958**, L26
- Huertas-Company, M., Iyer, K. G., Angeloudi, E., et al. 2024, *A&A*, **685**, A48
- Huertas-Company, M., Shuntov, M., Dong, Y., et al. 2025, *arXiv e-prints*, [arXiv:2502.03532](https://arxiv.org/abs/2502.03532)
- Hunter, J. D. 2007, *Computing in Science and Engineering*, **9**, 90
- Ikeda, R., Tadaki, K.-i., Mitsuhashi, I., et al. 2025, *A&A*, **693**, A237
- Jacobs, C., Glazebrook, K., Calabrò, A., et al. 2023, *ApJ*, **948**, L13
- Jiménez, E., Lagos, C. d. P., Ludlow, A. D., & Wisnioski, E. 2023, *MNRAS*, **524**, 4346
- Johnson, H. L., Harrison, C. M., Swinbank, A. M., et al. 2018, *MNRAS*, **474**, 5076
- Jones, G. C., Béthermin, M., Fudamoto, Y., et al. 2020, *MNRAS*, **491**, L18
- Jones, G. C., Vergani, D., Romano, M., et al. 2021, *MNRAS*, **507**, 3540
- Jones, T. A., Swinbank, A. M., Ellis, R. S., Richard, J., & Stark, D. P. 2010, *MNRAS*, **404**, 1247
- Jorsater, S. & van Moorsel, G. A. 1995, *AJ*, **110**, 2037
- Kaasinen, M., Scoville, N., Walter, F., et al. 2019, *ApJ*, **880**, 15
- Kaasinen, M., Walter, F., Novak, M., et al. 2020, *ApJ*, **899**, 37
- Kartaltepe, J. S., Rose, C., Vanderhoof, B. N., et al. 2023, *ApJ*, **946**, L15
- Kassin, S. A., Weiner, B. J., Faber, S. M., et al. 2012, *ApJ*, **758**, 106
- Kim, C.-G. & Ostriker, E. C. 2018, *ApJ*, **853**, 173
- Kohandel, M., Pallottini, A., Ferrara, A., et al. 2024, *A&A*, **685**, A72
- Koprowski, M. P., Wijesekera, J. V., Dunlop, J. S., et al. 2024, *A&A*, **691**, A164
- Krajnović, D., Cappellari, M., de Zeeuw, P. T., & Copin, Y. 2006, *MNRAS*, **366**, 787
- Kretschmer, M., Dekel, A., Freundlich, J., et al. 2021, *MNRAS*, **503**, 5238
- Krumholz, M. R., Burkert, B., Forbes, J. C., & Crocker, R. M. 2018, *MNRAS*, **477**, 2716
- Lambert, T. S., Posses, A., Aravena, M., et al. 2023, *MNRAS*, **518**, 3183
- Lang, P., Förster Schreiber, N. M., Genzel, R., et al. 2017, *ApJ*, **840**, 92
- Law, D. R., Steidel, C. C., Erb, D. K., et al. 2009, *ApJ*, **697**, 2057
- Le Fèvre, O., Béthermin, M., Faisst, A., et al. 2020, *A&A*, **643**, A1
- Lee, J. H., Park, C., Hwang, H. S., & Kwon, M. 2024, *ApJ*, **966**, 113
- Lee, L. L., Förster Schreiber, N. M., Price, S. H., et al. 2025, *ApJ*, **978**, 14
- Leethochawalit, N., Jones, T. A., Ellis, R. S., et al. 2016, *ApJ*, **820**, 84
- Li, J., Da Cunha, E., González-López, J., et al. 2024, *ApJ*, **976**, 70
- Lelli, F., Di Teodoro, E. M., Fraternali, F., et al. 2021, *Science*, **371**, 713
- Lemaux, B. C., Le Fèvre, O., Cucciati, O., et al. 2018, *A&A*, **615**, A77
- Leroy, A. K., Bolatto, A., Gordon, K., et al. 2011, *ApJ*, **737**, 12
- Li, J., Da Cunha, E., González-López, J., et al. 2024, *ApJ*, **976**, 70
- Lines, N. E. P., Bowler, R. A. A., Adams, N. J., et al. 2025, *MNRAS*, **staf627**
- Liu, D., Förster Schreiber, N. M., Genzel, R., et al. 2023, *ApJ*, **942**, 98
- Liu, D., Förster Schreiber, N. M., Harrington, K. C., et al. 2024a, *Nature Astronomy*
- Liu, Z., Kodama, T., Morishita, T., et al. 2025, *ApJ*, **980**, 69
- Liu, Z., Silverman, J. D., Daddi, E., et al. 2024b, *ApJ*, **968**, 15
- Livemore, R. C., Jones, T. A., Richard, J., et al. 2015, *MNRAS*, **450**, 1812
- Lovell, M. R., Pillepich, A., Genel, S., et al. 2018, *MNRAS*, **481**, 1950
- Madau, P. & Dickinson, M. 2014, *ARA&A*, **52**, 415
- Martinsson, T. P. K., Verheijen, M. A. W., Westfall, K. B., et al. 2013a, *A&A*, **557**, A131
- Martinsson, T. P. K., Verheijen, M. A. W., Westfall, K. B., et al. 2013b, *A&A*, **557**, A130
- Mason, C. A., Treu, T., Fontana, A., et al. 2017, *ApJ*, **838**, 14
- Miller, T. B., Suess, K. A., Setton, D. J., et al. 2024, *arXiv e-prints*, [arXiv:2412.06957](https://arxiv.org/abs/2412.06957)
- Mitsuhashi, I., Tadaki, K.-i., Ikeda, R., et al. 2024, *A&A*, **690**, A197
- Mizener, A., Pope, A., McKinney, J., et al. 2024, *ApJ*, **970**, 30
- Mogotsi, K. M., de Blok, W. J. G., Caldu-Primo, A., et al. 2016, *AJ*, **151**, 15
- Moster, B. P., Naab, T., & White, S. D. M. 2018, *MNRAS*, **477**, 1822
- Nakajima, K., Ouchi, M., Isobe, Y., et al. 2023, *ApJS*, **269**, 33
- Navarro, J. F., Frenk, C. S., & White, S. D. M. 1996, *ApJ*, **462**, 563
- Neeleman, M., Novak, M., Venemans, B. P., et al. 2021, *ApJ*, **911**, 141
- Neeleman, M., Prochaska, J. X., Kanekar, N., & Rafelski, M. 2020, *Nature*, **581**, 269
- Neeleman, M., Walter, F., Decarli, R., et al. 2023, *ApJ*, **958**, 132
- Nestor Shachar, A., Price, S. H., Förster Schreiber, N. M., et al. 2023, *ApJ*, **944**, 78
- Noordermeer, E. 2008, *MNRAS*, **385**, 1359
- O'Leary, J. A., Moster, B. P., Naab, T., & Somerville, R. S. 2021, *MNRAS*, **501**, 3215
- Orr, M. E., Hayward, C. C., Medling, A. M., et al. 2020, *MNRAS*, **496**, 1620
- Pandya, V., Zhang, H., Huertas-Company, M., et al. 2024, *ApJ*, **963**, 54
- Parlanti, E., Carniani, S., Pallottini, A., et al. 2023, *A&A*, **673**, A153
- Parlanti, E., Carniani, S., Übler, H., et al. 2024, *A&A*, **684**, A24
- Parlanti, E., Carniani, S., Venturi, G., et al. 2025, *A&A*, **695**, A6
- Patrício, V., Richard, J., Carton, D., et al. 2018, *MNRAS*, **477**, 18
- Pavesi, R., Riechers, D. A., Faisst, A. L., Stacey, G. J., & Capak, P. L. 2019, *ApJ*, **882**, 168
- Perna, M., Arribas, S., Ji, X., et al. 2025, *A&A*, **694**, A170
- Peschken, N., Lokas, E. L., & Athanassoula, E. 2020, *MNRAS*, **493**, 1375
- Pillepich, A., Nelson, D., Springel, V., et al. 2019, *MNRAS*, **490**, 3196
- Planck Collaboration, Abergel, A., Ade, P. A. R., et al. 2011, *A&A*, **536**, A21
- Pope, A., McKinney, J., Kamienieski, P., et al. 2023, *ApJ*, **951**, L46
- Posses, A., Aravena, M., González-López, J., et al. 2025, *A&A*, **in press**
- Posses, A. C., Aravena, M., González-López, J., et al. 2023, *A&A*, **669**, A46
- Price, S. H., Kriek, M., Barro, G., et al. 2020, *ApJ*, **894**, 91
- Price, S. H., Shimizu, T. T., Genzel, R., et al. 2021, *ApJ*, **922**, 143
- Price, S. H., Übler, H., Förster Schreiber, N. M., et al. 2022, *A&A*, **665**, A159
- Privon, G. C., Ricci, C., Aalto, S., et al. 2020, *ApJ*, **893**, 149
- Puglisi, A., Dudzevičiūtė, U., Swinbank, M., et al. 2023, *MNRAS*, **524**, 2814
- Puskás, D., Tacchella, S., Simmonds, C., et al. 2025, *arXiv e-prints*, [arXiv:2502.01721](https://arxiv.org/abs/2502.01721)
- Rathjen, T.-E., Naab, T., Walch, S., et al. 2023, *MNRAS*, **522**, 1843
- Rhodes, S., Jones, T., Keerthi Vasan G., C., et al. 2025, *arXiv e-prints*, [arXiv:2503.22039](https://arxiv.org/abs/2503.22039)
- Riechers, D. A., Carilli, C. L., Capak, P. L., et al. 2014, *ApJ*, **796**, 84
- Rizzo, F., Roman-Oliveira, F., Fraternali, F., et al. 2023, *A&A*, **679**, A129
- Rizzo, F., Vegetti, S., Fraternali, F., Stacey, H. R., & Powell, D. 2021, *MNRAS*, **507**, 3952
- Rizzo, F., Vegetti, S., Powell, D., et al. 2020, *Nature*, **584**, 201
- Robertson, B., Bullock, J. S., Cox, T. J., et al. 2006, *ApJ*, **645**, 986
- Rodríguez-Gomez, V., Genel, S., Vogelsberger, M., et al. 2015, *MNRAS*, **449**, 49
- Roman-Oliveira, F., Fraternali, F., & Rizzo, F. 2023, *MNRAS*, **521**, 1045
- Romano, M., Cassata, P., Morselli, L., et al. 2021, *A&A*, **653**, A111



- Rowland, L. E., Hodge, J., Bouwens, R., et al. 2024, *MNRAS*, **535**, 2068
- Scoville, N., Lee, N., Vanden Bout, P., et al. 2017, *ApJ*, **837**, 150
- Scoville, N., Sheth, K., Aussel, H., et al. 2016, *ApJ*, **820**, 83
- Sedov, L. I. 1946, *Journal of Applied Mathematics and Mechanics*, **10**, 241
- Sedov, L. I. 1959, *Similarity and Dimensional Methods in Mechanics*
- Sérsic, J. L. 1968, *Atlas de Galaxias Australes* (Observatorio Astronomico, Universidad Nacional de Cordoba)
- Shao, Y., Wang, R., Weiss, A., et al. 2022, *A&A*, **668**, A121
- Shapiro, K. L., Genzel, R., Förster Schreiber, N. M., et al. 2008, *ApJ*, **682**, 231
- Sharda, P., da Cunha, E., Federrath, C., et al. 2019, *MNRAS*, **487**, 4305
- Sharma, G., Salucci, P., Harrison, C. M., van de Ven, G., & Lapi, A. 2021, *MNRAS*, **503**, 1753
- Sharples, R., Bender, R., Agudo Berbel, A., et al. 2013, *The Messenger*, **151**, 21
- Shetty, R. & Ostriker, E. C. 2012, *ApJ*, **754**, 2
- Shibuya, T., Ito, Y., Asai, K., et al. 2025, *PASJ*, **77**, 21
- Smit, R., Bouwens, R. J., Carniani, S., et al. 2018, *Nature*, **553**, 178
- Solimano, M., González-López, J., Aravena, M., et al. 2025, *A&A*, **693**, A70
- Sommovigo, L., Ferrara, A., Carniani, S., et al. 2022, *MNRAS*, **517**, 5930
- Sotillo-Ramos, D., Pillepich, A., Donnari, M., et al. 2022, *MNRAS*, **516**, 5404
- Speagle, J. S., Steinhardt, C. L., Capak, P. L., & Silverman, J. D. 2014, *ApJS*, **214**, 15
- Springel, V. & Hernquist, L. 2005, *ApJ*, **622**, L9
- Stach, S. M., Smail, I., Swinbank, A. M., et al. 2018, *ApJ*, **860**, 161
- Stark, D. P., Swinbank, A. M., Ellis, R. S., et al. 2008, *Nature*, **455**, 775
- Stefanon, M., Yan, H., Mobasher, B., et al. 2017, *ApJS*, **229**, 32
- Swinbank, A. M., Papadopoulos, P. P., Cox, P., et al. 2011, *ApJ*, **742**, 11
- Swinbank, A. M., Smail, I., Sobral, D., et al. 2012, *ApJ*, **760**, 130
- Tacconi, L. J., Genzel, R., Neri, R., et al. 2010, *Nature*, **463**, 781
- Tacconi, L. J., Genzel, R., Saintonge, A., et al. 2018, *ApJ*, **853**, 179
- Tacconi, L. J., Genzel, R., & Sternberg, A. 2020, *Annual Review of Astronomy and Astrophysics*, **58**, 157
- Tadano, K., Iono, D., Yun, M. S., et al. 2018, *Nature*, **560**, 613
- Tanaka, T. S., Silverman, J. D., Nakazato, Y., et al. 2024, *PASJ*, **76**, 1323
- Taylor, G. 1950, *Proceedings of the Royal Society of London Series A*, **201**, 159
- Telikova, K., González-López, J., Aravena, M., et al. 2025, *A&A*, **669**, A5
- Tiley, A. L., Swinbank, A. M., Harrison, C. M., et al. 2019, *MNRAS*, **485**, 934
- Tohill, C., Bamford, S. P., Conselice, C. J., et al. 2024, *ApJ*, **962**, 164
- Toomre, A. 1964, *ApJ*, **139**, 1217
- Tsukui, T. & Iguchi, S. 2021, *Science*, **372**, 1201
- Turner, O. J., Cirasuolo, M., Harrison, C. M., et al. 2017, *MNRAS*, **471**, 1280
- Übler, H., D'Eugenio, F., Perna, M., et al. 2024, *MNRAS*, **533**, 4287
- Übler, H., Genel, S., Sternberg, A., et al. 2021, *MNRAS*, **500**, 4597
- Übler, H., Genzel, R., Tacconi, L. J., et al. 2018, *ApJ*, **854**, L24
- Übler, H., Genzel, R., Wisnioski, E., et al. 2019, *ApJ*, **880**, 48
- Übler, H., Naab, T., Oser, L., et al. 2014, *MNRAS*, **443**, 2092
- Umehata, H., Steidel, C. C., Smail, I., et al. 2025, *PASJ*, **77**, 432
- Vallini, L., Gallerani, S., Ferrara, A., Pallottini, A., & Yue, B. 2015, *ApJ*, **813**, 36
- van Albada, T. S., Bahcall, J. N., Begeman, K., & Sancisi, R. 1985, *ApJ*, **295**, 305
- van der Kruit, P. C. & Allen, R. J. 1978, *ARA&A*, **16**, 103
- van der Wel, A., Franx, M., van Dokkum, P. G., et al. 2014, *ApJ*, **788**, 28
- Varadaraj, R. G., Bowler, R. A. A., Jarvis, M. J., et al. 2024, *MNRAS*, **533**, 3724
- Venkateswaran, A., Weiss, A., Sulzenauer, N., et al. 2024, *ApJ*, **977**, 161
- Villanueva, V., Herrera-Camus, R., González-López, J., et al. 2024, *A&A*, **691**, A133
- Virtanen, P., Gommers, R., Oliphant, T. E., et al. 2020, *Nature Methods*, **17**, 261
- Wang, W., Cantalupo, S., Pensabene, A., et al. 2025, *Nature Astronomy*
- Wisnioski, E., Förster Schreiber, N. M., Fossati, M., et al. 2019, *ApJ*, **886**, 124
- Wisnioski, E., Förster Schreiber, N. M., Wuyts, S., et al. 2015, *ApJ*, **799**, 209
- Wisnioski, E., Mendel, J. T., Leaman, R., et al. 2025, *arXiv e-prints*, [arXiv:2505.24129](https://arxiv.org/abs/2505.24129)
- Wolfire, M. G., McKee, C. F., Hollenbach, D., & Tielens, A. G. G. M. 2003, *ApJ*, **587**, 278
- Wolfire, M. G., Vallini, L., & Chevance, M. 2022, *ARA&A*, **60**, 247
- Wuyts, S., Förster Schreiber, N. M., Wisnioski, E., et al. 2016, *ApJ*, **831**, 149
- Xu, D. & Yu, S.-Y. 2024, *A&A*, **682**, L17
- Zanella, A., Daddi, E., Magdis, G., et al. 2018, *MNRAS*, **481**, 1976
- Zolotov, A., Dekel, A., Mandelker, N., et al. 2015, *MNRAS*, **450**, 2327
- <sup>1</sup> Max-Planck-Institut für Extraterrestrische Physik (MPE), Gießenbachstra. 1, D-85748 Garching, Germany
- <sup>2</sup> Departamento de Astronomía, Universidad de Concepción, Barrio Universitario, Concepción, Chile
- <sup>3</sup> Millenium Nucleus for Galaxies (MINGAL)
- <sup>4</sup> Purple Mountain Observatory, Chinese Academy of Sciences, 10 Yuanhua Road, Nanjing 210023, China
- <sup>5</sup> Space Telescope Science Institute, 3700 San Martin D, MD 21218, USA
- <sup>6</sup> Department of Physics and Astronomy and PITT PACC, University of Pittsburgh, Pittsburgh, PA 15260, USA
- <sup>7</sup> Departments of Physics and Astronomy, University of California, Berkeley, CA 94720, USA
- <sup>8</sup> Max-Planck-Institut für Astrophysik (MPA), Karl-Schwarzschild-Str. 1, D-85748 Garching, Germany
- <sup>9</sup> Instituto de Estudios Astrofísicos, Facultad de Ingeniería y Ciencias, Universidad Diego Portales, Av. Ejército Libertador 441, Santiago, Chile [Código Postal 8370191]
- <sup>10</sup> Department of Astronomy, University of Virginia, 530 McCormick Road, Charlottesville, VA 22903, USA
- <sup>11</sup> National Radio Astronomy Observatory, 520 Edgemont Road, Charlottesville, VA 22903, USA
- <sup>12</sup> Jodrell Bank Centre for Astrophysics, Department of Physics and Astronomy, School of Natural Sciences, The University of Manchester, Manchester, M13 9PL, UK
- <sup>13</sup> Universitäts-Sternwarte Ludwig-Maximilians-Universität (USM), Scheinerstr. 1, München, D-81679, Germany
- <sup>14</sup> Centre for Astrophysics and Supercomputing, Swinburne University of Technology, Hawthorn 3122, Australia
- <sup>15</sup> Sterrenkundig Observatorium, Ghent University, Krijgslaan 281 S9, B-9000 Ghent, Belgium
- <sup>16</sup> Institute of Astrophysics, Foundation for Research and Technology - Hellas (FORTH), Heraklion 70013, Greece
- <sup>17</sup> School of Sciences, European University Cyprus, Diogenes Street, Engomi 1516, Nicosia, Cyprus
- <sup>18</sup> Las Campanas Observatory, Carnegie Institution of Washington, Casilla 601, La Serena, Chile
- <sup>19</sup> Department of Astronomy, School of Science, SOKENDAI (The Graduate University for Advanced Studies), 2-21-1 Osawa, Mitaka, Tokyo 181-8588, Japan
- <sup>20</sup> National Astronomical Observatory of Japan, 2-21-1 Osawa, Mitaka, Tokyo 181-8588, Japan
- <sup>21</sup> Department for Astrophysical & Planetary Science, University of Colorado, Boulder, CO 80309, USA
- <sup>22</sup> Department of Physics and Astronomy and George P. and Cynthia Woods Mitchell Institute for Fundamental Physics and Astronomy, Texas A&M University
- <sup>23</sup> Dept. Física Teórica y del Cosmos, E-18071 Granada, Spain
- <sup>24</sup> Instituto Universitario Carlos I de Física Teórica y Computacional, Universidad de Granada, E-18071 Granada, Spain
- <sup>25</sup> Osservatorio Astronomico di Padova, Vicolo dell'Osservatorio 5, Padova, I-35122, Italy
- <sup>26</sup> School of Physics and Astronomy, Tel Aviv University, Tel Aviv 69978, Israel
- <sup>27</sup> Centre for Computational Astrophysics, Flatiron Institute, 162 5th Avenue, New York, NY 10010, USA
- <sup>28</sup> Faculty of Engineering, Hokkai-Gakuen University, Toyohira-ku, Sapporo 062-8605, Japan
- <sup>29</sup> Department of Astronomy and Joint Space-Science Institute, University of Maryland, College Park, Maryland USA 20742

## Appendix A: Global properties of individual galaxies

For each galaxy individually, we briefly comment below on its global properties and its overall kinematic classification, based on the methods described in § 3. Detailed properties of CRISTAL-05 and 22 are presented in [Posses et al. \(2025\)](#) and [Telikova et al. \(2025\)](#), respectively. Figs. A.2 to A.4, from left to right, display the *JWST*, *HST* colour-composite images, the [C II] line emission, velocity and velocity dispersion maps. The velocity locus measured with SA in § 3.4 are overlaid on either the *JWST* or *HST* colour images in the rightmost column. The sizes and transparencies of these overlays are proportional to the positional uncertainty error. Figs. A.5 to A.7 shows additionally the p-v diagrams along the kinematic major and minor axes and the integrated spectrum. Where applicable, the quoted distance between companions is always projected.

**CRISTAL-01a:** Non-Disk. Identified as ‘Multi-UV’ in [Ikeda et al. \(2025\)](#) with *HST* data, *JWST* further supports that it is interacting with a massive neighbour SMG J1000+0234 and a companion at its north-east. It is also consistent with the multiple peaks in the integrated spectrum. The velocity field displays a gradient along the morphological minor axis observed in imaging data. This could suggest that this system is in its later phase of the merger, and the misaligned gradient may be a signature of gas inflow triggered by the merger. The interaction of the members in the CRISTAL-01 system is studied in more detail in [Solimano et al. \(2025\)](#).

**CRISTAL-01b:** Non-Disk. A pair of interacting systems, situated approximately  $\sim 48$  kpc south-east of CRISTAL-01a. The binary nature is conspicuous in both *HST* and *JWST* images, with the two components separated by a distance of  $\sim 7$  kpc. The [C II] line map shows emission south of the eastern companion, and there is an apparent spatial offset between the [C II] emission and the stellar component of the western companion, possibly originating from the gas that is being stripped away in the interaction. Although the eastern companion exhibits a velocity gradient transitioning from north to south, its dispersion appears disrupted, with elevated peaks in the north-eastern region.

**CRISTAL-02:** Disk. This system is also known as the LBG-1 in [Riechers et al. \(2014\)](#). The SMG AzTEC-3 ( $z = 5.298$ )  $\sim 90$  kpc away is also detected in [C II] at the edge of FoV. There is an overall isovelocity pattern consistent with disk rotation. The receding side is influenced by the interaction with the lower-mass satellite galaxy, resulting in a velocity reversal at the very north. The p-v diagram shows excess emission in high-velocity wings near the centre, which is associated with an outflow as evidenced in the integrated spectrum in Fig. A.6. NIRSpec/*JWST* data ( $R \sim 1000$ ) further confirms the biconical outflow signature ([Davies et al. 2025](#)). Considering the outflow and the interacting companion in the north, we therefore fit the emission in the p-v diagram (method detailed in § 3.1) with a broad and a narrow component (Fig. A.1). We attribute the narrower line to the bulk rotation motion, and the velocity and dispersion profiles derived from it are used in the analysis in § 5.1. By removing the broad component, we effectively minimise the contributions from the outflow and the satellite galaxy.

**CRISTAL-03:** Best Disk; Velocity gradient is along the overall morphological PA of the *HST* and *JWST* images, but not with that of [C II], especially at the outer isophotes due to the protrusion at the south-west. Although this galaxy is the most poorly resolved in our sample, the NIRSpec/*JWST* data with  $5\times$  better angular resolution reveals a consistent rotational pattern in H $\alpha$  ([W. Ren et al., in prep.](#)). This galaxy is also flagged as the most evident candidate for an AGN, which could potentially account for the protruded [C II] emission towards the south-west, and the slight deviation from the uni-directional SA locus in Fig. A.2.

**CRISTAL-04a:** Non-Disk; Have a velocity gradient running from south to north and elevated dispersion along the zeroth velocity contour. However, the velocity isocontours deviate substantially from a spider diagram, and the p-v diagram along the major axis is primarily flat. The perturbation is most likely due to its recent minor-merger interaction with CRISTAL-04b (mass ratio  $\sim 17:1$ , [Herrera-Camus et al. 2025](#)). CRISTAL-04a and CRISTAL-04b are identified as ‘Pair’ in [Ikeda et al. \(2025\)](#).

**CRISTAL-04b:** Non-Disk; A blob of faint [C II] emission  $\sim 10$  kpc north of CRISTAL-04a that does not show a clear rotating signature. It could comprise two smaller substructures, as evidenced by the [C II] line map and the *JWST* images.

**CRISTAL-06a:** Non-Disk. Possibly a counter-rotating binary merger of two disks, where we observe a reversal in velocity gradient along the major axis, yet the individual components remain spatially unresolved at the current resolution. This system was also classified as a pair-merger in association with CRISTAL-06b in [Le Fèvre et al. \(2020\)](#) and is the only multiple-[C II] system in [Ikeda et al. \(2025\)](#). Alternatively, it could be a single disk with the approaching side at the east perturbed by CRISTAL-06b, as hinted by a velocity dispersion that peaks where the gradient is steepest. [Ikeda et al. \(2025\)](#) identified the multi-[C II] nature within CRISTAL-06a, while CRISTAL-06a and CRISTAL-06b are identified as ‘Pair’ in [Ikeda et al. \(2025\)](#).

**CRISTAL-06b:** Disk; it is located  $\sim 10$  kpc north-east of CRISTAL-06a with its velocity and dispersion fields consistent with a rotating disk. The slightly twisted velocity isocontours is likely a result of the perturbation from CRISTAL-06a, which is  $8\times$  more massive ([Herrera-Camus et al. 2025](#)).

**CRISTAL-07a:** Disk. It exhibits a clear velocity gradient from north to south, but the northern part is perturbed by its interaction with CRISTAL-07b (mass ratio  $\sim 2:1$ ) in the early phase. In the kinematics modelling, we symmetrise the velocity dispersion profile from the receding and approaching sides (following [Posses et al. 2025](#)) to reduce the impact of the interaction on the intrinsic dispersion, as the receding side is much less perturbed.

**CRISTAL-07b:** Non-Disk, an interacting neighbour with CRISTAL-07a separated by  $\sim 8$  kpc; there is an overall velocity gradient stretching from east to west, but the isovelocity contours are more disrupted compared to CRISTAL-07a due to its lower mass. CRISTAL-07a and CRISTAL-07b are identified as ‘Pair’ in [Ikeda et al. \(2025\)](#), while CRISTAL-07 as a whole was classified as a pair-merger in [Le Fèvre et al. \(2020\)](#).

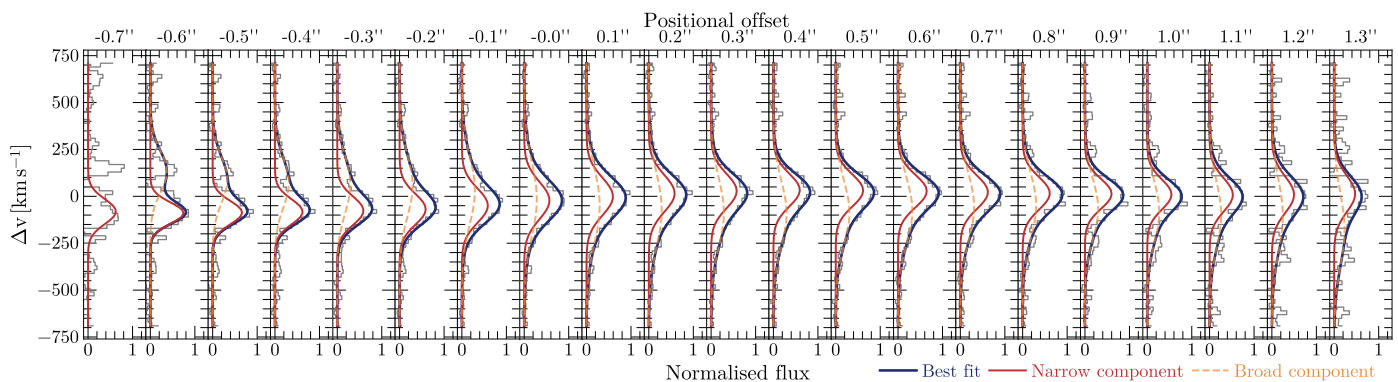


Fig. A.1: Two-component Gaussian fit (blue thick line) of CRISTAL-02 emission profile along each column in the position-velocity (p-v) diagram (grey lines) extracted along the kinematic major axis. The underlying p-v diagram from which the profiles are extracted is shown in Figure A.6 in the Appendix A. We assume the narrow component (red) to trace the bulk rotation motion of the gas, which will be used for subsequent kinematics modelling, while the broad component (orange) is associated with the outflow and the interacting companion in the north (at offset  $\geq 0''.8$ ). For other galaxies, we assume a single Gaussian profile using the same extraction method.

**CRISTAL-07c:** Non-Disk; an interacting system of comparable masses locates at 140 kpc west of CRISTAL-07a and CRISTAL-07b.

**CRISTAL-08:** Disk. It exhibits a remarkably smooth velocity gradient, although there is a change of isovelocity contours PA from south to west (visible also in the SA locus), likely due to non-circular motion along the minor axis (H. Herrera-Camus et al. 2025c, in prep.). The velocity dispersion peaks at the south-west corner, away from the morphological centre and peak of the [C II] line emission; The JWST colour image shows a very clumpy appearance (see also the F444W residual image in Fig. B.1) similar to the galaxy in Tanaka et al. (2024) at  $z = 4.91$ , with clumps of various colours distributed from 8 o'clock to 2 o'clock positions. The disk classification is consistent with the 'rotating disk' classification in Le Fèvre et al. (2020). Herrera-Camus et al. (2025) will present the detailed properties of the clumps.

**CRISTAL-09:** Disk. Observed as a compact object in the *HST* image, *JWST* reveals extended stellar light at the south-west at faint levels. The extended stellar component is more apparent in the residual left after subtracting a Sérsic model (Fig. B.1). [C II] data provides tentative evidence of disk rotation but is still limited by the angular resolution and S/N. This system was classified as a pair-merger in Le Fèvre et al. (2020).

**CRISTAL-10a:** Non-Disk. No *JWST* image is available for this system. Based on the *HST* data, Ikeda et al. (2025) classified it as a Multi-UV system, with the two UV components separated by  $\sim 5.5$  kpc. [C II] line map shows a consistent separation of the two components. Consider the two components as one system, it exhibits a monotonic velocity gradient from north-east to south-west across the two components, with a prominent dispersion peak where the velocity gradient is steepest. However, the Gaussian fit errors at the dispersion peak are large due to low S/N. SA locus and p-v diagram reveals an abrupt velocity jump between the east (CRISTAL-10a-E) and west components, with a clear gap in the velocity structure, coinciding with that in the *HST* image. This suggests that the velocity gradient is

plausibly driven by the orbital motion of the two components. Notably, this system shows a strong [C II]/FIR deficit (Herrera-Camus et al. 2025), with prominent dust continuum emission where [C II] emission is weakest, particularly around the southern parts of both components. While this could indicate that the CRISTAL-10a and CRISTAL-10b are substructures of a single larger system, the [C II] kinematics does not support the interpretation for now, so we classify the system as Non-Disk.

**CRISTAL-10a-E:** Disk. The east component of CRISTAL-10a. Despite being in a potentially interacting system, it shows a very promising disk-rotating signature in its own velocity and dispersion maps. The SA locus and p-v diagram resemble a disk-like system but also exhibit features indicative of interaction with the western component.

**CRISTAL-11:** Disk. We observe a velocity gradient from south-east to north-west, with a dispersion peak near the morphological centre. The kinematic PA is aligned with the morphological PA in both *JWST* and *HST* images with a difference of  $< 10^\circ$ . However, the north-west region appears more dust-attenuated and has a distinct colour compared to the south-east, suggesting a possible merger of the two systems. Higher resolution data would be required to discern the true nature of this system. Nevertheless, based on the available data, we maintain our classification as a Disk. Le Fèvre et al. (2020) classified this system as 'extended and dispersion-dominated'.

**CRISTAL-12:** Disk. The least massive system among CRISTAL with a shallow velocity gradient. It is classified as 'compact' in Le Fèvre et al. (2020) and, even with our higher resolution data, it remains poorly resolved, with only a tentative velocity gradient from west to east. There is a faint [C II] emission blob  $\sim 4$  kpc away in the north-west, but no visible counterpart in *HST* and *JWST* images. This emission is linked to the elevated dispersion at the north-west. This feature is also seen in other disk systems, CRISTAL-02, 15, 19 (and 03, although poorly resolved), which may suggest an outflow origin of the gas. However, except for CRISTAL-02, deeper data will be required to confirm this speculation.



**CRISTAL-13:** Non-Disk. Already noted by Ikeda et al. (2025) about its multi-UV appearance in *HST*, *JWST* images further reveal the intriguing structure of the eastern and western components. The compact western source is dominated by an older stellar population (Lines et al. 2025) situated adjacent to a clumpy, blue eastern tail. The clump properties are addressed in Herrera-Camus et al. (2025). While both the velocity and dispersion maps exhibit characteristic signatures of a rotating disk, the p-v diagrams along both the major and minor axes show features that deviate substantially from typical disk-like rotation. SA indicates receding motion along the blue tail, suggesting that this system is likely the result of a merger between the western and eastern sources.

**CRISTAL-14:** Non-Disk. We observe an apparent velocity gradient from north-east to south-west. However, a centralised dispersion peak is absent. Furthermore, the p-v diagrams do not display the characteristic patterns associated with disk-like rotation. Both *HST* and *JWST* images reveal a western component with a distinct colour that is faint in [C II]. The [C II] emission predominantly traces the eastern component, which contributes the majority of the velocity gradient. Therefore, it is likely that this system is similar to CRISTAL-13, with the eastern source being in a close encounter with the western source.

**CRISTAL-15:** Best Disk. We observe a velocity gradient from south-east to north-west, which agrees with the uni-directional locus traced by SA. An extended [C II] structure is present at the north-east of the kinematic minor axis, which could indicate slow outflowing gas (see also CRISTAL-12), as there is no significant broad emission component in the integrated spectrum. The ‘root’ of this extended structure is also co-spatial with the elevated dispersion in the dispersion map. *JWST* data reveals three clumps of bluer colour embedded within a redder disk, which is also more evident in the F444W residual image in Fig. B.1. We notice that the peak-to-peak velocity difference of CRISTAL-15 is only  $50 \text{ km s}^{-1}$ , and our ALMA data cube is binned to  $20 \text{ km s}^{-1}$ , which barely samples the velocity gradient. The data cube binned to  $10 \text{ km s}^{-1}$  is too low S/N for robust extraction of the RC and dispersion profile. As a result, the derived velocity dispersion in § 5 for CRISTAL-15 may still be contaminated by the contribution of the unresolved velocity gradient.

**CRISTAL-16a,b:** Non-Disk; Similar to CRISTAL-01b and CRISTAL-06, this system is an interacting pair consisting of at least two companions, CRISTAL-16a and CRISTAL-16b, separated by a distance of  $\sim 5.3 \text{ kpc}$ . The eastern companion, CRISTAL-16a, appears to be composed of two clumps separated by  $\leq 2 \text{ kpc}$ , similar to CRISTAL-02, although it is unclear whether these clumps represent separate galaxies in a merger, or multiple star formation clumps within a galaxy. The [C II] line map reveals two barely resolved emission peaks co-spatial with the two companions of CRISTAL-16a. When considering CRISTAL-16a as a whole, the global velocity gradient is aligned with the morphological minor axis. Interestingly, the zeroth-velocity contour coincides with the dispersion peaks, suggesting a possible scenario in which two disk-like systems are approaching each other along their respective minor axes. The *JWST*/F444W image (Fig. B.1) reveals a conceivable connecting ‘bridge’ between the north-east and south-west clumps within CRISTAL-16a, providing further evidence for an interaction. CRISTAL-16b is too faint in [C II] for kinematics extraction.

Overall, CRISTAL-16a system bears similarities to CRISTAL-07a and 07b, but perhaps with a different orbital configuration. However, the individual components remain spatially unresolved at the current resolution.

**CRISTAL-19:** Best Disk; The velocity map, SA locus and p-v diagram all show a coherent velocity gradient with little deviation from symmetry. The dispersion peak coincides with the position of the steepest velocity gradient. There is no evidence of a physically associated neighbour in the available data. Despite having a high intrinsic dispersion ( $\sigma_0 = 65 \text{ km s}^{-1}$ ), the system’s  $V_{\text{rot}}/\sigma_0 \approx 2.2$  ratio indicates it is not dispersion-dominated, contrary to the classification in Le Fèvre et al. (2020).

**CRISTAL-20:** Best Disk; It is one of the CRISTAL pilot galaxies first studied by Herrera-Camus et al. (2022), which also presented its outflow properties. The velocity map shows the typical rotating pattern of a disk, while the dispersion map shows the expected outflow signature at the north-west. SA aligns unidirectionally with the observed gradient in the velocity map; p-v diagrams along the major axis show a clean S-shape, while along the minor axis, no velocity gradient is seen, indicative of a classical disk. Parlanti et al. (2025) presented the NIRSpec/*JWST* data of the ionised gas outflow traced by [O III] $\lambda 5007 \text{ Å}$  and a merger scenario based on the ionised gas.

**CRISTAL-21:** Non-Disk; The velocity gradient is from north to south, but the dispersion map shows multiple peaks. The SA locus also displays a chaotic distribution within the central region, which could indicate unresolved line-of-sight mergers. It is consistent with the very elongated shape of the p-v diagram, stretching from  $-500 \text{ km s}^{-1}$  to  $500 \text{ km s}^{-1}$  within the central  $\sim 2 \text{ kpc}$  region, indicative of an absence of a global velocity gradient. Although this could also be caused by a strong outflow at the centre, Lambert et al. (2023) found no evidence of outflows from the system, as indicated by the absence of a broad secondary component in the [C II] spectrum. Instead, the observed disturbed gas and dust emission, combined with its kinematics structure, suggest that the system is in a late-stage merger. NIRCам/*JWST* images reveal a blue ‘clump’ located at the east side of the [C II] light centre, which could be the merger companion.

**CRISTAL-23a:** Non-Disk. One of the companions (source C) in the ‘triple-merger’ system was first studied in detail by Jones et al. (2021). As noted by Jones et al. (2021), it is in proximity to the massive protocluster PC1 J1001+0220 (Lemaux et al. 2018). Since it lies along the major axis of the protocluster and is only  $\sim 3.5 \text{ Mpc}$  from the north-east component of this protocluster, it could be associated with the system in a filamentary structure. Because of a different slit angle chosen, we observe a velocity gradient from north to south of this source, in contrary to Jones et al. (2021). The p-v diagram however exhibits substantial broadening along the velocity axis in the central region, which is inexplicable by a disk origin (e.g. an outflow).

**CRISTAL-23b:** Disk; Source E in Jones et al. (2020). The velocity gradient exhibits a clear East-West orientation, consistent with SA analysis. The velocity dispersion is elevated around the zero-velocity contour. The p-v diagram along the major axis displays a characteristic disk profile, whereas the minor axis p-v



diagram shows a slight deviation, likely attributed to the ongoing interaction with CRISTAL-23a.

**CRISTAL-23c:** Disk; Noted also by [Devereaux et al. \(2024\)](#), it is the least luminous of the three sources in the CRISTAL-23 system and is likely to be rotating. It is separated from CRISTAL-23a and 23b in velocity by  $\sim 300 \text{ km s}^{-1}$  and spatially by 18 kpc. The velocity and dispersion map of this galaxy showed signs of disk rotation but is slightly perturbed by its interaction with CRISTAL-23a and 23b. It is the source W in [Jones et al. \(2020\)](#).

**CRISTAL-24:** Non-Disk; Multiple dispersion peaks in the dispersion map; SA does not show a large-scale velocity gradient, with a closely spaced locus suggesting a line-of-sight merger, which is further supported by the almost vertical position-velocity diagram along the major axis. Morphological and kinematic studies by [Devereaux et al. \(2024\)](#) rejected the outflow scenarios. This galaxy has the largest integrated line width  $\sigma_{\text{int}} \approx 300 \text{ km s}^{-1}$ . Although CRISTAL-07 is 130 kpc (projected) away, it is not associated with CRISTAL-24 with a redshift difference of  $\Delta z \approx 0.6$ .

**CRISTAL-25:** Non-Disk; Although [Devereaux et al. \(2024\)](#) previously dismissed the merger scenario based on the *HST* morphology and dust continuum emission, the disjoint velocity structure in the p-v diagram, the well-defined velocity gradients of each component (Fig. A.7), with the northern component displaying a clear dispersion peak, could be indicative of a merger.

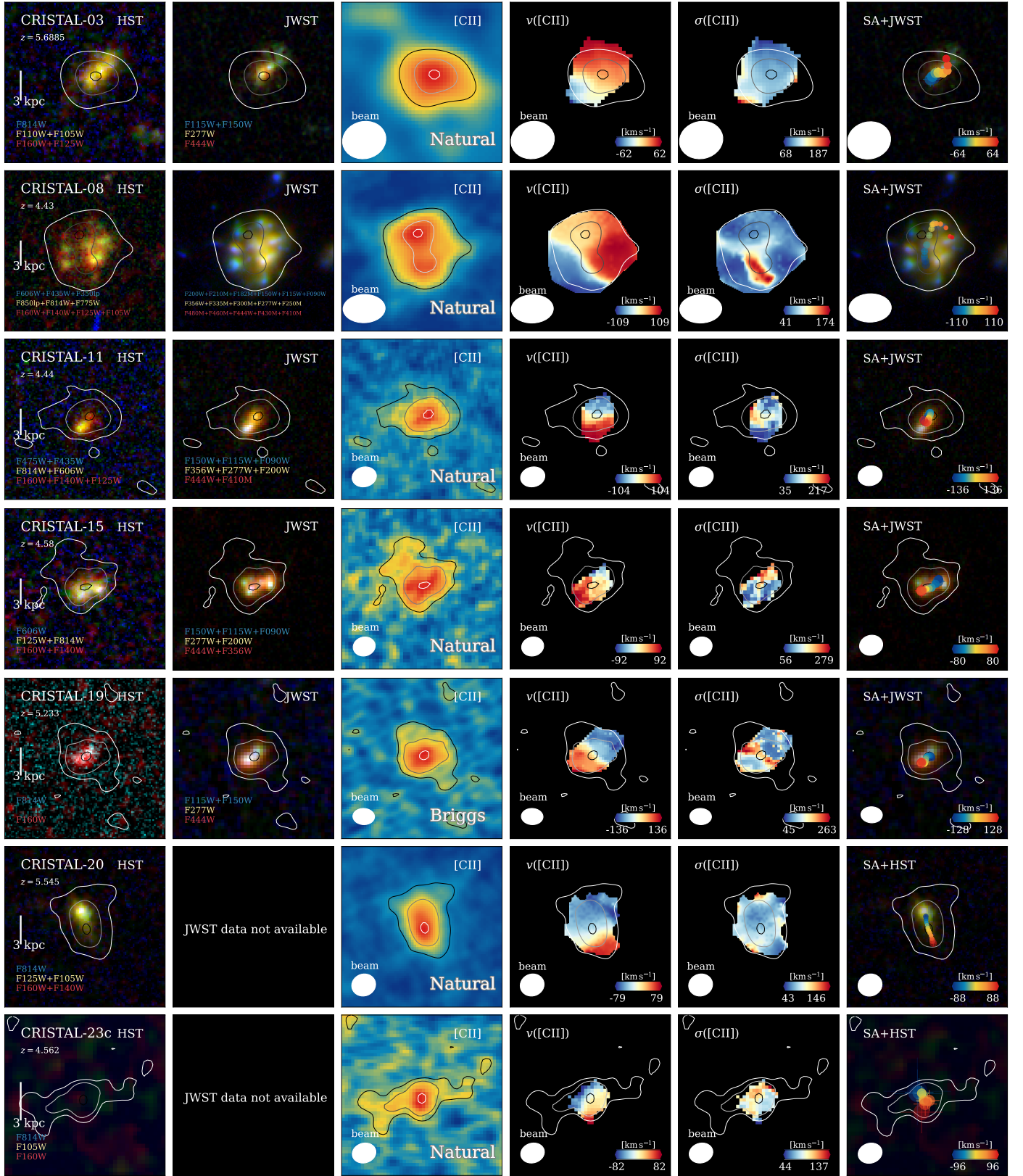


Fig. A.2: Gallery showing the multi-wavelength properties of the Best Disk. The first column displays the colour-composite images from *HST*, and if available, NIRCcam/*JWST* images are shown in the second column. The third to fifth columns are ALMA images of [C II] emission, shown as line intensity, velocity, and velocity dispersion maps. The velocity and velocity dispersion maps are obtained by pixel-by-pixel single Gaussian fitting to the natural-weighted line cube, binned at  $\Delta V = 20 \text{ km s}^{-1}$  spectral resolution. They are *not* corrected for spectral broadening, beam-smearing and projection. The last column shows the spectro-astrometry (SA) measurement overlaid on *HST* (or NIRCcam/*JWST* if available) colour images, in which the sizes and transparencies of the points are proportional to the positional uncertainties derived using Equation 1 in Condon et al. (1998). For all panels, the contours correspond to the intensities of the [C II] line map, plotted from  $1.5\sigma$  to  $3\sigma$ .

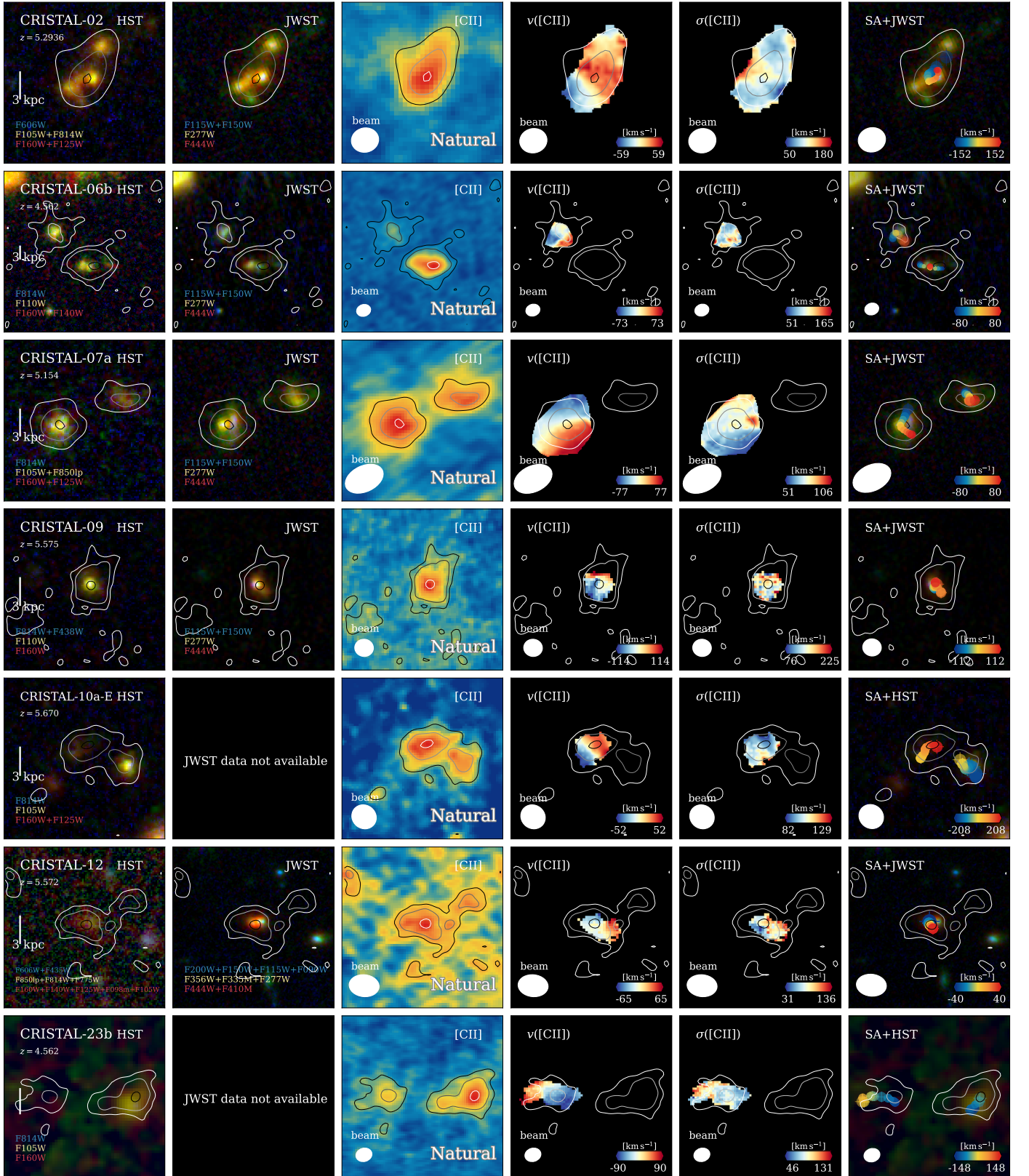


Fig. A.3: Same as Figure A.2, but for the Disk.



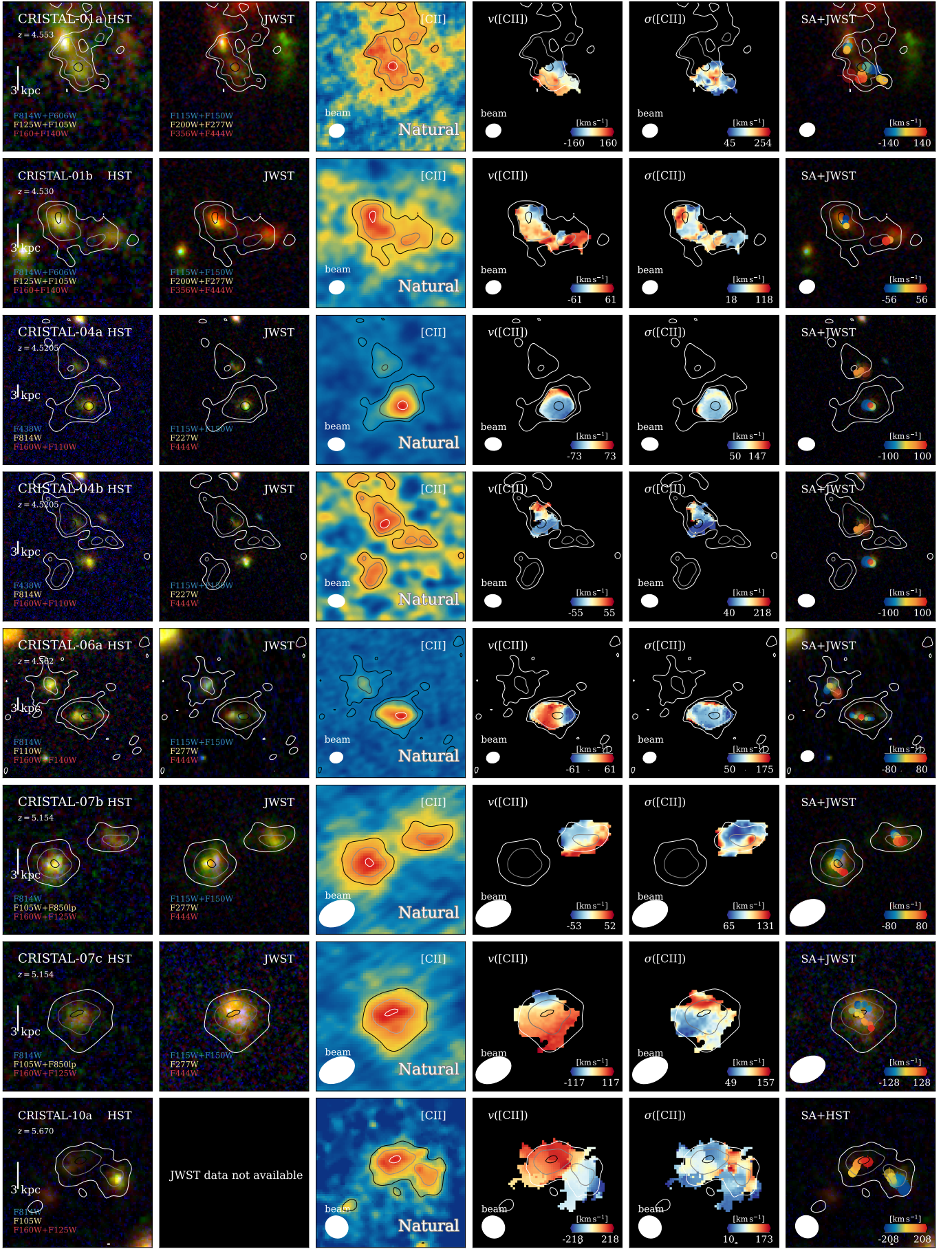


Fig. A.4: Same as Figure A.2, but for the Non-Disk. For CRISTAL-01a and 04b, we subtract the bright companions to improve visual contrast.



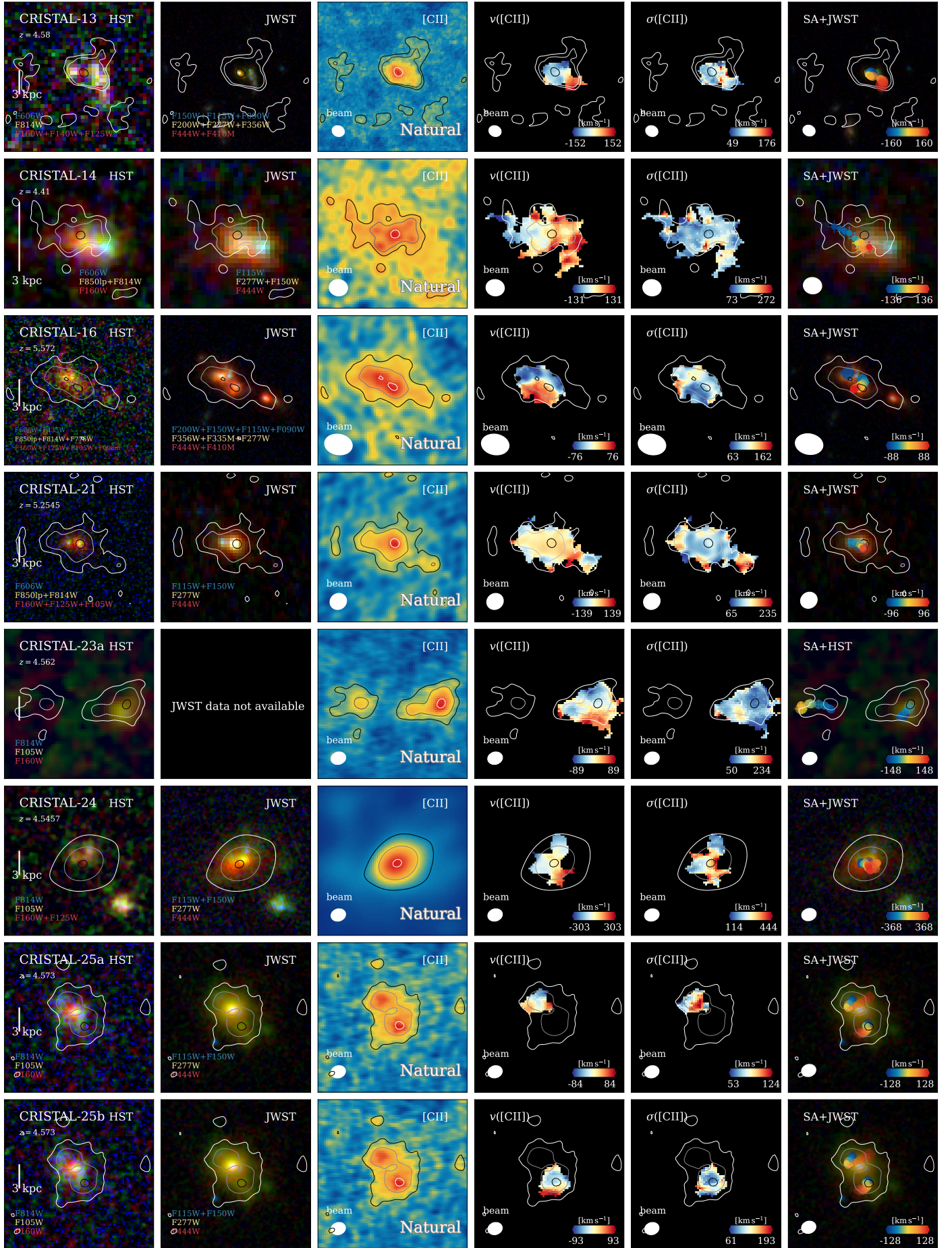


Fig. A.4: (Continued.)

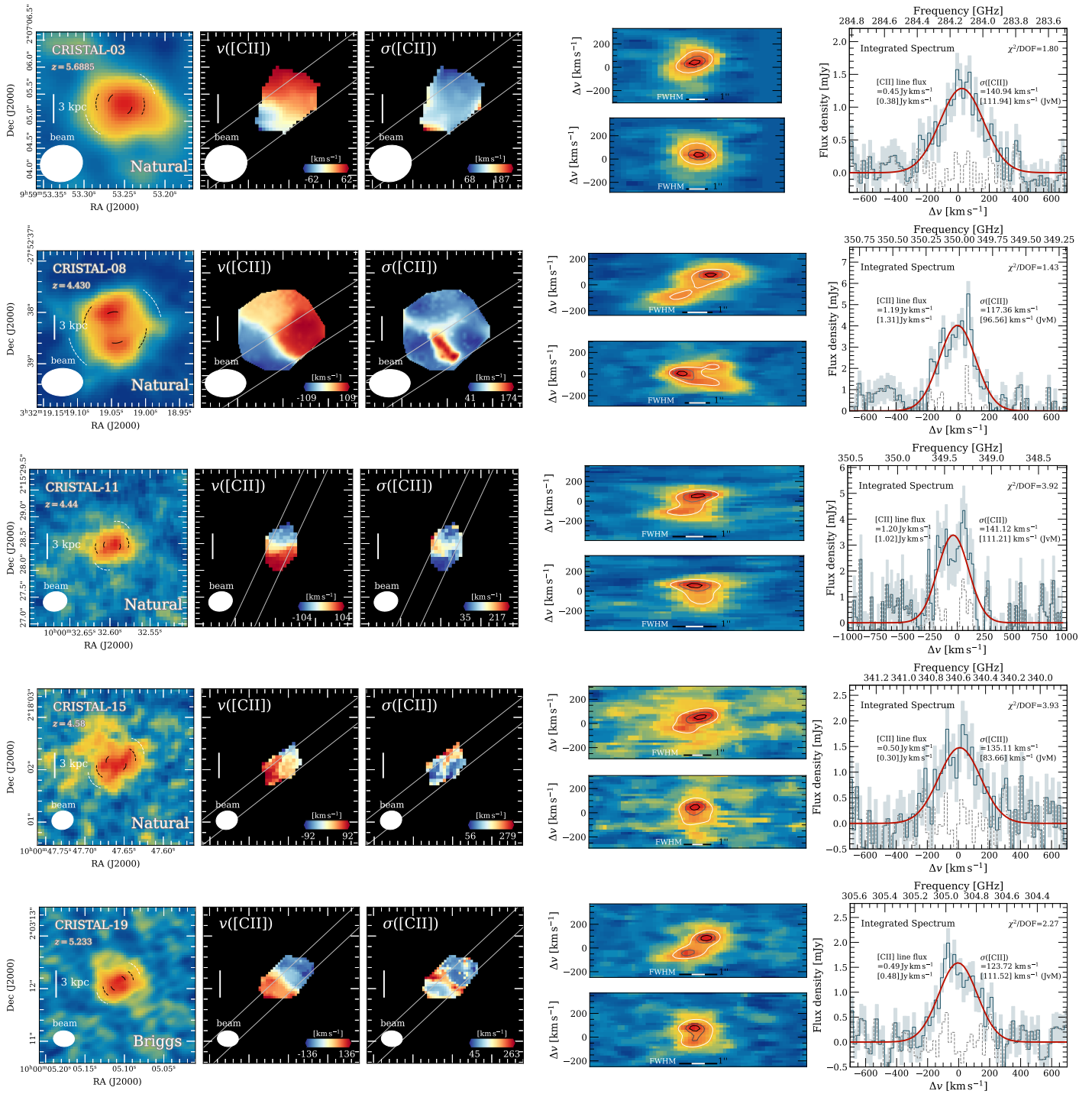


Fig. A.5: [C II] line maps, velocity maps, dispersion maps, position-velocity (p-v) diagrams (with median filtering applied for visual purpose), integrated spectra and shifted spectra of the Disk. In the [C II] line maps, the dashed pairs of arcs delineating the emission indicate the apparent morphological position angle (PA<sub>m</sub>, black) and the kinematic major axis (white). The solid pair of arcs represent the intrinsic PA<sub>m</sub> after correcting for the beam. In the p-v diagrams, the black and white horizontal bars correspond to 1'' and the synthesised beam FWHM, respectively.

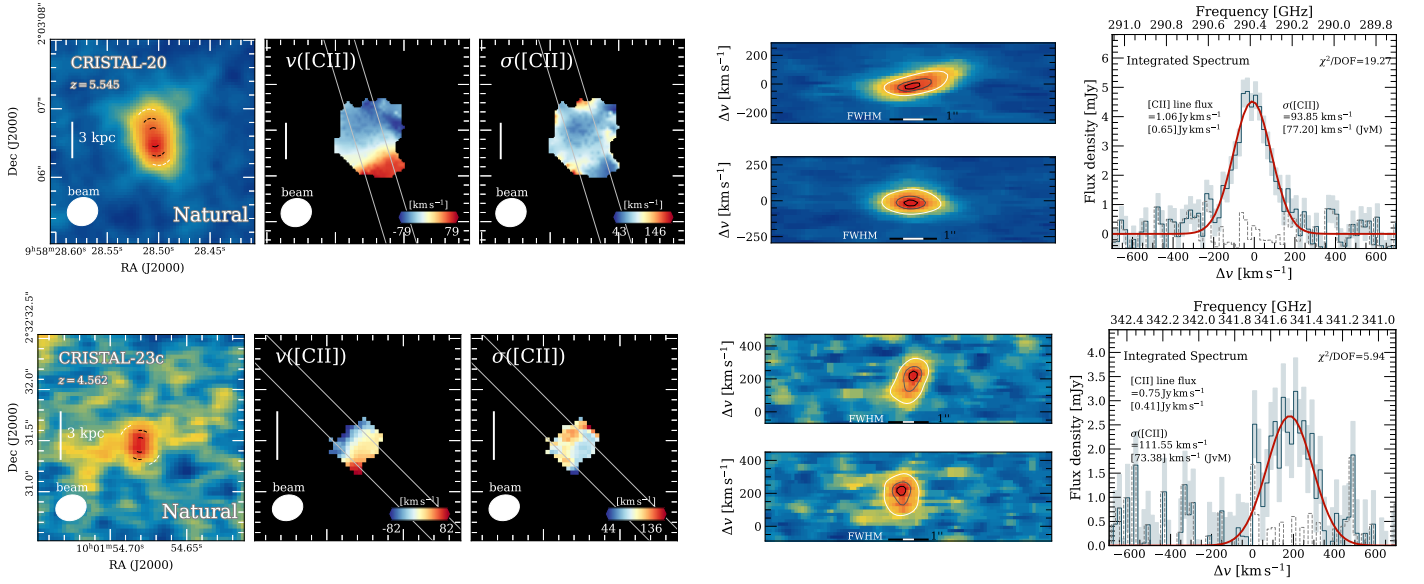


Fig. A.5: (Continued.)



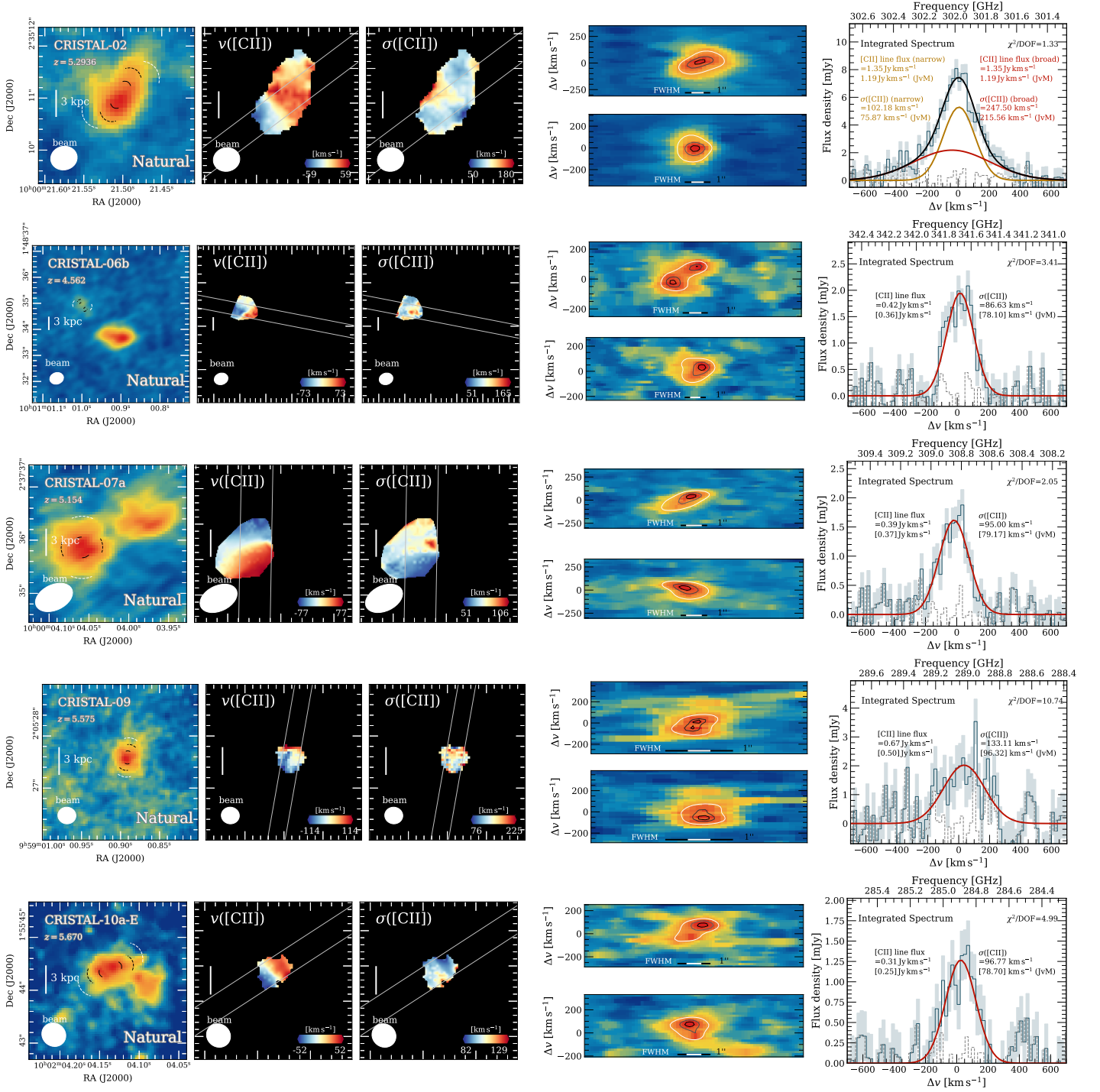


Fig. A.6: Same as Figure A.5, but for the Disk.

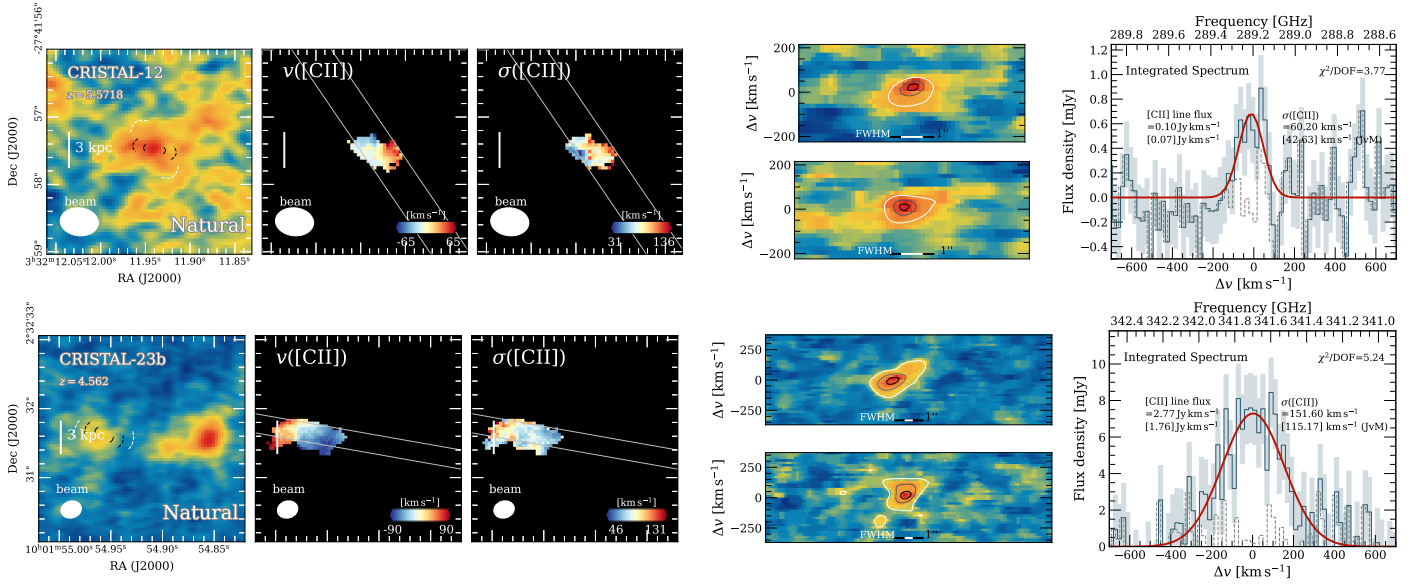


Fig. A.6: (Continued.)

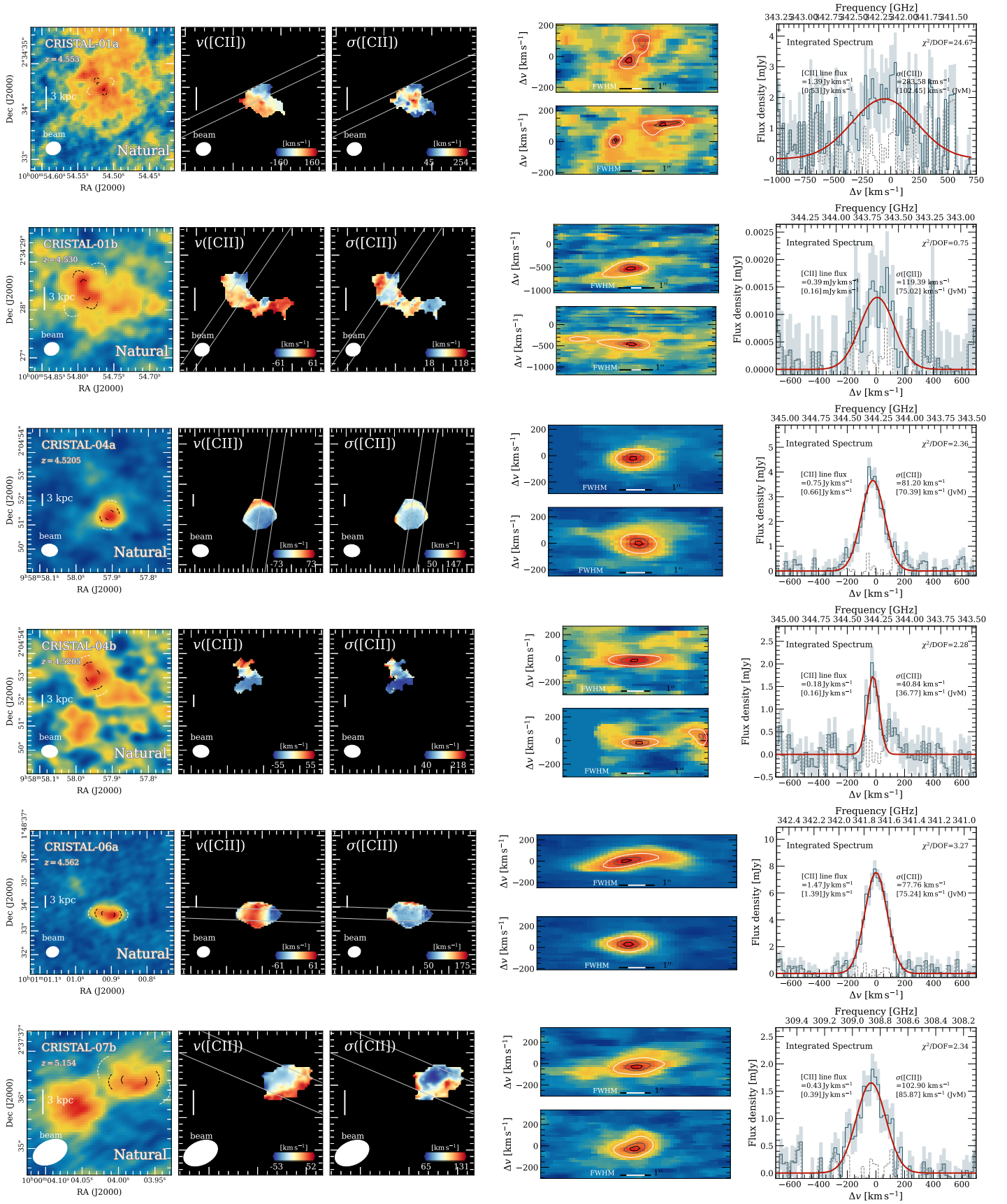


Fig. A.7: Same as Figure A.5, but for the Non-Disk. For CRISTAL-01a and CRISTAL-04b, the bright companions are subtracted from the line maps for better visual contrast.

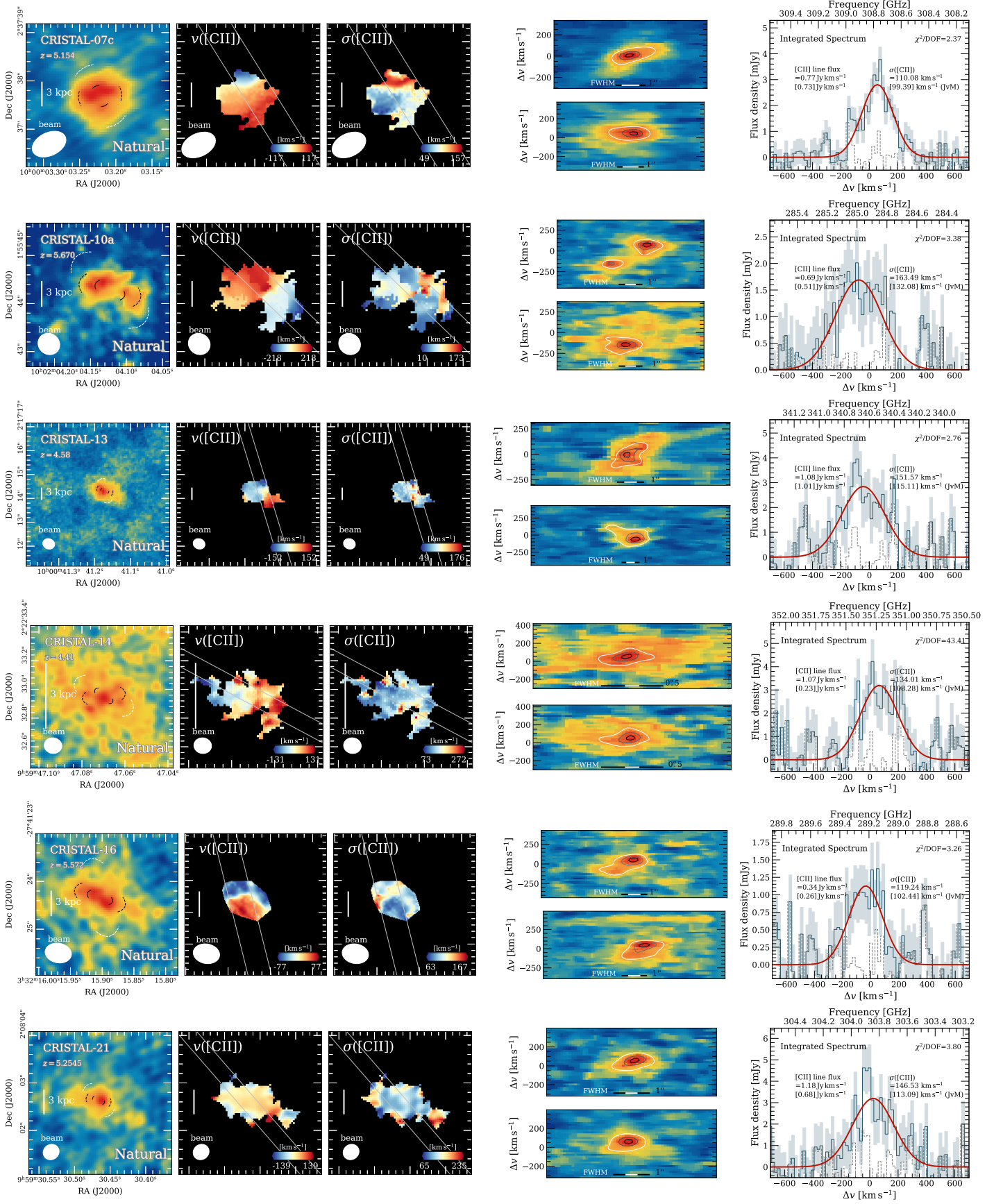


Fig. A.7: (Continued.)



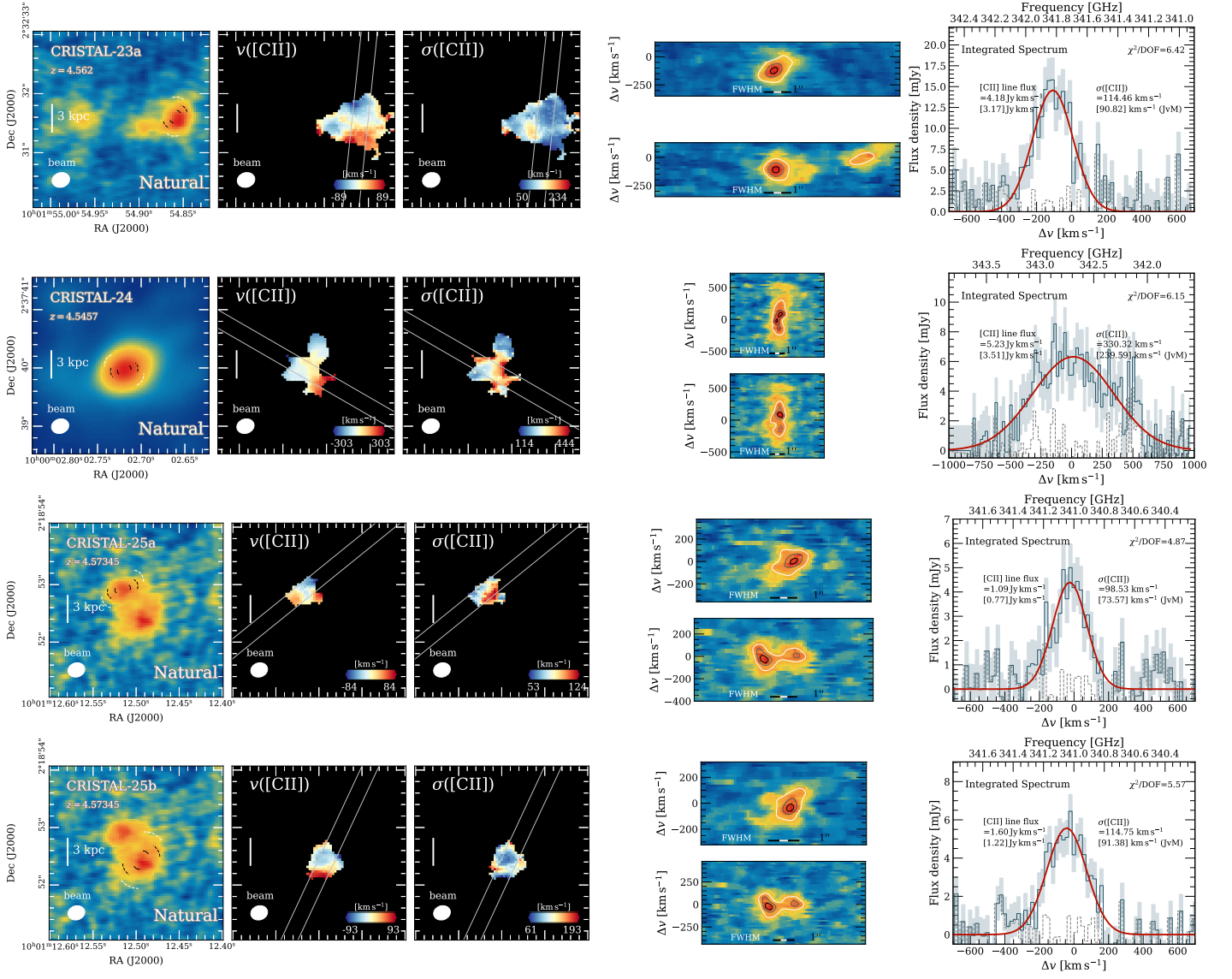


Fig. A.7: (Continued.)

## Appendix B: Structural parameters fit of NIRCam/F444W images

We fit the 2D light distributions of the galaxies observed with NIRCam/JWST F444W with *imfit* (Erwin 2015), accounting for the PSF. The PSF model adopted is described in Li et al. (2024). We assume a Sérsic profile with variable Sérsic index  $n$  and fixed  $n = 1$ . When let free,  $n$  freely varying within [0.5, 6]. We also let the effective radius ( $R_e$ ), the ellipticity  $e = 1 - b/a$ , and the position angle (PA) of the major axis as free parameters. Table B.1 lists the best-fit structural parameters of the galaxies for variable  $n$ . Average Sérsic index and effective radius are  $\langle n \rangle = 1.1 \pm 0.2$ ,  $\langle R_{e,4\mu\text{m}} \rangle = 1.46 \pm 0.04$  kpc, respectively. The effective radius is  $\sim 1.5\times$  that of the rest-frame UV emission  $\langle R_{\text{eUV}} \rangle \approx 0.98$  kpc (for the same sources considered, Ikeda et al. 2025). Our  $\langle R_{e,4\mu\text{m}} \rangle$  is comparable to that of the dust continuum emission  $\langle R_{\text{e,dust}} \rangle \approx 1.78$  kpc (Mitsunashi et al. 2024), but is smaller than the [C II] sizes  $\langle R_{\text{e,[C II]}} \rangle \approx 1.9$  kpc (Ikeda et al. 2025). Fixing  $n = 1$  in our fit gives  $\langle R_{e,4\mu\text{m}} \rangle = 1.77$  kpc. For consistency, we use this  $n = 1$   $R_e$  as the initial guess for the dynamical modelling.

In comparison, van der Wel et al. (2014), which covers  $0 < z < 3$  galaxies observed in the  $H_{160}$  band, the expected value for SFGs extrapolated to  $z = 5$  and  $\log M_*/M_\odot = 10$  is 2.4 kpc, our  $R_{e,4\mu\text{m}}$  is on average 40% smaller, but is still within the  $\sim 0.2$  dex scatter at  $z \approx 3$ .

## Appendix C: Molecular gas fractions $f_{\text{molgas}}$

Previous studies of MS SFGs at  $z \sim 1\text{--}3$  have shown that their gas kinematics are closely tied to their molecular gas content (e.g. Wisnioski et al. 2015; Übler et al. 2019) inferred from scaling relations. We similarly explore the relationship between the kinematic properties of CRISTAL disks and their gas fractions in §§ 6.1–6.2. As a first step, we need to estimate the gas content of our sample galaxies.

Measuring the gas content of CRISTAL galaxies using CO emission, which is a well-calibrated  $\text{H}_2$  tracer at low- $z$ , is challenging in our case due to the cosmic dimming effect and typically low metallicities of galaxies, exacerbated by the higher temperature of the cosmic microwave background for lower- $J$  transitions ( $T_{\text{CMB}}(z) = 2.73(1+z)$  K). Furthermore, the lack of multi-band observations for all galaxies, which would be necessary to constrain the full far-infrared (FIR) SED shape (e.g. Béthermin et al. 2015; Kaasinen et al. 2019), means that the only feasible estimator for most galaxies in CRISTALfootnote Data from Very Large Array (VLA) observations of CO(2-1) are available for CRISTAL-22 (HZ10) and CRISTAL-02 (LBG-1). is to infer gas masses from the single-band dust continuum emission measured in the Rayleigh-Jeans (R-J) tail of the FIR SED following the method of Scoville et al. (2016, 2017).

With the rest frequencies probed by the Band-7 (343.5 GHz) continuum data and if we adopt  $\lambda_0 = 100\mu\text{m}$  similar to Faisst et al. (2020a), which is the wavelength where optical depth reaches unity, and single dust temperature of  $T_{\text{dust}} = 50$  K (see discussion below), then we can assume the R-J regime criterion is still satisfied and optically-thin approximation is valid. We measure the dust continuum fluxes on the image directly using the curve-of-growth method. They are in general good agreement with Mitsunashi et al. (2024).

We infer the gas mass  $M_{\text{gas}}$  from the observed flux density  $S_{\nu_{\text{obs}}}$  of the Band-7 dust continuum ( $\lambda_{\text{obs}} \approx 850\text{--}1050\mu\text{m}$ ) in the

Table B.1: Rest-frame optical to near-IR (F444W) structural parameters fitted by *imfit*.

ID	$R_e^a$ (kpc)	$n^b$	$e^c$	PA <sup>d</sup> (°)	$i^e$ (°)
01a	1.3	2.5	0.00	...	...
	2.3	1.9	0.51	9	64
02	1.7	0.5	0.30	150	48
03	1.3	2.0	0.57	135	69
04a	1.2	1.1	0.04	...	...
04b	2.8	1.5	0.00	...	...
06a	1.6	0.7	0.61	86	72
06b	1.2	0.4	0.25	141	43
07a	1.5	1.1	0.26	126	44
07b	1.4	1.0	0.27	52	45
07c	1.6	0.4	0.24	33	42
08	2.7	0.8	0.29	166	46
09	0.8	1.2	0.39	37	55
11	1.1	0.1	0.71	146	82
12	0.9	0.6	0.43	92	58
13a	2.2	0.1	0.64	77	75
14	1.3	1.1	0.36	85	52
15	2.3	0.0	0.62	108	73
16a	1.4	0.8	0.32	251	49
	0.6	0.4	0.22	122	40
16b	1.5	1.3	0.55	70	67
19	1.0	0.7	0.54	124	66
21	0.6	3.6	0.18	65	36
	0.5	0.5	0.10	6	26
24	1.9	0.8	0.46	112	60
25	0.7	2.5	0.20	85	39

Notes. <sup>(a)</sup> Intrinsic half-light radius. <sup>(b)</sup> Sérsic index. <sup>(c)</sup> Intrinsic ellipticity ( $e = 1 - b/a$ ). <sup>(d)</sup> Position angle (counter-clockwise from north). <sup>(e)</sup> Inclination inferred from Equation 2. <sup>(†)</sup> The ellipticity is too low. Targets with two entries are fitted with a double-Sérsic profile. CRISTAL-10, 20, 23 systems do not have NIRCam data available.

R-J regime following Eq. (3) in Tacconi et al. (2020):

$$\left( \frac{M_{\text{gas}}}{1 \times 10^{10} M_\odot} \right) = \left( \frac{S_{\nu_{\text{obs}}} D_L^2}{\text{mJy Gpc}^2} \right) \times (1+z)^{-(3+\beta)} \times \left( \frac{\delta_{\text{gd}}}{150} \right) \times \left( \frac{\nu_{\text{obs}}}{352 \text{ GHz}} \right)^{-(2+\beta)} \times \left( \frac{6.7 \times 10^{19}}{\alpha_{\text{dust},0}} \right) \times \frac{\Gamma_0}{\Gamma_{\text{R-J}, \nu_{\text{obs}}}} \quad (\text{C.1})$$

We introduced the R-J departure coefficient  $\Gamma_{\text{R-J}}$  back to Eq. (C.1) to account for the deviation of dust temperature from 25 K, which was originally used in Tacconi et al. (2020).  $\Gamma_{\text{R-J}}$  is defined as (Eq. (6) in Scoville et al. 2016)

$$\Gamma_{\text{R-J}}(T_d, \nu_{\text{obs}}, z) = \frac{h\nu_{\text{obs}}(1+z)/kT_d}{e^{h\nu_{\text{obs}}(1+z)/kT_d} - 1}. \quad (\text{C.2})$$

The  $\Gamma_0$  factor in Eq. (C.1) is taken at  $z = 0, T_d = 50$  K (see below) and at the respective  $\nu_{\text{obs}}$  for different observations. On average, the coefficient  $\langle \frac{\Gamma_0}{\Gamma_{\text{R-J}, \nu_{\text{obs}}}} \rangle \sim 2.4$ .



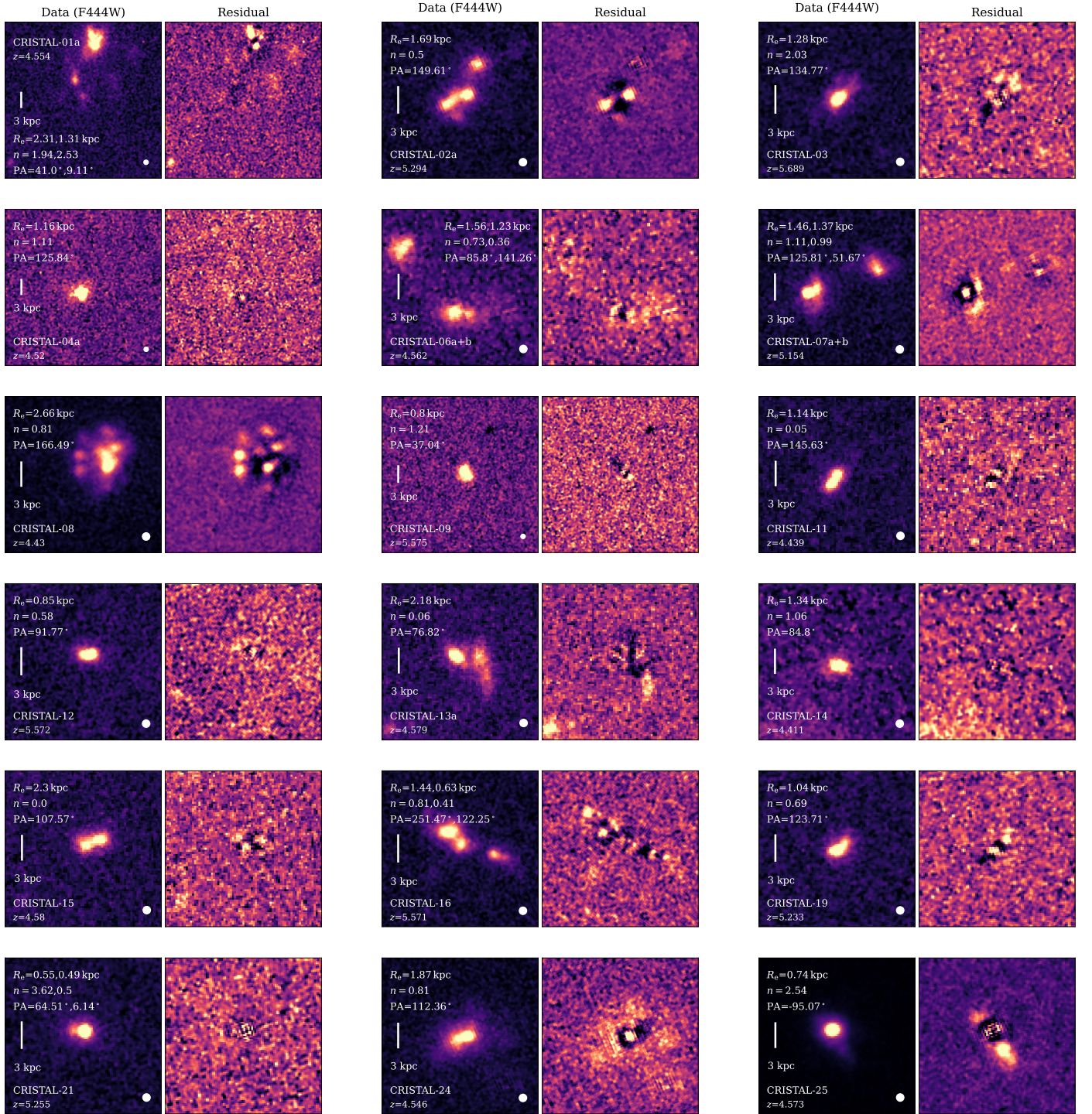


Fig. B.1: Examples of Sérsic fits and residuals of CRISTAL galaxies observed in JWST/F444W (rest-frame  $0.7 \mu\text{m}$  at  $z \sim 5$ ). North is up for all images. For galaxies with multiple components, we simultaneously fit all components, each characterised by a single Sérsic profile. The resulting half-light radii ( $R_e$ ), Sérsic indices ( $n$ ), and position angles (PA, measured counter-clockwise from the north) are listed in Table B.1 and annotated in the figures in order of increasing  $R_e$ . Except in a few cases, such as CRISTAL-09, 12, and 14, the residuals exhibit clumpy structures and asymmetries in the light distributions due to multiple discrete clumps.

We adopt a dust temperature<sup>5</sup>  $T_d = 50\text{K}$ , based on Villanueva et al. (2024) FIR SED modelling of CRISTAL-22, which ben-

<sup>5</sup> This temperature is luminosity-weighted, as the mass-weighted temperature is not available, see Scoville et al. (2016) and Scoville et al. (2017) for the discussion for the resulting difference on the dust mass between the two temperature.

efits from the continuum data observed at multiple bands (but see also Béthermin et al. 2020; Faisst et al. 2020a and Sommovigo et al. 2022). We assume a dust emissivity index<sup>6</sup> of  $\beta = 1.8$ , the suggested value by Scoville et al. (2016) based on the findings of the Planck Collaboration et al. (2011). Such a

<sup>6</sup>  $\beta$  is frequency-dependent but is not constrained by our data.



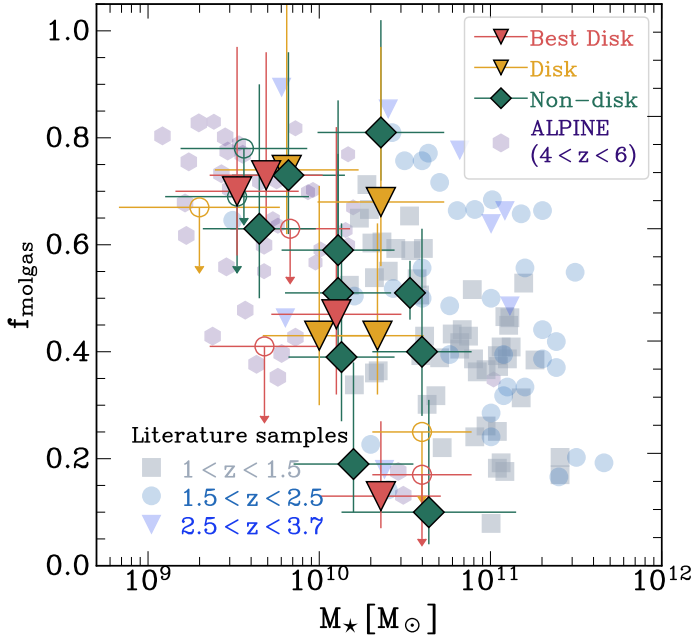


Fig. C.1: Molecular gas fraction  $f_{\text{molgas}}$  (Equation C.3) as a function of stellar mass as inferred from the Band-7 dust continuum based on Equation C.1. The points are colour-coded by their classifications described in Section 3. The empty circles represent upper limits. The median gas fraction of the CRISTAL sample is  $\sim 0.5$ . Our measurements are in broad agreement with those reported by Dessauges-Zavadsky et al. (2020) for the ALPINE samples (purple hexagons), in which we both observe a similar slope of dependence of  $f_{\text{molgas}}$  on  $M_*$ , similar to that of the lower redshifts  $1 \lesssim z \lesssim 6$  star-forming galaxies compiled by Dessauges-Zavadsky et al. (2020) and references therein (light grey to blue markers).

choice is close to the value of  $\beta = 2$  measured by Villanueva et al. (2024). We adopt the R-J luminosity-to-mass ratio  $\alpha_{\text{dust},0} = 6.7 \times 10^{19} \text{ erg (s Hz } M_{\odot})^{-1}$ . Assuming  $\alpha_{\text{dust},0} = 8 \times 10^{19} \text{ erg (s Hz } M_{\odot})^{-1}$  following Tacconi et al. (2020)<sup>7</sup> would result in lower  $M_{\text{gas}}$  by  $\lesssim 0.1$  dex in median.

The gas-to-dust ratio,  $\delta_{\text{gd}} := \frac{M_{\text{gas}}}{M_{\text{dust}}}$ , anti-correlates with metallicity (Eq. (10) in Genzel et al. (2015), see also Leroy et al. (2011) and Tacconi et al. (2018)). We estimate metallicity using the mass-metallicity relation (MZR) inferred from NIRSpec/JWST data of galaxies at  $z = 4$ –10 by Nakajima et al. (2023), which applies to galaxies with masses in the range  $10^{7.5} < M_* < 10^{9.5}$ . We extrapolate the MZR to cover the more massive galaxies in our sample. Our sample’s average metallicity  $\langle 12 + \log(\text{O}/\text{H}) \rangle = 8.27 \pm 0.05$ , and the corresponding gas-to-dust ratio coefficient is  $\langle \delta_{\text{gd}}/150 \rangle = 2.20^{+0.22}_{-0.24}$ . The uncertainties represent the scatter in the Nakajima et al. (2023)’s relation, which would translate to no more than 0.05 dex difference to the final  $M_{\text{gas}}$ .

We note that individual gas-phase metallicities (except for CRISTAL-08, 21, and 23) can be determined from rest-frame optical strong line ratios using NIRSpec/JWST data ( $R = 1000$ ), and the values are consistent with our adopted metallicities. A more detailed discussion of these results will be presented in A. Faisst (in prep.) and S. Fujimoto et al. (in prep.). Parlanti et al.

(2025) presented the metallicity measurement of CRISTAL-20 (HZ4) which is  $12 + \log(\text{O}/\text{H}) \sim 8.3$ .

Based on the  $M_{\text{gas}}$  derived above, Fig. C.1 and Table 3 show the gas fraction of the CRISTAL sample. We define the gas fraction as

$$f_{\text{molgas}} := \frac{M_{\text{gas}}}{M_{\text{gas}} + M_{\text{stars}}}. \quad (\text{C.3})$$

The median gas fraction  $f_{\text{molgas}} = 0.51$ . This is also consistent with the expected value from Tacconi et al. 2020’s relation at  $z = 5$  for  $M_* = 10^{10} M_{\odot}$ , which is  $\sim 0.53$ . For CRISTAL-22, our measured  $f_{\text{molgas}} = 0.71^{+0.28}_{-0.12}$  is consistent with that inferred by Pavesi et al. (2019) from VLA CO(2-1) data. For CRISTAL-01a, 08, 12, 14, 15, 16, 23b, 23c, the measured  $f_{\text{molgas}}$  are upper-limits because the dust continuum fluxes are below the S/N threshold defined in Mitsuhashi et al. (2024). There is insufficient co-spatial dust emission for CRISTAL-04b and 07b, so we have no  $f_{\text{molgas}}$  measurement for those. The stellar mass  $M_*$  are based on SED fitting results presented in Li et al. (2024) for those sources with NIRCam/JWST images; if not, then we adopt the values from Mitsuhashi et al. (2024).

Our  $f_{\text{molgas}}$  measurements, regardless of their kinematics types, are in good agreement with Dessauges-Zavadsky et al. (2020) (purple hexagons in Fig. C.1), which measured  $f_{\text{molgas}}$  for the ALPINE sample based on (i) [C II] emission following Zanella et al. (2018) (ii) rest-frame  $850 \mu\text{m}$  extrapolated from the FIR SED template of Béthermin et al. (2017) and (iii) dynamical mass assuming virialised spherical systems. We also recover a steep relation between  $f_{\text{molgas}}$  and the stellar mass of the systems, similar to the lower-redshift studies following the same selection in Dessauges-Zavadsky et al. (2020) and references therein.

Inferring  $M_{\text{gas}}$  with the method described above is subject to several important caveats. Firstly, the assumption that the Band-7 continuum lies on the R-J tail is sensitive to the adopted single dust temperature,  $T_d = 50 \text{ K}$ . If  $T_d$  is lower, the R-J assumption breaks down, particularly for the highest-redshift sources in our sample. Using  $T_d = 25 \text{ K}$  would increase  $M_{\text{gas}}$  by  $\sim 0.5$  dex. Furthermore, we lack information on the mass-weighted  $T_d$ . The absence of longer wavelength data implies that we are neglecting a dominant colder component of the dust. Additionally, the adopted values for  $\alpha_{\text{dust},0}$  and  $\delta_{\text{gd}}$  are based on lower-redshift measurements and calibrations, although  $M_{\text{gas}}$  appears to be relatively insensitive to these values within the possible range.

An alternative method for estimating  $M_{\text{gas}}$  is by using the [C II] luminosity. If we apply the relation from Zanella et al. (2018) (their Eq. (2)), we find that the resulting  $M_{\text{gas}}$  is systematically higher by 0.23 dex (in terms of the median), but still within the 0.3 dex scatter of the relation. We also observe a significant correlation between the dust- and [C II]-inferred  $M_{\text{gas}}$  values (with Kendall’s  $\tau = 0.56^{+0.12}_{-0.14}$ ,  $p \ll 0.05$ ).

Overall, varying our assumptions and using different methods will very likely lead to higher  $M_{\text{gas}}$  and  $f_{\text{molgas}}$  values, which, as a corollary, a lower Toomre  $Q$  values, as inferred from Eq. (3) in § 6.3. This will not change the main findings that CRISTAL disks are gravitationally (un)stable and the correlations discussed in § 6.2. However, the statistical significance of the correlations would be weaker given the more uncertain  $M_{\text{gas}}$  and  $f_{\text{molgas}}$ .

## Appendix D: Literature sample of $V_{\text{rot}}$ and $\sigma$

Table D.1 lists the literature samples discussed in § 6.1 and shown in Fig. 9.

<sup>7</sup> Tacconi et al. (2020) assumes lower  $\alpha_{\text{CO}}$  and  $X_{\text{CO}}$  than Scoville et al. (2016)’s.

Table D.1: Compilation of literature references for rotational velocity and velocity dispersion from local to  $z \lesssim 8$  galaxies.

Gas phase (Tracer(s))	Reference
	$z \leq 0.5$
Cold/Atomic (H I, CO)	Mogotsi et al. 2016 (THINGS)* Girard et al. 2021 (DYNAMO)**
Ionised (H $\alpha$ , [O II])	Epinat et al. 2008 (GHASP) Girard et al. 2021 (DYNAMO)**
	$0.5 < z < 4$
Cold/Atomic (CO, [C I])	Swinbank et al. 2011 <sup>†</sup> Lelli et al. 2018 Kaasinen et al. 2020 Huang et al. 2023 Nestor Shachar et al. 2023 (RC100) Rizzo et al. 2023 (ALPAKA) Liu et al. 2024b Liu et al. 2025
Warm ([C II]) Ionised (H $\alpha$ , [O III], [O II], C III)	Umehata et al. 2025 Stark et al. 2008 <sup>†</sup> Epinat et al. 2009 (MASSIV) Jones et al. 2010 <sup>†</sup> Gnerucci et al. 2011 (AMAZE-LSD) Livermore et al. 2015 <sup>†</sup> Di Teodoro et al. 2016 Leethochawalit et al. 2016 <sup>†</sup> Mason et al. 2017 (KLASS) <sup>†</sup> Turner et al. 2017 (KDS) Girard et al. 2018 (KLENS) <sup>†</sup> Patrício et al. 2018 <sup>†</sup> Hirtenstein et al. 2019 <sup>†</sup> Price et al. 2020 (MOSDEF) Hogan et al. 2021 Nestor Shachar et al. 2023 (RC100) Puglisi et al. 2023 (KURVS) Barišić et al. 2025 (MSA-3D) Birkin et al. 2024 (KAOSS) Rhoades et al. 2025 <sup>*,†</sup> Wang et al. 2025
	$z \geq 4$
Cold (CO) Warm ([C II])	Tadaki et al. 2018 Rizzo et al. 2020 <sup>†,††</sup> Fujimoto et al. 2021 <sup>†</sup> Jones et al. 2021 Neeleman et al. 2021 Rizzo et al. 2021 <sup>†</sup> Tsukui & Iguchi 2021 Neeleman et al. 2023 Parlanti et al. 2023 Posses et al. 2023 Roman-Oliveira et al. 2023 Rowland et al. 2024 Venkateshwaran et al. 2024 Amvrosiadis et al. 2025 <sup>†</sup> Fei et al. 2025
Ionised (H $\alpha$ , [O III])	Parlanti et al. 2023 de Graaff et al. 2024 (JADES) Danhaive et al. 2025 ('gold' only)

**Notes.** Sources listed in Table D.2 are not duplicated here. (\*) Velocity dispersion only. (\*\*) Local analogues. (†) Lensed. (††) The object is potentially a system undergoing a minor merger with mass ratios of  $\sim 1:6$  separated by  $\sim 4$  kpc (Cathey et al. 2024). Still, the low dispersion of the system  $\sim 32 \text{ km s}^{-1}$  suggests the interaction has not significantly perturbed the dynamics. With an updated stellar mass of  $\log(M_*/M_\odot) \approx 10.39$  and a  $\log[\text{SFR}/(M_\odot \text{ yr}^{-1})] \approx 2.13$ , the galaxy would be shifted closer to the main sequence, with a revised  $\Delta\text{MS} = 0.23$  at  $z = 4.2$ .

Table D.2: Literature sample with multi-phase gas kinematics measurement.

Object	$z$	Tracer	Reference
A521 <sup>*,†</sup>	1.0	CO(4-3) [O II]	Girard et al. 2019 Girard et al. 2019
ALESS073.1	4.8	[C II] H $\alpha$	Lelli et al. 2021 Parlanti et al. 2024
BX610	2.2	CO(4-3) H $\alpha$	Genzel et al. 2023 Nestor Shachar et al. 2023
Cosmic Snake <sup>*,†</sup>	1.0	CO(4-3) [O II]	Girard et al. 2019 Girard et al. 2019
EGS4-24985	1.4	CO(4-3) H $\alpha$	Übler et al. 2018 Übler et al. 2018
GN20	4.1	CO(2-1) H $\alpha$	Hodge et al. 2012 Übler et al. 2024
J0235	6.1	[C II] [O III]	Parlanti et al. 2023 Parlanti et al. 2023
J0901 <sup>†</sup>	2.3	CO(4-3) H $\alpha$	Liu et al. 2023 Liu et al. 2023
J1211	6.0	[C II] [O III]	Parlanti et al. 2023 Parlanti et al. 2023
J2310	6.0	CO(9-8) [C II]	Shao et al. 2022 Shao et al. 2022
MACS0717_Az9 <sup>†</sup>	4.3	CO(4-3) [C II]	Mizener et al. 2024 Pope et al. 2023
PJ0116-24 <sup>†</sup>	1.4	CO(3-2) H $\alpha$	Liu et al. 2024a Liu et al. 2024a

**Notes.** (\*) Velocity dispersion only. (†) Lensed. See also Genzel et al. (2013) and Fujimoto et al. (2024) for qualitative comparisons between kinematics in different gas phases.

## Appendix E: Model velocity profiles

Fig. E.1 shows the intrinsic  $\sigma_0$ , circular velocity profiles of the DM and the baryonic components. The DM fraction profile inferred from the circular velocities  $f_{\text{DM}}(< R) = V_{\text{circ,DM}}^2(R)/V_{\text{circ,tot}}^2(R)$  is shown as the secondary y-axis.

## Appendix F: Comparison to K18 model with total SFR

In § 6.4, we compare the  $\sigma_0$ – $\Sigma_{\text{SFR}}$  with the Krumholz et al. (2018) analytic models. Here, we also compare the CRISTAL values with the models in  $\sigma_0$ –SFR space. Integrating Eq. (4) with radius, the total SFR is related to  $\sigma_g$  by (Eq. (60) in Krumholz et al. (2018)):

$$\text{SFR} = \sqrt{\frac{2}{1+\beta}} \frac{\phi_a f_{\text{SF}}}{\pi G Q} f_{g,Q} v_{\phi,\text{out}}^2 \sigma_g \cdot \max \left[ \sqrt{\frac{2(1+\beta)}{2f_{g,P} \phi_{\text{mp}}}} \frac{8\epsilon_{\text{ff}} f_{g,Q}}{Q}, \frac{t_{\text{orb,out}}}{t_{\text{sf,max}}} \right], \quad (\text{F.1})$$

while for ‘feedback-only’ (fixed  $Q$ ) model (Eq. (62) in Krumholz et al. 2018):

$$\text{SFR} = \frac{4\eta \sqrt{\phi_{\text{mp}} \phi_{\text{nt}}^3 \phi_Q \phi_a} f_{g,Q}^2 v_{\phi,\text{out}}^2 \sigma_g^2}{G Q^2 \langle p_*/m_* \rangle f_{g,P}} \quad (\text{F.2})$$

The definitions of the symbols and values adopted are described in § 6.2 and Table F.1. Here the rotation velocity  $v_\phi$  that is related to the radial gradient of the potential  $\psi$ , is set to be  $v_\phi = \sqrt{r \frac{\partial \psi}{\partial r}} \in [100, 350] \text{ km s}^{-1}$ , in increments of  $50 \text{ km s}^{-1}$ .

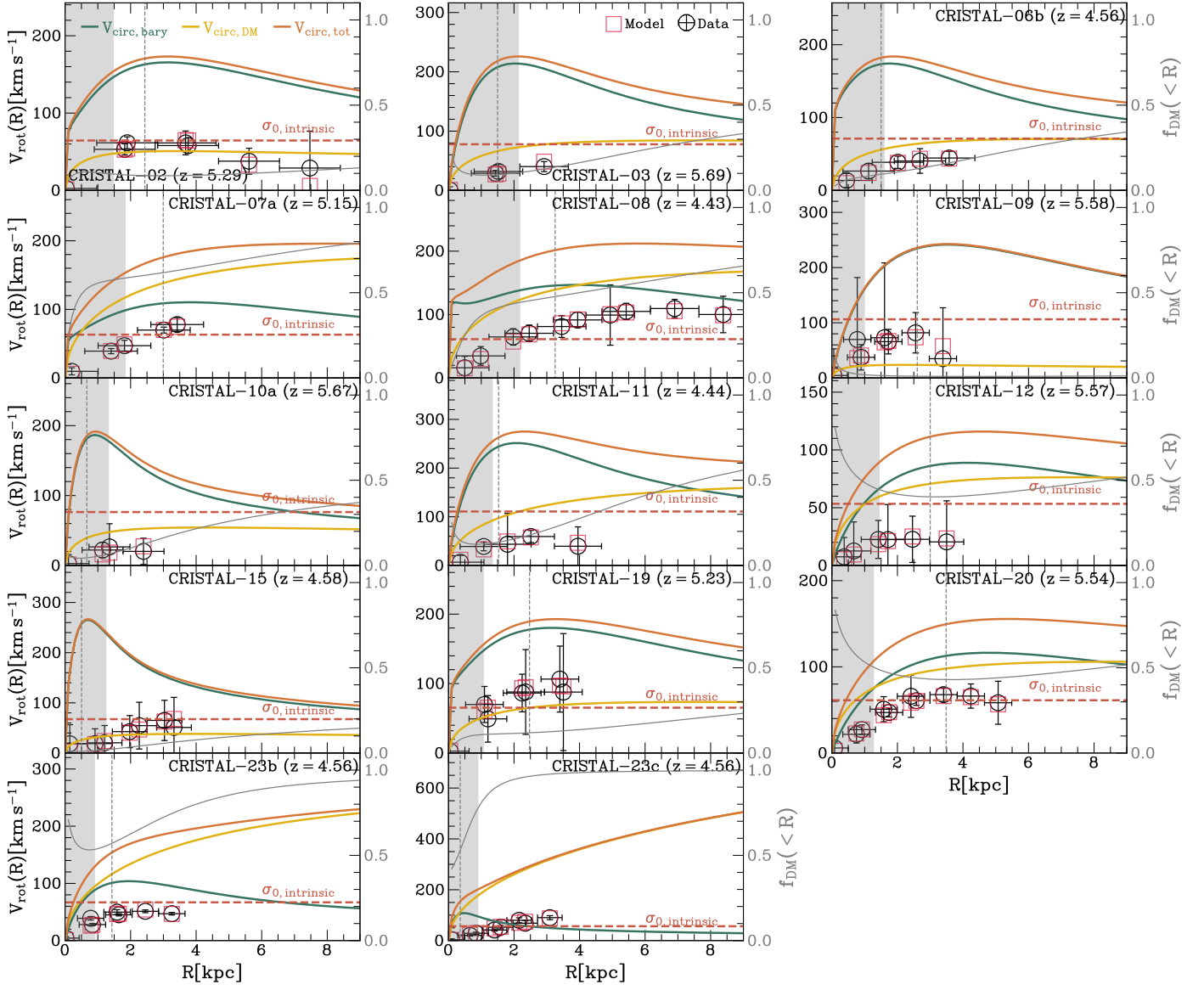


Fig. E.1: Intrinsic baryonic  $V_{\text{circ,bary}}$ , dark matter  $V_{\text{circ,DM}}$ , and total circular velocity  $V_{\text{circ,tot}}$  profiles of the CRISTAL disk samples with asymmetric drift correction. The grey circles mark the folded 1D observed velocity profiles, and the red squares show the observed profiles extracted from the DysmalPy-modelled cubes. The red dashed line indicates the intrinsic constant velocity dispersion  $\sigma_{0,\text{intrinsic}}$ . The dark matter fraction  $f_{\text{DM}}(<R) = V_{\text{circ,DM}}^2(R)/V_{\text{circ,tot}}^2(R)$  is shown in solid grey curves. The grey dashed vertical line marks the disk's effective radius.



Table F.1: Fiducial values adopted for Equations 4, 5 and 6.

Symbol	Value	Unit
$\eta$	1.5	...
$t_{\max}$	2.0	Gyr
$Q_{\min}$	1.0	...
$\epsilon_{\text{ff}}$	0.015	...
$\phi_{\text{mp}}$	1.4	...
$\langle \frac{p_s}{m_s} \rangle$	3000 <sup>†</sup>	km s <sup>-1</sup>
$\phi_Q$	2.0	...

**Notes.** The definitions of each symbol can be found in Table 1 in Krumholz et al. (2018). <sup>(†)</sup> The momentum injection rate used is based on simulations (e.g. Hayward & Hopkins 2017; Krumholz et al. 2018, and references therein) and assumes that supernova remnants undergo an energy-conserving (Sedov-Taylor) phase (Sedov 1946, 1959; Taylor 1950), where energy is converted into momentum. However, this value can vary by up to a factor of 4, which could sustain a higher velocity dispersion of the critical value  $\sim 20$  km s<sup>-1</sup>. To match the properties of CRISTAL disks using star-formation feedback alone, a factor of 10 larger than this adopted value would be required.

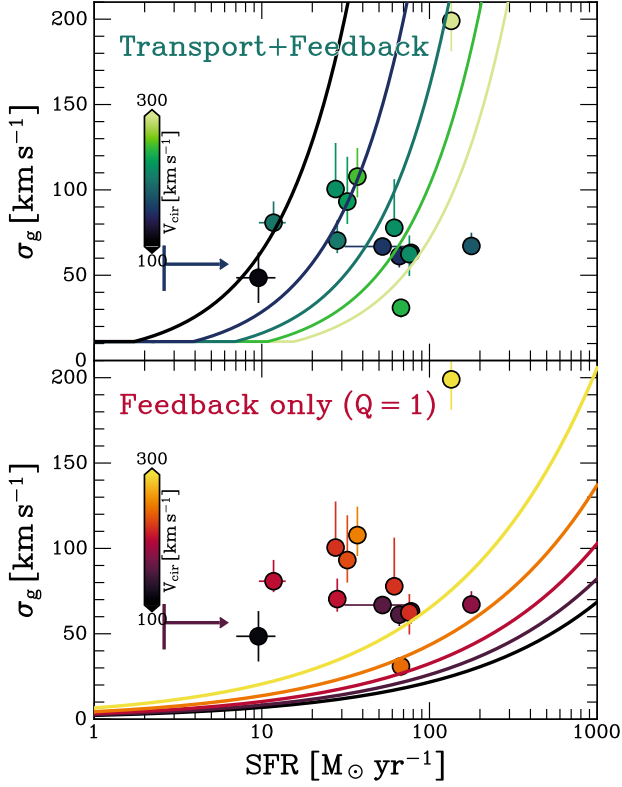


Fig. F.1: Same as Figure 11 but for  $\sigma_0$  vs total star formation rate (SFR). The solid lines are analytical models from Krumholz et al. (2018) based on Equations F.1 and F.2.